Thesis

submitted to

University Pierre et Marie Curie

by

Jean Ochin ABRAHAMIANS KHANGHAH

to obtain the degree of

Doctor of Philosophy of the University Pierre et Marie Curie

Specialization: Robotics

Quartz probes for embedded micro-robotics and imaging

Defended the 10th of May, 2016

JURY

M.	Y. HADDAB	Professor at the Université de Montpellier	Reviewer
M.	H. XIE	Professor at Harbin Institute of Technology	Reviewer
M.	S. RÉGNIER	Thesis supervisor	
		Professor at University Pierre et Marie Curie	Examinator
M.	L. PHAM VAN	Thesis co-supervisor	Examinator
M.	B. GAS	Professor at University Pierre et Marie Curie	Examinator
M.	P. LUTZ	Professor at University of Franche-Comté	Examinator

Thèse

présentée à

L'Université Pierre et Marie Curie

par

Jean Ochin ABRAHAMIANS KHANGHAH

pour obtenir le diplôme de

Doctorat de l'Université Pierre et Marie Curie

Spécialité : Robotique

Sondes de quartz pour la micro-robotique intégrée et l'imagerie

---

Soutenue le 10 Mai 2016

JURY

M.	Y. HADDAB	Professeur à l'Université de Montpellier	Rapporteur
M.	H. XIE	Professeur à l'Institut de Technologie de Harbin	Rapporteur
M.	S. RÉGNIER	Directeur de thèse	
		Professeur à l'Université Pierre et Marie Curie	Examinateur
M.	L. PHAM VAN	Co-directeur de thèse	Examinateur
M.	B. GAS	Professeur à l'Université Pierre et Marie Curie	Examinateur
M.	P. LUTZ	Professeur à l'Université de Franche-Comté	Examinateur

Quartz probes for embedded micro-robotics and imaging

Abstract

As self-sensing and self-exciting tools, quartz probes present many advantages over the heretofore dominant silicon cantilevers for mechanical micro-sensing applications. One of these advantages is that they can be embedded and calibrated without the need for a laser deflection setup. The more compact and self-sufficient tools can therefore be readily integrated and controlled with Scanning Electron Microscopy, which is favoured at the smaller scales of micro-robotic research. More generally, the development and use of quartz probes is bolstered by the fact that they can be fabricated from widely commercialized quartz components and customised through the addition of a microtip. The quartz probes found in the literature are however largely based on components with limited oscillation frequencies, and could benefit from higher operating speeds. In this context, we address the frequency improvement and embedded control of AFM probes with regard to their use in targeted micro-robotics and imaging. The properties of quartz probes are first covered towards the evaluation and use of higher frequency components; we next demonstrate that faster scanning can be achieved with quartz probes made from thickness shear resonators, making them suitable for fast applications which do not require high sensitivity. Lastly, we integrate a tuning fork probe inside a SEM, and establish through it a proof of concept for the non-destructive stiffness mapping of fragile micro-membranes.

Keywords: local probe, micro- and nano-robotics, self-sensing AFM, quartz, high frequency, embedding, mechanical characterisation, scanning electron microscopy

Résumé

Les sondes basées sur des résonateurs en quartz sont des capteurs disposant d'une autonomie en termes d'excitation et d'acquisition, et à cet égard présentent de nombreux avantages par rapport aux poutres cantilever qui ont jusqu'à présent dominé dans les applications de micro-caractérisation directe. Un de ces avantages est qu'elles peuvent êtres embarquées et calibrées sans recours à un système de déflection laser. Ces outils plus compacts et autosuffisants peuvent en conséquence être aisément intégrés et contrôlés au sein d'un microscope électronique à balayage, qui permet une observation globale rapide souvent privilégiée dans la recherche en micro-robotique. Le développement de ces sondes est de plus avantagé de par le fait qu'elles sont constituées de composants électroniques standards répandus dans le commerce, et qu'elles peuvent être adaptées à des usages spécifiques par l'ajout d'une micro-pointe. Les sondes de quartz dans la littérature sont cependant souvent basées sur des composants à fréquence d'oscillation limitée, et une plus grande vitesse d'opération serait utile à l'ensemble de leurs applications. C'est dans ce contexte que nous nous intéressons à des composants à plus haute fréquence, et au contrôle de sondes dans un microscope électronique propre à leur utilisation ciblée en micro-robotique et en imagerie. Les propriétés de ces sondes sont tout d'abord examinées dans le but de pouvoir évaluer et exploiter des résonateurs à plus haute fréquence; nous montrons ensuite que des sondes basées sur des résonateurs à cisaillement d'épaisseur atteignent de plus hautes vitesses en imagerie, ce qui les rend prometteuses pour des applications rapides ne requérant pas une haute résolution. Enfin, nous intégrons une sonde diapason dans un MEB, et établissons ainsi une preuve de concept pour la cartographie en raideur de micro-membranes fragiles.

Mots clefs : sonde locale, micro- et nano-robotique, AFM à capteur autonome, quartz, haute fréquence, intégration, caractérisation, microscopie électronique à balayage

Acknowledgements

The completion of this work has been made possible through the contributions of many, the accurate account of which might have spanned another manuscript. It is fortunate then that the field of physics accommodates approximations, for, thankfully, we have but one page.

My first thanks go to the supervisors of this work. The praise Stéphane Régnier has continuously garnered from all the students he has supported in the past is ever justified, and adding to it would be playing the part of the triangle in a brass orchestra – suffice to say that I would not have set out on this enterprise were it not for his enthusiasm, scientific acumen and human qualities. No less can be said of Jérôme Polesel-Maris, with whom the study of this subject was initiated, and Laurent Pham Van, who kindly carried it on past the first year – I am warmly grateful to both for their mentoring and friendship.

It is through the latter that I may then extend my extolment to St. Albertus Magnus and, down below, to the wonderful team at Saclay – Claire, François, Joël, José and all the others. My fellow Ph.D. students in Paris, too numerous to name, I trust to recognise themselves – alias *the MicRob Team*, with a special mention for the two I have worked with the closest: Bruno Sauvet and Shuai Liang; I would be remiss not to place next to them Sylvain Pledel, Sinan and Ky Lân, and the staff of the ISIR lab – Michèle, Anne-Claire, Adela, Ludovic and Yves.

Beyond the two laboratories this work was conducted in, I must also express my gratitude to the Drs. Patrick Hsia and Farid Kameche, and soon-to-be-Drs. Nathalie Bonatout and Annie Lamalice, as much for their congeniality as for fruitful discussions. I may at last salute my comrades Allister & Fynn, who gaily brightened even the dreariest of days, though our paths did part – and will close by thanking my parents, as always, for their extraordinary food and support. May those I have forgotten forgive me.

J.O.A.
Paris, 17 May 2016

Contents

Contents **i**

List of figures **v**

General introduction **1**

1 Probing into the micro-world: imaging, tools and state of the art **3**

1 Micro-robotics, observation and actuation 3
1.1 Physics of the micro-world 4
1.1.1 Scale effect 4
1.1.2 Surface forces 5
1.2 Observing the micro- and nano-world 5
1.2.1 Optical microscopes 6
1.2.2 Electron microscopes 6
1.2.3 Local probe microscopes 7
1.3 Micro-robotic systems and SEM-controlled characterisation 8
1.3.1 Micro-robotic actuators 8
1.3.2 SEM-integrated platforms 9
2 Sensing and imaging through Atomic Force Microscopy 12
2.1 General principles of AFM 12
2.1.1 AFM modes 12
2.1.2 Dynamic AFM control modes 14
2.2 Tuning fork AFM 17
2.2.1 Operating principle 18
2.2.2 Force measurement 19
2.2.3 Conservative and dissipative forces 20
2.2.4 Stiffness measurement 20
2.3 AFM environments 22

2.4 High-frequency AFM . . . 23
3 Objectives . . . 24

2 Micro-robotic probes designed from standard quartz resonators 27
1 Mechanical properties of tuning forks . . . 28
1.1 Quality factor . . . 28
1.2 Stiffness . . . 29
1.3 Sensitivity . . . 30
2 Probe fabrication . . . 31
2.1 Probe tip . . . 32
2.2 Adhesive and balancing . . . 34
2.3 Tip positioning . . . 35
2.4 Probe holder and fixation . . . 36
3 Towards higher frequencies . . . 37
3.1 Tuning fork overtones . . . 37
3.2 Other tuning fork frequencies . . . 39
3.3 Thickness shear quartz resonators . . . 40
3.3.1 Horizontally mounted resonators . . . 40
3.3.2 Disc resonators . . . 42
3.3.3 Contoured beam resonators . . . 44
3.4 Comparison . . . 44
4 MHz-range contoured beam quartz analysis . . . 45
4.1 Hypotheses . . . 45
4.2 Results . . . 47
5 Conclusion . . . 50

3 Ambient imaging with quartz probes 51
1 Experimental setup . . . 52
1.1 Quartz control, electronics and software . . . 52
1.2 Actuators . . . 54
1.3 Control parameters . . . 55
2 Experimental protocol and testing . . . 57
2.1 Attractive and repulsive modes . . . 57
2.2 Samples . . . 58
2.3 Imaging criteria . . . 58
2.4 Artefacts and causes . . . 60
2.5 Preliminary internal characterisation . . . 61
2.5.1 Actuator overshoot . . . 61
2.5.2 Overall Z-axis drift . . . 62
2.5.3 Adhesion and meniscus effect . . . 63
2.6 Adopted conventions . . . 64
3 Attractive mode FM-AFM . . . 64
3.1 32.768 kHz probe on calibration grating . . . 64
3.2 32.768 kHz and 196 kHz overtone probes on paraffin wax . . . 66
3.3 3.58 MHz probe on silicon surface . . . 67
3.4 Overview of the attractive mode . . . 67

4 Repulsive mode FM-AFM 67
4.1 32.768 kHz probe on paraffin wax 67
4.2 100 kHz probe on paraffin wax 69
4.3 100 kHz probe on calibration grating 70
4.4 10 MHz probe on calibration grating 71
4.5 3.58 MHz probe on calibration grating 71
4.6 3.58 MHz probe on paraffin wax 74
5 Conclusion and perspectives 80

4 SEM-embedded micro-robotic sensing with quartz tuning forks 81
1 Quartz probe sensing and in air, vacuum and SEM environments 82
1.1 Setup and pressure 82
1.2 Effect on the piezo-actuating system 83
1.3 Quartz frequency, quality factor and dissipation 83
1.4 Influences on settling time 85
1.5 Influences on sensitivity 86
1.6 Influence of the electron beam in a Scanning Electron Microscope 90
1.7 Conclusion and perspectives 94
2 Membrane stiffness measurement in a SEM 94
2.1 Samples and setup 94
2.2 Membrane stiffness measurements 98
2.3 Results 100
3 Conclusion 104

Conclusion and Perspectives 105

Bibliography 107

List of publications 117

List of Figures

1.1 Balance of forces with regard to scale . . . 4
1.2 Microscope resolution scale. . . . 6
1.3 Optical and electron microscope images . . . 7
1.4 Stick-slip actuating scheme . . . 9
1.5 Micro-robotic platforms and positioners designed for SEM integration . . . 10
1.6 Reduced depth of field in optical microscopy and impact on tilted stage . . . 11
1.7 AFM laser beam setup . . . 14
1.8 Repulsive and attractive zones on a pull-in curve . . . 15
1.9 AM-AFM block diagram . . . 15
1.10 FM-AFM block diagram . . . 16
1.11 PM-AFM block diagram . . . 17
1.12 Tuning fork . . . 18
1.13 Tuning fork electrodes . . . 18
1.14 Tuning fork antiphase oscillation mode . . . 19
1.15 Spring-mass mechanical models of tuning forks . . . 22

2.1 Q factor and -3 dB bandwidth of a resonance curve. . . . 28
2.2 Tuning fork tine effective length . . . 29
2.3 Tuning forks in various states . . . 32
2.4 Platinium-Iridium tip etching . . . 33
2.5 Direct tip etching . . . 33
2.6 Influence of tip curvature . . . 34
2.7 Tip positioning on a tuning fork . . . 36
2.8 Tuning fork overtone resonance diagram . . . 38
2.9 Tuning fork tines length comparison. . . . 39
2.10 Thickness shear quartz deformation. . . . 40
2.11 Horizontal thickness shear quartz resonator (QZ2768 7.68 MHz). . . . 41
2.12 Horizontal TSR: Finite Element analysis . . . 41

2.13 Horizontal TSR: Resonance mode and deformation. 42
2.14 Disc-shaped thickness shear quartz resonator (Rakon XTAL 3.255 MHz). 42
2.15 Disc-shaped TSR: Finite Element analysis 43
2.16 Disc-shaped TSR: Electrodes and oscillation 43
2.17 Contoured beam thickness shear quartz resonator (CSA31, 3.579 MHz) 44
2.18 Contoured beam TSR: In-plane flexural mode Finite Element analysis 46
2.19 Contoured beam TSR: Out-of-plane flectional mode Finite Element analysis . . . 46
2.20 Contoured beam TSR: Finite Elements meshing 47
2.23 Contoured beam TSR: 3D displacement graph 47
2.21 Contoured beam TSR: Finite Elements electric displacement field 48
2.24 3.58 MHz probe with tip 48
2.22 Contoured beam TSR: Finite Elements displacement graph X, Y 49

3.1 Experimental setup. 52
3.2 Overall structure of the experimental setup. 53
3.3 Actuators setup and probe holder. 54
3.4 X/Y/Z nano-positioning actuator Nano-PQD375HS (Mad City Labs Inc.). 55
3.5 Calibration sample: NT-MDT TGZ series. 58
3.6 Difference between the backward (blue) and forward (white) scanned profiles being discordant (top) or concordant (bottom). 59
3.7 Effects of tilt compensation 61
3.8 Height colour scale 64
3.9 Ambient approach curve 65
3.10 Calibration grating image, attractive mode: 32.768 kHz probe at 1.6 µm/s 65
3.11 Calibration grating image, attractive mode: 32.768 kHz probe at 1.1 µm/s, rotated 66
3.12 Paraffin wax image, repulsive mode: 32.768 kHz probe speeds comparison and profile curve 68
3.13 Paraffin wax image, repulsive mode: 100 kHz probe speeds comparison 69
3.14 Paraffin wax image, repulsive mode: 100 kHz probe speeds comparison 2 70
3.15 Calibration grating image, repulsive mode: 100 kHz probe under 1 µm/s 71
3.16 Calibration grating image, repulsive mode: 10 MHz probe at 1 µm/s. 72
3.17 Calibration grating image, repulsive mode profile. 72
3.18 Calibration grating image, repulsive mode: 3.58 MHz probe at 22-28 µm/s 73
3.19 Calibration grating image, repulsive mode: 3.58 MHz probe image defects above 40 µm/s 74
3.20 Calibration grating images, repulsive mode: 3.58 MHz probe scan speeds comparison 75
3.21 Paraffin wax image, repulsive mode: 3.58 MHz probe at various speeds 76
3.22 Paraffin wax images, repulsive mode: 3.58 MHz probe scan speeds comparison . . 77
3.23 Paraffin wax images, repulsive mode: 3.58 MHz probe scan speeds, single line comparison 78
3.24 Paraffin wax images, repulsive mode: 3.58 MHz probe scan speeds cross section profile comparison 79

4.1 Stick-slip piezo actuator 83
4.2 High dissipation due to a micro-object on the probe tip 84
4.3 Q factor and amplitude response to shifted frequency 85

4.4 Settling time with a same Q factor, with variable environment and mass 86
4.5 Phase signal noise 87
4.6 Phase-locked frequency shift signal noise 88
4.7 Transverse mode, approach curves 89
4.8 Transverse mode, repulsive approach curves 90
4.9 Shear mode, long-range approach curves 91
4.10 Long-range electrostatic effects 92
4.11 Effect of exposure to a SEM beam 93
4.12 Manipulation setup inside the SEM vacuum chamber and SmarAct robotic platform. 95
4.13 Suspended micro-membrane samples 96
4.14 Destroyed micro-membranes 97
4.15 Blender virtual reality interface and control scheme 97
4.16 Tuning fork probe viewed by SEM; illustration of the probe and samples. 98
4.17 Frequency shift pull-in and pull-off 99
4.18 InP membranes, stretched or compressed 99
4.19 Automated measurement process step-by-step 101
4.20 Local stiffness variations on two stretched flat membranes 102
4.21 Local stiffness variations on a convex membrane 102
4.22 Stiffness measurements between two suspensions of a concave membrane 103

General introduction

The ability to probe and sense at the micro-scale is a defining aspect of micro-robotic research. The diverse applications developed in the field all derive their capabilities from the combined performances of control, actuating and sensing tools, and this work focuses on a category of tools which is especially adaptable to the multi-part systems built in micro-robotics: the self-sensing local probes of atomic force microscopy (AFM).

AFM is a local probe force-sensing technique which is now a popular way of obtaining topographical and fine-resolution imaging data, with many commercially available solutions. However, while AFM has allowed the direct observation of the atom itself, its most advanced systems are still custom-built for research in the fields of fundamental physics, biology and chemistry. In general and in micro-robotics especially, there is yet a need for AFM solutions to be made faster, more sensitive, easier to operate, capable of functioning in less amenable environments, and of providing quantitative force-sensing data – challenges which are the subject of increasingly pointed research. In this context, we will address the improvement and embedded control of AFM probes with regard to their use in imaging and in micro-robotics.

Our work focuses on the more recent branch of AFM based on quartz tuning forks (QTF), standard electronics components which can be fitted with a microtip to function as self-sensing probes. We will see that self-sensing AFM provides an advantage over the laser-deflection cantilevers which have been the most commonly used and adaptable tools in the various tasks of micro-robotics, making QTF probes highly suitable for embedded systems. In addition to their improvement in imaging, our objective will hence be to show how these force-sensing probes can be used and adapted to the structures of micro-robotic experimentation.

The corresponding state of the art in micro-robotics and AFM will be reviewed in Chapter 1. A brief summary of the physics and observation techniques associated with micro-robotics and the importance of electron microscopy will first demonstrate this need for compact and embeddable systems which points to self-sensing AFM. The general principles of AFM and how they apply to imaging and force sensing in various environments will then be covered. The operation and control equipment of QTF probes will follow, together with the mechanical models and hypotheses necessary to force and stiffness sensing, leading to an examination of the current literature working towards their improved performance in imaging and in the targeted characterisation of mechanical properties.

Chapter 2 will be dedicated to the design and fabrication process of quartz probes. Like with QTF resonators, we will remain within the confines of standard, commercially available electronic components, which make the fabrication of quartz probe possible without industrial equipment. The fabrication and properties of standard QTF probes, on which depends not only the calibration but also the comparability and reproducibility of all imaging and force-sensing data, will be examined first: in addition to providing the necessary understanding for the experiments conducted in the later chapters, this will form the basis on which to select higher frequency quartz resonators for the development of faster probes.

Chapter 3 will proceed with testing the performance of quartz probes based on the selected high-frequency components, and comparing them to QTF probes in ambient imaging, to judge the extent to which these higher-frequency probes can improve the performance and extend the potential of AFM systems in imaging and micro-robotic applications. With an aim to validate the design of these probes in experimental systems which are impacted by a multitude of factors, this study will evaluate scanning speed results by relying on the qualitative comparison between images taken on a same set-up with both unknown surfaces and calibration samples.

Chapter 4 will lastly address the embedded control of quartz probes. In a case study where cantilever laser deflection methods are incompatible with the control requirements of micro-robotics, the opportunities enabled by self-sensing will be fully exploited through the combined use of QTF probes with a scanning electron microscope (SEM), while encompassing the conditions and difficulties related to the corresponding operating environment: low pressure and electrostatic charging. Using an actuation platform designed for the SEM vacuum chamber and tailored virtual reality and automation control tools, a proof-of-concept for SEM-embedded stiffness characterisation applications with quartz probes will be conducted, with measurements taken *in situ* on fragile micro-membranes amidst a manufactured batch, locally and non-destructively.

Chapter 1

Probing into the micro-world: imaging, tools and state of the art

Probing the micro-world for imaging and characterisation is the combined task of several control and actuation systems, at the end of which are the quartz probes studied here. As this work intersects with both micro-robotics and atomic force microscopy (AFM), this chapter will sum up the fundamental principles and outline the corresponding state of the art in both fields. It will first cover the observation and actuation tools involved through the broader aspects of robotic operation at the micro- and nano-scales; a second section will then be dedicated to AFM sensing, from its general principles and operating environments to the case of self-sensing quartz probes, and their improvement through increased operating frequencies. We will thus aim to point out the needs and experimental conditions involved in micro-robotic research, how self-sensing AFM can answer them, and the perspectives for this technology in both fields.

1 Micro-robotics, observation and actuation

The driving forces behind micro-scale experimentation hang on appropriate observation, actuation and control tools which are the centrepiece of micro-robotics. Micro-robotics as a field has been developed since the 1990s, and consists in the application of micro- or macro-scale robotic tools in order to affect micro-scale objects – where micro-scale originally refers to sizes between a micrometre and a millimetre. This extends further into actuation and manipulation down to the nanometre scale, and although the transition is not trivial, the physics here will pertain to both the micro- and nano-world. This section will address the main aspects of physics and robotics which are specific to these scales: physical phenomena, observation tools, actuation

systems, and, as pertains to the experiments conducted in this work, their applications under scanning electron microscopes.

1.1 Physics of the micro-world

The physical phenomena which form the basis of interaction and sensing at the micro-scale are not those we are normally familiar with. Although the laws of classical (as opposed to quantum) physics still apply at this scale, different forces prevail in the micro-world. This difference is referred to as the scale effect [Chaillet 10].

1.1.1 Scale effect

The prevailing forces at our scale (the human or macro-scale) are "volumetric forces", so called because they scale with the volume of the objects involved: gravity and inertial forces. However, at the micro-scale, the power balance is reversed and "surface forces" take over.

This phenomenon can be illustrated through the "Square-Cube Law": a cube with edges 10 cm has 100 cm^2 sides and a volume of 1000 cm^3. A cube with ten times smaller edges would have a side surface of 1 cm^2 (e.g. a hundred times smaller) and a volume of 1 cm^3 (e.g. a thousand times smaller). Therefore, through this evolution in scale, the effects of forces that apply on surfaces progressively catch up with those of volumetric forces (Fig. 1.1).

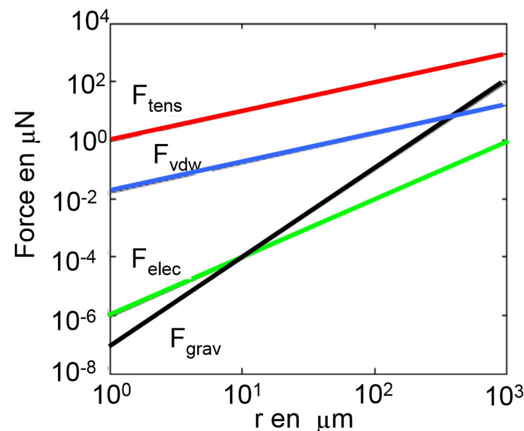

Figure 1.1 - *Evolution of the balance of forces when going down in scale [Menciassi 04] : tension forces (F_{tens}), van der Waals forces (F_{vdw}), and electrostatic forces (F_{elec}) progressively get to overcome gravity (F_{grav}).*

Beyond surface and volume forces, the scale effect also affects behaviour as they relate to time (time dilatation) and all physical phenomena of the micro-world, from solid or fluid mechanics to heat transfers. The immediate consequence is the apparition of significant interaction forces

between objects: attractive forces if they are very close, adhesion forces if they are in contact, but also attractive or repulsive electrostatic forces which can be completely unpredictable. These behaviours result in both challenges and opportunities for experimentation at the micro-scale.

1.1.2 Surface forces

Surface forces can be attractive or repulsive. Attractive forces notably contribute to adhesion effects, which are omnipresent in micro-robotics. The three main categories of adhesion forces at the micro-scale are : [Israelachvili 91]

- Van der Waals forces: interaction forces between two permanent or induced dipoles, which cover most intermolecular forces aside from covalent or hydrogen bonds. They are dependent upon the materials of the objects, and become significant at distances around a dozen nanometres.
- electrostatic forces, or classical Coulomb forces, which act between all charged objects. They are dependent upon the accumulation of electrostatic charges by the objects. When in the presence of even weak charges, electrostatic interaction of modest magnitude can be detected from over a hundred nanometres, but compared to Van der Waals forces, it only becomes significant in closest proximity [Butt 91].
- capillary forces, which govern surface tensions and liquid menisci, according to the humidity of the medium. They appear at air-liquid interfaces, or on immersed hydrophobic surfaces. They are dependent upon the nature of the liquids, materials and geometry of the system.

In the context of this work, quartz probes will mainly seek to sense attractive or repulsive van der Waals forces, which are reliably short-ranged. Electrostatic forces apply at a greater and potentially more variable range, and may for this reason be an obstacle, especially in the experiments combined with electron microscopy in Chapter 4.

1.2 Observing the micro- and nano-world

Various means of observation are available when it comes to obtaining global vision feedback into the micro-world. Depending on the scale aimed for (Fig. 1.2), they rely on distinct physical principles of operation, and may interact directly or indirectly with objects to build an image. Alternatives to optical vision therefore come with their advantages as well as additional hindrances; in this regard, the microscopes relevant to this work are the optical, electron and local probe microscopes, the characteristics of which are as follows.

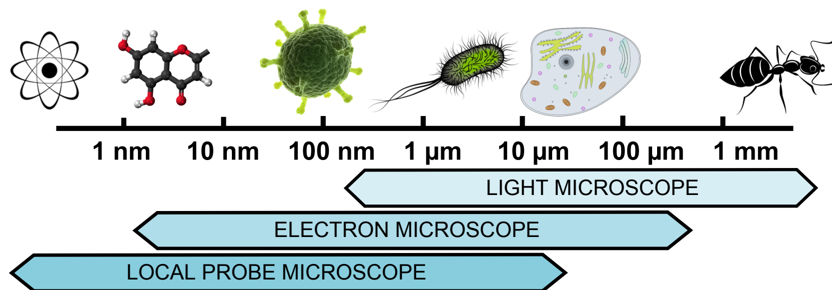

Figure 1.2 - *Microscope resolution scale.*

1.2.1 Optical microscopes

Optical microscopy relies on mirrors and lenses to redirect photons and provide the user with an enlarged image. Photons can be reflected, as is the case for human vision, or transmitted (going through a transparent sample). Although it is very commonly used and easy to set up, optical microscopy is limited by:

- resolution, which cannot be lower than 0.2 µm for classical optical microscopes [1]
- depth of field, which decreases as resolution increases, and only covers a very thin layer of space, so that topography or movements along the depth axis cannot be observed.
- field of view, which decreases in the same manner.

1.2.2 Electron microscopes

Electron microscopy relies on electrons instead of photons. Electrons are emitted by a field electron gun (electromagnetically induced) or a thermoionic field gun (tungsten filament, LaB6 cathode). As with photonic microscopy, these electrons can then be reflected (SEM: Scanning Electron Microscopy) or transmitted (TEM: Transmission Electron Microscopy). The electron beam interacts with matter as it hits its surface, which results in emissions e.g. secondary, Auger, back-scattered electrons, or X-rays. These emissions are intercepted by specific sensors, and treated so as to reconstruct an image of the object's surface, topography, atomic composition...

A SEM can reach sub-nanometre resolutions, and a TEM ten times finer resolutions yet on thin samples. However, the electron beam also interacts with the environment along the distance that separates it from the samples, including air molecules - an electron microscope therefore requires a vacuum chamber (or at least, in the case of the more recent "environmental" models[2],

[1]The Rayleigh criterion or Rayleigh limit: half the illumination wavelength.

[2]These models, based on technology enabling airtight transmission between the gun and sample chambers, are meant to extend their application range to the observation of e.g. hydrated objects around the triple point of water, or objects that would be damaged by low pressure.

an environment with controlled pressure and composition). Further, the samples and sample holders must be conductive, lest electric charges accumulate on them and interfere with the behaviour of the microscope. Despite these drawbacks, electron microscopy is the most popular when real-time vision feedback is required at resolutions not reached by optical microscopy.

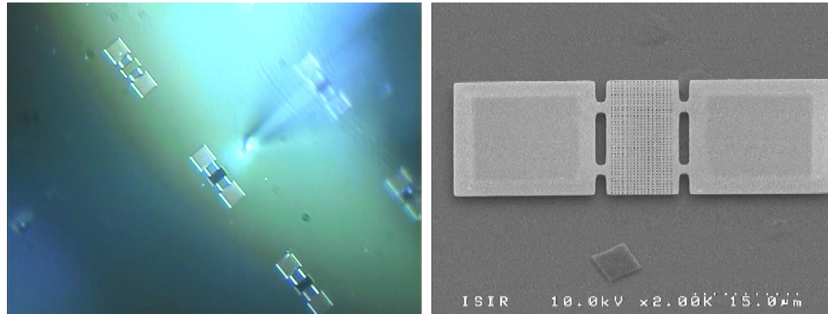

Figure 1.3 - *Images of a 20×30 μm membrane by optical (left) and electron (right) microscopy.*

1.2.3 Local probe microscopes

These microscopes use end-tools of various natures, sizes and operating principles, which have in common that they probe the observed surfaces with a stiff tip. In each case, the apex of this tip is of a nano- or micrometre scale and is brought very close or even in contact with the zones of interest. Imaging conducted with quartz probes falls into this category.

- Atomic Force Microscopes (AFM) [Binnig 86] : probes are either soft cantilevers deflecting and reflecting a laser, or more recently so-called "self-sensing" probes, such as the quartz resonators used in this work. Measured data are the Z (vertical) position of the probe and the interaction forces applied on the apex of its tip, be they attractive or repulsive. This combined information allows the reconstitution of a topographic profile of the sample's surface, and/or the measurement of forces at the nano- or pico-Newton scales. The three main AFM modes are contact mode, intermittent contact (or "tapping"), and "non-contact" (or "near-contact") modes. These modes of operation, as well as the state of the art in AFM, will be further elaborated on in the next section of this chapter. Aside from (or in conjunction with) microscopy, AFM probes can also be used as self-sensing manipulators [Xie 12b].
- Scanning Tunnelling Microscopes (STM) [Binnig 82] can be used for conductive or semi-conductive samples. As the tip remains within 0.1 to 1 nanometre of the object's surface, information is obtained through the electric current flowing between the two. Tunnelling can also be combined with atomic force microscopy on a same probe [Polesel-Maris 11b], with the drawback that any deformation caused by one mode of observation is then itself observed by the other with a phase shift [Morán Meza 13]. Just as AFM can be used to push objects along with their imaging capabilities, so have STM been used for electrodeposition - for instance to build nanometre-scale batteries [Li 92].

- many variations exist on the AFM concept that, instead of transversal van der Waals forces, exploit magnetic force (Magnetic Force Microscopy), chemical interactions (Chemical Force Microscopy - [Frisbie 94]), friction (Lateral or Friction Force Microscopy [Mate 87] [Marsden 13]), electrostatic potential (Electrostatic Force Microscopy [Terris 89], Kelvin Probe Microscopy [Nonnenmacher 91])... each adapted to specific phenomena or sample properties of interest.

The capabilities of local probe microscopes vary widely across all types – the technology is however the most precise currently in use, and can reach the atomic resolution [Giessibl 05]. The main performance downside of local probe microscopy is the length of time it takes to scan an image: several minutes for micrometre-sized samples, and up to half an hour or more when aiming for higher-resolution images. This is one of the motivations behind seeking higher-frequency quartz resonators in the next two chapters, and the literature on the subject will be examined in Sect. 2.4. Although quartz local probes will be used as imaging tools in Chapter 3, the sample characterisation experiments that follow in Chapter 4 will require real-time vision: electron microscopy (SEM) will therefore be the observation method of choice. Whether it be for imaging or its applications in force sensing or characterisation, local probe microscopy will equally rely on micro-actuation systems; we now turn towards these sytems and their combined use with SEM.

1.3 Micro-robotic systems and SEM-controlled characterisation

Micro-robotic setups involve accurate movements at the micro-scale, carried through actuating systems at the end of which effectors are displaced by micrometric or nanometric steps. These systems can be composed of one or more actuators, and assembled into micro-robotic platforms with one or several effectors adapted to the environment, sample objects and observation method.

1.3.1 Micro-robotic actuators

Micro-robotic actuators exploit displacement phenomena which are not significant at the macro-scale but offer great accuracy in micro-manipulation. The main actuating principles used in micro-robotics are piezoelectric; electrostatic; thermal; SMA (shape memory alloys) or EAP (electroactive polymers) [Chaillet 10].

To this day, actuators used in micro-robotics have for the most part been based on the piezoelectric effect: deformation occurs when current is applied through piezoelectric ceramics in a quantified and repeatable manner, which is easily controlled in closed loop. This deformation, when exploited directly, offers the ability to apply continuous displacement at extremely high resolutions proportional to the actuator's size. Hence, the best resolutions and speeds [Yong 12] cannot be directly applied on a large range. A common way to remedy this problem is to have a small-range, accurate positioner placed at the end of a rougher, larger-range positioner chain. Another way to exploit the piezoelectric effect for larger-range positioning exists through the

stick-slip principle [Breguet 98] : during the "stick" phase, a progressive displacement is applied by a piezoelectric actuator, during which the effector is carried by its guide through friction; then the electric signal driving this displacement is suddenly inverted, and the subsequent, comparatively much quicker deformation or relaxation of the piezoelectric actuator withdraws the guide but lets the end effector "slip" (Fig. 1.4). Whereas the actuators used in Chapter 3 are piezo-stacks with a range limited to 50 micrometres, Chapter 4 will make use of stick-slip actuators with a range over a centimetre, which represents an advantage over a combination of distinct coarse- and fine actuators in that the position sensors remain the same throughout both large-range and close-range motion – meaning that the reference position between effector and sample is not lost after large-range relocation, in turn enabling enough flexibility for operations such as the local characterisation of samples on a larger-scale batch to go on uninterrupted.

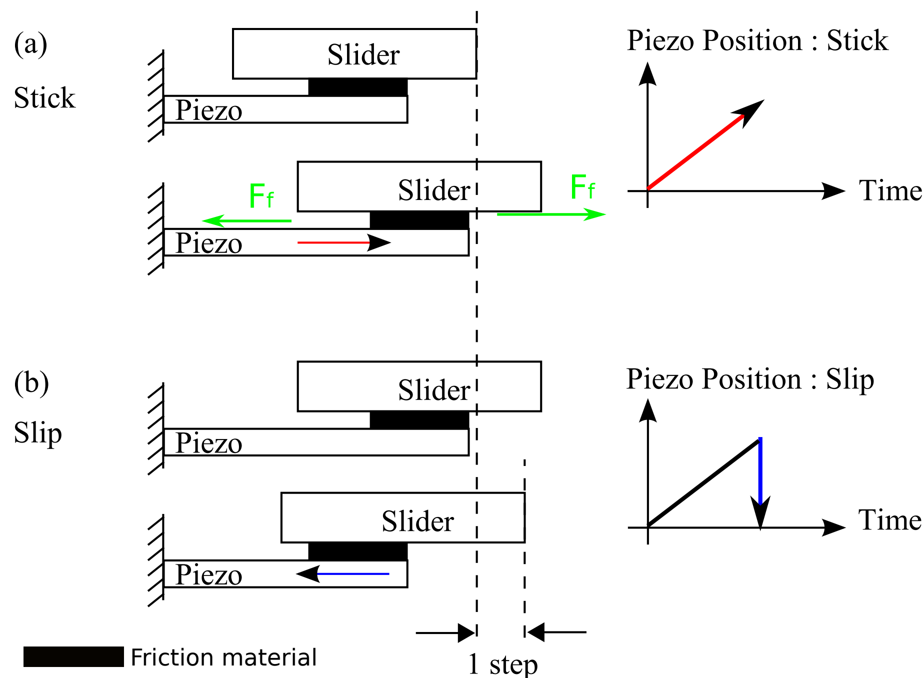

Figure 1.4 - *Stick-slip actuating scheme: stick (a) and slip (b) phases.*

Other types of positioners are found in the literature, especially in order to satisfy specific requirements with regard to performance or environmental conditions. General-purpose micro-robotic manipulation platforms (such as the SmarPod system used in this work), however, all rely on the piezoelectric effect.

1.3.2 SEM-integrated platforms

In order to use a manipulation system at the nanometric scale, the positions of the tools and effectors relative to the objects with which they interact need to be observed in a fairly precise manner. In the case of Atomic Force Microscopy (AFM), the manipulator itself can be used as

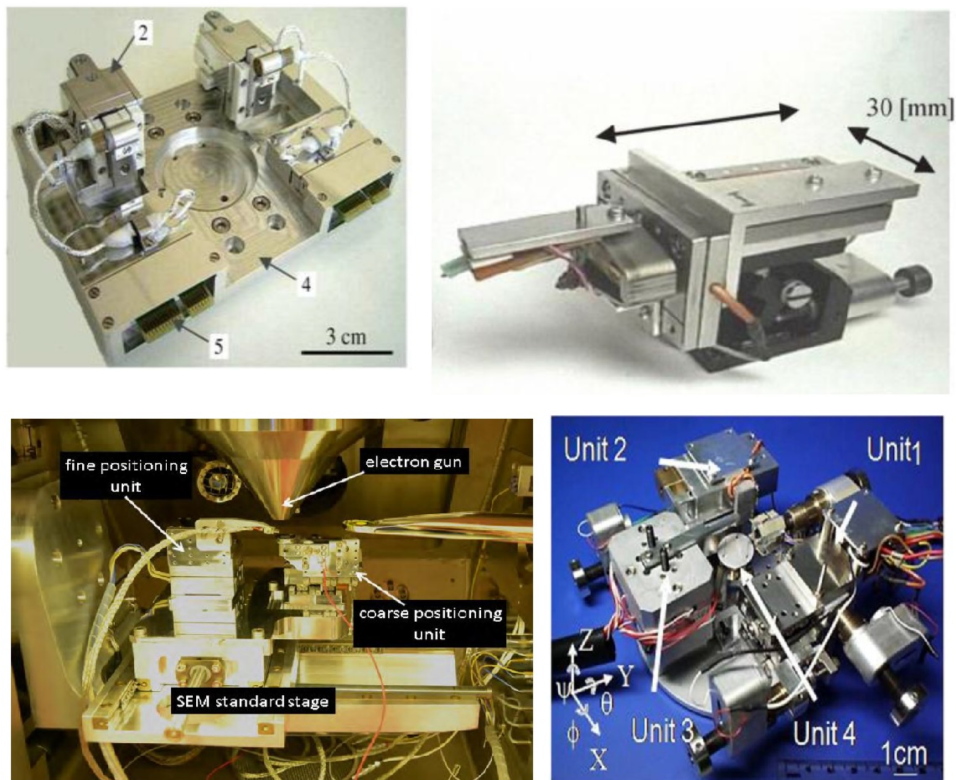

Figure 1.5 - *Micro-robotic platforms and positioners designed for SEM integration; from left to right and top to bottom from the Universities of Toronto [Zhang 13], Shizuoka [Takahashi 11], Oldenburg [Eichhorn 12] and Nagoya [Yang 12].*

a probe to obtain images before or during the manipulation, but more complex or exploratory operations call for more direct visual feedback. Using scanning electron microscopes (SEMs) is advantageous in this regard. This choice is mainly motivated by performances that classical optical microscopy cannot offer: the nanometric imaging resolution, and the depth of field which is instrumental to simultaneously observing tools and samples. Indeed, in a typical setup, tools and samples end up being superimposed vertically during operations, and the field of view needs to be tilted at an angle in order to discern the precise interactions and contact points between the two (Fig. 1.6). In these conditions, it is often impossible to focus on both using optical microscopy. Without a depth of field such as that offered by a SEM, it is possible for AFM and derived technologies to rely on force-feedback to control the position of the tools relative to substrates and samples; one can also tilt the effectors rather than the whole system, or use angled tool tips [Higuchi 11] as is often the case for cantilevers. However, in some cases tools must stay perpendicular to the surface of the sample (see Chapter 2, Sect. 2) and, short of designing specific interface tools, a tilted field of view with a high depth of field may indeed be required for human-operated experimentation.

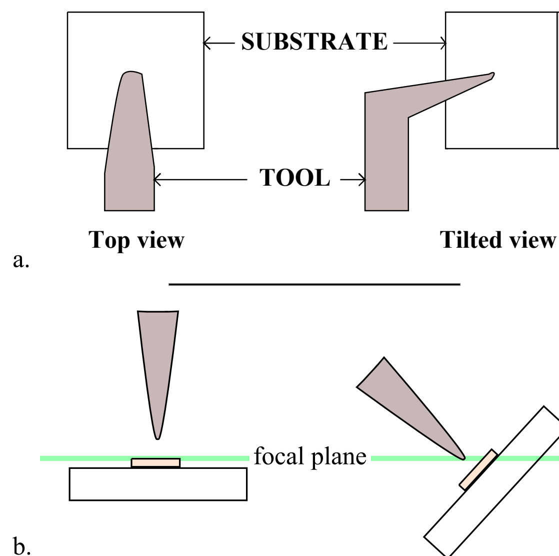

Figure 1.6 - *Illustration of the reduced depth of field in optical microscopy and its impact when the observed surface is tilted – a.: Cantilever tool viewed from above; b.: Focal plane in a tilted setup; the depth of field cannot fully include both the probe and sample.*

Dissuasive factors, on the other hand, are the cost and upkeep of a SEM. Besides, the technical challenges related to the use of a SEM are themselves the subject of much work, usually concerning the vacuum chamber which is part of a SEM. When it comes to effectors and tools, these challenges include the potentially limited space of the chamber, the restriction to specific materials (vacuum-compatible, and nonmagnetic so as not to interfere with the electron beam), and the absence of thermal dissipation through convection (which is a limitation to how much heat the sensors and actuators are allowed to generate). For samples, difficulties include the fixation, loading and unloading inside the chamber, and specific conditions required for the ob-

servation of hydrated or biological samples which otherwise exsiccate. Further, observed objects have to be sufficiently conductive so as not to be electrically charged (and thus rendered unobservable or even damaged) under the effect of the electron beam - this is often, for normally non-conductive surfaces, done through metallisation.

The overview of SEM-integrated nanomanipulation platforms as described in the literature shows that electron microscopy is a viable and valued tool in micro-robotics. The main characteristics for the micro-robotic platforms found in recent papers are summarised in table 1.1: embedding into a SEM correlates with nanometre-range experiments, and with flexible degrees of freedom; both are exemplified in the specific advantages of self-sensing AFM probes.

2 Sensing and imaging through Atomic Force Microscopy

The operation of quartz probes in force sensing or mechanical characterisation, just like topographical imaging, finds its roots in Atomic Force Microscopy (AFM). This particular branch of local probe microscopy was developed by Binnig, Quate and Gerber in 1986, following the invention of the Scanning Tunneling Microscope (STM). AFM and STM have since been preeminent methods of observation and measurement at the nanoscale and below. Although AFM can be used for manipulation, i.e. the pushing and positioning of small objects, this aspect will not addressed here, the focus being on force sensing and imaging. This section will first summarise the general principles and control modes of AFM, then the use of tuning forks as AFM probes, the medium specificities of ambient and liquid environments, and the evolution towards faster AFM imaging.

2.1 General principles of AFM

AFM as it was first conceived [Binnig 86] consists in using a cantilever as a probe: a soft horizontal beam, clamped at one end and with a sharp vertical tip at the other; this initial setup also allowed some degree of observation under an optical microscope. Countless other applications based on AFM were then developed. AFM can be combined together with another observation technique, such as optical microscopy for coarse positioning, an electron microscope for more precise yet relatively large-scale observation, or complementary tools such as fluorescence [Fukuda 13] for biological applications.

2.1.1 AFM modes

The term AFM in and of itself only describes the use of nanoscale force sensing, but can refer to very different ways of using a probe. There are three main variations of AFM:

- contact mode, or static mode: the cantilever's tip is and remains in contact with the imaged surface, and the beam's deflection is measured - usually through laser reflection (Fig. 1.7). During the scan, the cantilever or the substrate are moved along the vertical

Table 1.1 - *Characteristics of SEM-integrated micro-robotics platforms (blank when no informations available).*

	Actuators	Degrees of freedom	Step / Range	Applications
Oldenburg [Eichhorn 12]	Smaract (coarse)	2 DoF + rotation	10 nm / 35 mm	micro-assembly, automatisation, Carbon
	Physik Instrumente - Hera (fine)	3 DoF	1.55 nm / 50 µm	nanotubes, NEMS, multiprobe
Nagoya [Yang 12]	Picomotors TM (coarse)	2 DoF + rotation	30 nm /	cell tests (stiffness, adhesion, electrical),
	Nanomotors TM, PZTs (fine)	3 DoF, 6 DoF (3 rotations); 3 DoF (2 rotations)	2 nm /	thermometer, Carbon Nanotubes
Shizuoka [Takahashi 11]	New Focus Picomotor (coarse)	1 DoF (z)	/	biomanipulation,
	Piezo (fine)	1 DoF (z)	/	haptics,
	Parallel spring stages (fine)	2 DoF (x,y)	/	multiprobe
Toronto [Ru 11]	Zyvex S100	4x 3DoF	100 nm / 12 mm 5 nm / 100 µm	nanowires, nanorings, 4-probes characterisation, mechanical, electrical
Toronto [Zhang 13]	Smaract	2x 3DoF	100 nm / 11 mm 0.7 nm / 1.2 µm	lock-load manipulator, assembly, nanowires
Tennessee [Qin 12]	Unisoky STM	4x 3DoF	µm / 3-5 mm nm / 1.5 µm	nanowires, STM multiprobe
Sheffield [El-awayeb 12]	Kleindiek	2x 3DoF	nm / mm	nanowires, electrical characterisation
Karlsruhe [Boles 12]	Kleindiek	3DoF	nm / mm	AFM, mechanical characterisation

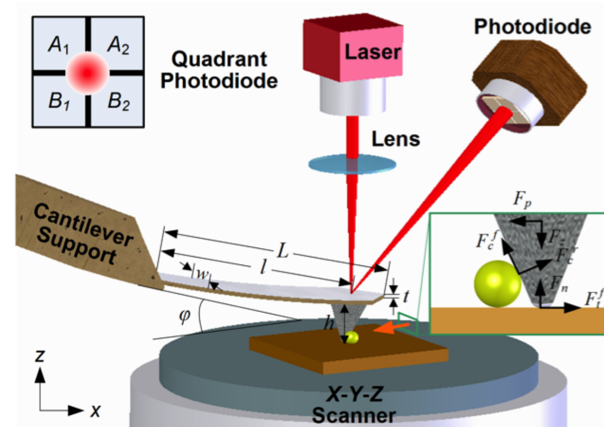

Figure 1.7 - *AFM setup with a photodiode measuring laser deflection [Xie 12a].*

axis so as to maintain a constant application of force. This mode obviously involves high forces and frictions, and can damage both the tool and the observed surfaces.

- "non-contact" or "near-contact" mode: the cantilever is excited by an oscillator and vibrates close to its resonance frequency. When the tip is brought onto the surface of the sample, the interaction forces influence the frequency, amplitude and phase of the oscillation, whence data is extracted to reconstitute an image. The oscillation amplitude must remain small, at a sub-nanometre or even sub-Angström scale, to remain within the range of attractive forces (Fig. 1.8).
- "tapping" mode: this hybrid dynamic mode somewhat combines contact and dynamic modes. The cantilever is also excited, and the tip only briefly touches the surface, near the desired maximum amplitude when the oscillating movement reaches its end. This mode usually uses greater oscillation amplitudes than pure non-contact modes, as it needs to be able to pull free from adhesion forces.

"Tapping" is often chosen when imaging in air or liquid environments, but "non-" or "near-contact" modes are preferred in very controlled environments where oscillation is least disturbed, e.g. high vacuums, and this work will later focus on them.

2.1.2 Dynamic AFM control modes

The tapping and near-contact modes are dynamic modes, having in common that the probe is made to oscillate. The oscillation can be controlled in:

- amplitude modulation (AM) – the "tapping" mode always uses amplitude control
- frequency modulation (FM) and phase modulation (PM)

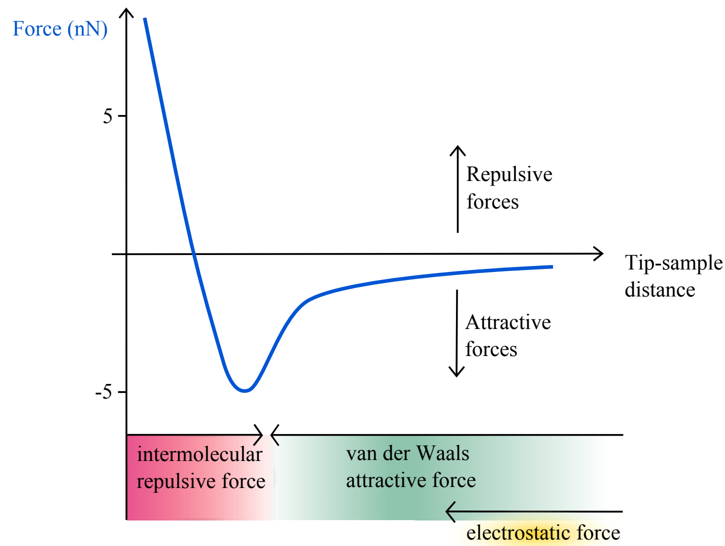

Figure 1.8 - *Repulsive and attractive intermolecular force zones on the pull-in curve. The point where repulsive contact forces start to contribute corresponds to the "pseudo-contact" zone.*

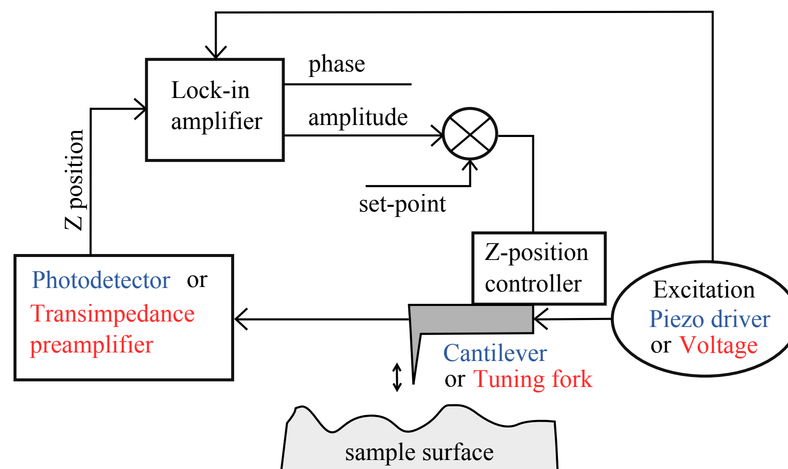

Figure 1.9 - *AM-AFM mode block diagram.*

Where contact modes sense repulsive forces in constant contact with the surface, AM-AFM for dynamic probes [Zhong 93], which now often refers to the more specific "tapping mode", is based on the principle of the probe's oscillation at a chosen frequency being interrupted by only intermittently touching the surface at a set force intensity value, usually at around 90% of the probe's oscillation amplitude. AM-AFM is generally considered as the most stable mode in environments that aren't especially well controlled, e.g. air and liquids. This mode of operation is naturally more damaging to the tip and sample.

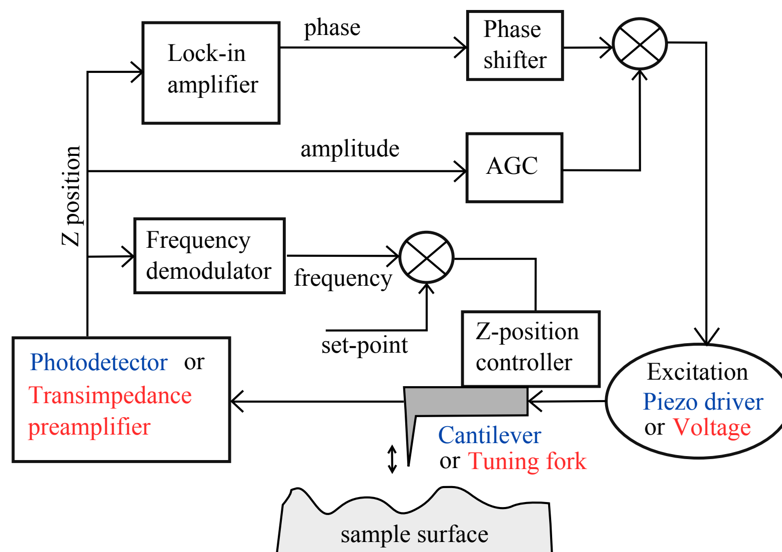

Figure 1.10 - *FM-AFM mode block diagram.*

FM-AFM [Albrecht 91], as a "non-contact" or "near-contact" mode, is more sensitive to small oscillations. Albrecht and Grütter first used frequency modulation as it improved the quality factor of the probe by one order of magnitude in a medium vacuum. FM-AFM uses fixed oscillation amplitude and phase, or fixed drive amplitude and phase. The probe stays near the surface at all times and senses attractive or repulsive forces which affect the frequency of the oscillation. Atomic resolution by FM-AFM was first achieved on silicon by [Giessibl 95].

PM-AFM is comparable to the FM technique but uses a simplified setup, which eliminates several risks of instability in hazardous environments, and could possibly achieve higher resolutions in a vacuum [Fukuma 06]. 0-PM, a variation on this concept, includes phase-shifting back to 0 when the tip is near the surface, yielding optimal control conditions for the technique [Pham Van 08].

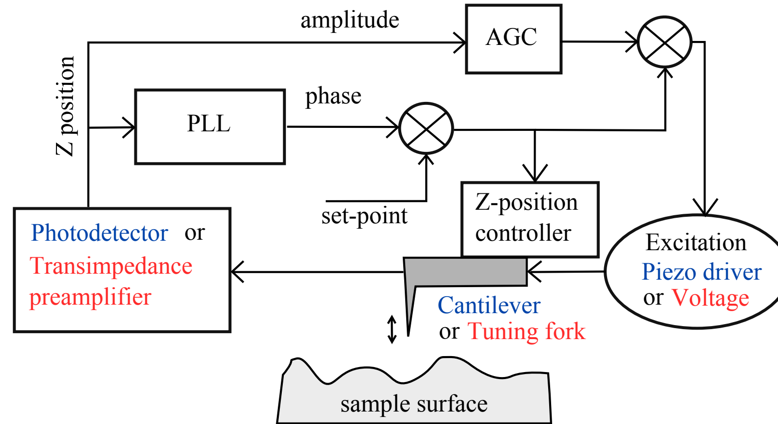

Figure 1.11 - *PM-AFM mode block diagram.*

"Non-contact" modes are the most popular when it comes to reaching high resolution images, whereas AM-AFM is rather used for biological or video-rate dynamic imaging. In micro-robotic applications, cantilevers have been a forefront tool even without AFM feedback; as dynamic sensors, they provide both force measurements and additional position data beyond the resolution of electron microscopy. The addition of self-sensing quartz resonators to the fold brings now, with tuning forks, AFM technology that is unimpeded by laser positioning and adapted to flexible operations. This flexibility is especially important in micro-robotics, in which not only positions but approach angles may need to be controlled, in a SEM or with dynamic reactivity (neither case leaving room for the recalibrating and repositioning of laser feedback).

2.2 Tuning fork AFM

Tuning forks are acoustic resonators shaped with two prongs (or tines). This geometry results in an especially pure fundamental frequency. Tuning forks have been used since the 18th century to tune musical instruments, then later in their miniaturised form as components in watches, gyroscopes and other portable devices, and have as such become one of the foremost resonators amongst standard electronic components.

With the addition of a tip, these quartz tuning forks (QTF) were successfully used as AFM probes [Edwards 97] after they were reported for near field optical microscopy applications [Karrai 95]. As their oscillation control and the shift in their behaviour are both tracked electronically, these self-sensing probes do not require a mechanical excitator nor an optical detection setup. One configuration in which tuning forks are so used, called qPlus [Giessibl 98], consists in fixing one of the tines to a supporting structure, severing the link between the tines. This halves

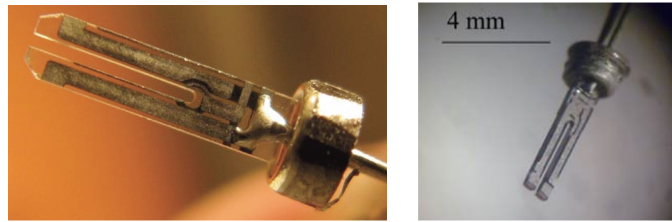

Figure 1.12 - *Tuning fork*

the stiffness of the resulting probe and results in a structure with a better-known mechanical behaviour, at the cost of a great loss in quality factor. Other models were then developed that address the whole quartz tuning fork [Castellanos-Gomez 10] [Kim 14] [GmbH 05], in order to fully take advantage of its inherent sensitivity. Yet another tuning fork based self-sensing probe design, the Akiyama Probe or A-Probe, combines a silicon microcantilever with the tuning fork in order to obtain a much softer tip and inflict less damage on samples [Akiyama 03].

Probes based on tuning forks have reached the atomic resolution both in a vacuum [Giessibl 00] and in ambient conditions [Wastl 13].

2.2.1 Operating principle

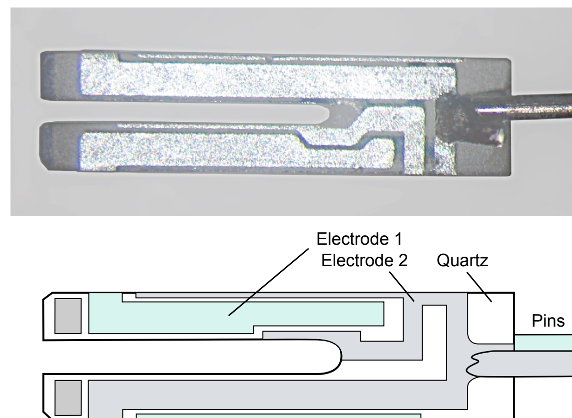

Figure 1.13 - *Tuning fork electrodes. The disposition can vary slightly across manufacturers.*

The quartz crystal fork, which is the main component of a tuning fork, vibrates when excited by the electrodes placed on each tine (Fig. 1.13). The oscillation amplitude can be brought down under a nanometre, a few Angströms, or less. Standard and commercially available electronic models only oscillate in the anti-phase coupled mode (1.14) due to the geometrical disposition of the electrodes – tuning fork shapes can otherwise also oscillate in coupled phase or transversal

modes [Castellanos-Gomez 10].

A tuning fork possesses an inherently high quality factor Q, defined as the quotient of its fundamental frequency f_0 by the corresponding resonance's bandwidth. Q is indicative of the rate at which the tuning fork is dampened, and factors in its sensitivity (see Section 1.3). A higher Q therefore results in the probe being able to sense smaller interaction forces, which also leads to better image resolutions in AFM.

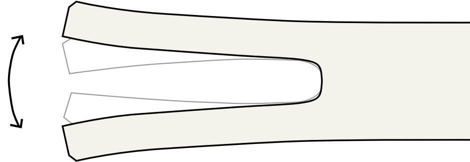

Figure 1.14 - *Tuning fork antiphase oscillation mode*

To use a tuning fork as a self-sensing probe, voltage is applied to its electrodes and the feedback current first goes through a preamplifier. To drive and obtain signal from the resonant mode, the cables and tuning fork's stray capacitance must be compensated in order to avoid anharmonic effects, which can be done in a variety of ways: manually with a variable capacitor; with a second QTF, in order to match the exact capacitance value of the first [An 13]; or by digital compensation, which provides better capacitance-tuning resolution [Peng 15]. The signal then goes to the appropriate controllers – e.g. in AM-AFM, a lock-in amplifier which separates the phase and amplitude of the signal; in FM-AFM, an AGC (Automatic Gain Control) and PLL (Phase-Locked Loop) controllers maintaining both phase and amplitude constant to analyse the frequency shift when interacting with a surface.

2.2.2 Force measurement

Force sensing by AFM technology is used not only for the topographical reconstruction of images, but also directly for relative or quantitative force sensing. One example is the deflection of cantilevers for mechanical characterisation through nano-indentation, though this is an inherently destructive process. Other methods consist in using an intermediary object – [Arai 03] observes by SEM the deflection of a CNT (Carbon Nanotube) held at the end of a cantilever.

Tuning forks, like cantilevers, have been used as force sensors for numerous applications, ranging from magnetic force microscopy [Seo 05] to biosensors [Su 02], microbalances [Nihei 10] and density or viscosity measurements in gas or liquids [Sell 11, Toledo 14]. The laserless setup of quartz tuning fork probes has now also been exploited by micro-robotic applications in combined use with electronic microscopy , covering the mechanical characterisation of nano-objects [Acosta 11] or force-sensitive manipulation of CNTs [Oiko 14].

The critical parameter in using tuning fork based probes as force sensors is the stiffness of the tuning fork, which will be referred to as k_{probe} or k_{eff} in this work, and which appears in any expression of quantitative force measured by the probe. Contemporary works have calibrated

tuning fork sensors through the deflection of pre-calibrated AFM cantilevers [Oiko 14], though due to the use of an angled tip this requires a new calibration for each tuning fork probe. Another means of characterising the stiffness is to physically indent the quartz probe [Shaw 14]. Non-invasive methods of measurement [Castellanos-Gomez 10] include thermal noise measurement; the Cleveland method, which measures the resonant frequency before and after adding a small mass; or a ratio of the in-phase and anti-phase frequencies, though this isn't applicable on standard commercial tuning forks due to the disposition of the electrodes (which imposes the anti-phase oscillation mode and is itself necessary to their proper operation). Lastly, theoretical models exist that deduce the stiffness value from geometrical parameters, with adjustments based for instance on a coupled oscillator system [Castellanos-Gomez 10] [GmbH 05] – this model is however controversial beyond the specific tuning fork model it was developed for, and is opposed by other experiments in the literature: other models hence deduce the stiffness from frequency measurements [Kim 14] or FEM simulations [Gonzalez 15]. The subject of effective stiffness k_{eff} is further detailed in Chapter 2, Sect. 1.2.

2.2.3 Conservative and dissipative forces

When considering the interaction dynamics of the surface with an oscillating object – here the oscillating tip – one aspect of the micro-scale forces sensed by AFM which comes into play is whether their components are of a conservative or non-conservative nature. Its definition is thus: the work W associated with a conservative force does not change for given beginning- and end-points of the resulting motion of an object, and the overall work is therefore null for a back-and-forth oscillation cycle. Conversely, W is not path-independent for a non-conservative force which results in energy dissipation. Examples of conservative forces are spring forces, gravity, or some attractive components of van der Waals forces; non-conservative forces include any lateral or friction force, which notably accounts for the changes in the quality factor of oscillating resonators in ambient or fluid environments (see Sect. 2.3 and Chapter 2). Distinguishing these forces can provide more insight into sensor data and be instrumental in the study of micro-scale interactions, for instance fluctuations in electromagnetic interaction such as Casimir forces [Dedkov 09]. Atomic Force Microscopy can to some extent apply such a distinction – although, because the net conservative component can be the combined effect of several other factors, [Sader 05] instead of *conservative* and *dissipative* favours in this context the terms *even* and *odd*. The underlying fundamental assumptions are the basis of tip-sample force measurements, which will be touched on in Chapter 4.

2.2.4 Stiffness measurement

The stiffness to be measured is here a mechanical characteristic of micro-samples (k_{sample}), such as will be conducted in Chapter 4, and is to be distinguished from calibrating the stiffness of the tuning fork probe (k_{probe} or k_{eff}). Stiffness measurement is derivative of force measurement in the Frequency Modulation mode. The relation between FM-AFM frequency shift Δf and sample stiffness k_{sample} can be obtained using the coupled oscillators model presented in [Castellanos-Gomez 10] (Fig. 1.15) which, unlike single-cantilever models, considers that the oscillation

dynamics are affected by a coupling of the two tines of the tuning fork – with each tine a harmonic oscillator modelled as a clamped beam. With effective masses m and spring constants k, and k_c modelling the coupling between the masses, the system is written as:

$$\begin{bmatrix} m & 0 \\ 0 & m \end{bmatrix} \begin{Bmatrix} \ddot{x_1} \\ \ddot{x_2} \end{Bmatrix} + [K] \begin{Bmatrix} x_1 \\ x_2 \end{Bmatrix} = \begin{Bmatrix} 0 \\ 0 \end{Bmatrix} \tag{1.1}$$

where x_1 and x_2 represent the motion of the masses. For a free resonating tuning fork,

$$[K] = [K_{free}] = \begin{bmatrix} k + k_c & -k_c \\ -k_c & k + k_c \end{bmatrix} \tag{1.2}$$

When the probe is in contact with a sample,

$$[K] = [K_{incontact}] = \begin{bmatrix} k + k_c & -k_c \\ -k_c & k + k_c + \Delta k \end{bmatrix} \tag{1.3}$$

with Δk representing the effective stiffness of the combined tip and sample,

$$\Delta k = \frac{1}{\frac{1}{k_{tip}} + \frac{1}{k_{sample}}} \tag{1.4}$$

The resolution of this model provides in-phase and anti-phase eigenmodes. The anti-phase solutions, respectively for a free and in-contact probe, are ω_0 and ω_1:

$$\omega_0^2 = \frac{k + 2k_c}{m}, \omega_1^2 = \frac{2(k + k_c) + \Delta k + \sqrt{4k_c^2 + \Delta k^2}}{2m} \tag{1.5}$$

$$\omega_1^2 = \frac{2(k + k_c) + \Delta k + \sqrt{4k_c^2 + \Delta k^2}}{2m} \tag{1.6}$$

Assuming a small $\Delta k \ll k_c$, and

$$\omega_1^2 = \frac{2(k + 2k_c) + \Delta k}{2m} \tag{1.7}$$

the corresponding eigenfrequencies being f_0 and f_1, the frequency shift in contact is:

$$\frac{\Delta f}{f_0} = \frac{f_0 - f_1}{f_0} \simeq \frac{1}{2} \frac{\Delta k}{2(k + 2k_c)} \tag{1.8}$$

whence Δk is obtained. It is assumed that the tip is much stiffer than the sample, and therefore $k_{sample} \approx \Delta k$. The resolution of this model gives k_{sample} proportional to Δf factored by the sensor's sensitivity

$$k_{sample} = \left(\frac{2k_{probe}}{f_0} \right) \Delta f \tag{1.9}$$

with k_{probe} the effective elastic constant of the whole tuning fork probe, including the added probe tip and its counterweight.

Tuning fork probe stiffness measurement is applied on micro-membranes in this work (Chap. 4, Sect.2) using the coupled oscillators model. Another coupled oscillators model [GmbH 05] puts the emphasis on modelling the influence of the balance of symmetry using a third mass.

One must note that while this spring-mass model is indeed used for practical purposes, since it yields satisfying results with 32.768 kHz tuning fork components, it does not necessarily reflect the physical reality of the tuning fork oscillation phenomenon, as is pointed out in a comparison with different models of tuning forks with various eigenfrequencies [Kim 14].

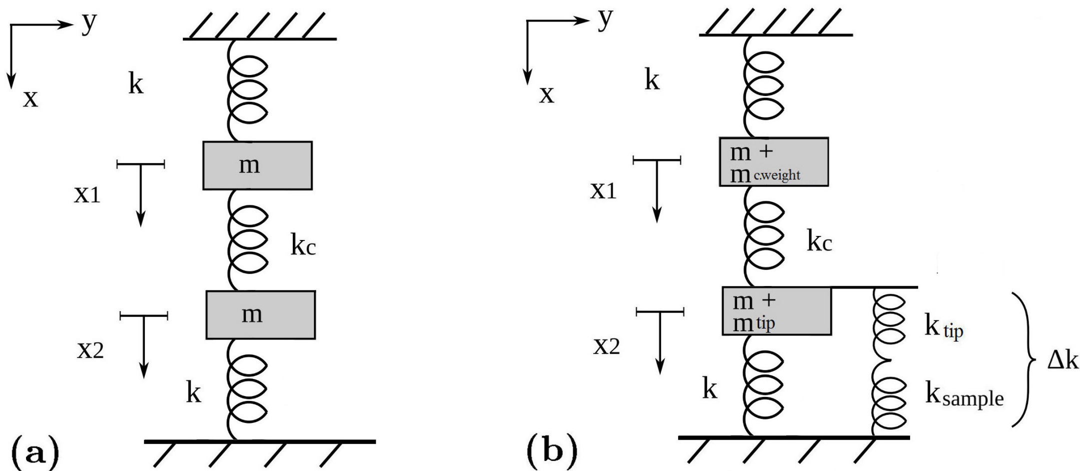

Figure 1.15 - *[Sauvet 13] Spring-mass mechanical models of (a): a free tuning fork [Castellanos-Gomez 10], and (b): a tuning fork with a probe tip in contact with a sample. Both prongs have the same mass m and stiffness k; k_c models the coupling between the prongs; the tip and the counterweight have the same mass m_{Probe}.*

2.3 AFM environments

The environment is a determining factor in AFM, and through its effect on tip-sample interaction as well as dissipation (expressed through the factor Q) will influence the sensitivity and reactivity of quartz probes – this will be later detailed in the first sections of Chapter 2 on the mechanical properties of tuning forks, and Chapter 4 concerning the differences between air and vacuum environments.

In the dynamic control modes, friction against air molecules further dampens the oscillation; in the case of quartz tuning forks in particular, the high quality factor sought by manufacturers decreases to around a tenth of its value outside of the vacuum container the components are packaged in, and decreases further in more difficult fluid environments. As mentioned earlier, this may affect the choice of AFM mode (the "tapping" mode being less affected in air or liquid environments, whereas the "non-contact" modes benefit from high vacuum environments), but the limitation does not rule out exceptional performances – the qPlus sensor having reached the atomic resolution in ambient conditions [Wastl 13] as well as in a vacuum. In ambient or nitrogen environments, observations using tuning forks have also been made on biological objects such as bacteria, cells, biomolecules [Otero 12] and the mechanical forces inherent in biological processes like the withdrawal of BSA proteins [Polesel-Maris 12]. Uses in micro- manipulation have also extended to ambient environments with the exfoliation of two-dimensional objects [Island 15].

Liquids are a much more challenging environment, in which the use of AFM is often motivated by the necessity to observe specific biological or soft samples– or even, for atomic-resolution AFM, to observe the liquid itself. When in the presence of an air-liquid interface, a meniscus is formed by the condensation between the tip and the substrate, which attracts both [Weisenhorn 89]. The order of magnitude of the corresponding force is 10 to 100 nanoNewtons [Baselt 93]. The

viscoelasticity [An 13] and rupture dynamics [Bak 15] of these menisci, or water-bridges, have been studied thanks to the high stiffness of quartz tuning fork probes overcoming jump-to-surface effects. For AFM seeking to operate in liquid environments, both the samples and the tip are often entirely immersed in liquid in order to avoid this phenomenon. However, the effect on van der Waals interaction forces when objects are completely immersed, as is evidenced by the values of the Hamaker constant [Weisenhorn 89], significantly affects sensing capabilities. Applications have been developed for AFM imaging in liquids, some of them imitating the concept of wet diving bells for a higher quality factor [LeDue 09], including tuning fork AFM [Koopman 03]. AFM techniques can also be exploited in liquids as a complementary measurement for other experiments, such as capture or deposition with a nanopipette attached to a tuning fork [Ito 11]. Tip preparation and conditioning are even more significant in liquid media, as the tips can be coated to grant them beneficial properties – making them hydrophobic to reduce friction, bio-inert, magnetically neutral... In biological or chemical applications, the tips can be coated with substances to detect binding events or interact with targeted elements, e.g. having them bind with certain parts of a cell [Lehenkari 00]. Liquid environments will not be explored in this work, but these applications are to be considered as specific potential uses for the base tools which will be used in air and vacuum environments.

2.4 High-frequency AFM

Quartz probes as found in the literature have for the most part been limited to 32 kHz tuning forks. Attaining higher oscillation frequencies for dynamic AFM allows the characterisation of dynamic phenomena, or the obtention of images at a faster speed [Brown 13], thus palliating the downside of local probe microscopy being slow, especially for larger surfaces. This will motivate the push towards higher frequency probes in Chapter 3.

Parameters affecting imaging speed are the feedback bandwidth, the sample's spacial frequency and fragility, and imaging conditions. One solution which consists in concurrently using several probes in parallel [Minne 95] can result in raster scanning with up to 50 tips, reaching speeds up to several mm/s [Minne 98]. However, this solution has proven to be too impractical both for research and commercial applications.

Some commercial packages rather opt for other types of resonators, such as the KolibriSensor™'s 1 MHz length extensional resonator (LER or "needle sensor") which operates at 1 MHz. These quartz sensors have achieved atomic resolution imaging [An 08, Torbrügge 10], and can be applied on soft materials in ambient and liquid environments [Froning 15]. Giessibl et al. have compared these LER probes or "needle sensors" to qPlus probes for these applications, showing that the needle sensor, with a 600 times greater stiffness than the qPlus (1080000 to 1800 N/m), presents 16 times lesser deflection sensitivity (45 $\mu C/m$ to 2.8 $\mu C/m$) [Giessibl 11]. The comparison finds the qPlus sensor to have superior signal-to-noise thanks to its geometry and stress profile, while noting that the longitudinal shape of the LER sensor is favourable to reduced microscope dimensions.

Another option towards increasing frequency is overtone excitation on given quartz components. The first inharmonic overtone for tuning forks corresponds to about 6 times the

fundamental frequency, which is around 190 kHz for 32 kHz QTFs. Despite findings in the literature on cantilevers [Dohn 05] indicating that overtones must have considerably higher quality factors than their fundamental modes, most commercial models are designed and optimized for fundamental mode excitation, and their overtone modes therefore tend to have low quality factors (see Chapter 2). The models which still present satisfying quality factors are also found to yield very low signal [Babic 15]. Aside from these limitations, a study on the potential improvements of overtone excitation with the qPlus scheme has further emphasized the effects of tip length and suggested its use to tune the properties of the probe [Tung 10].

Overall, the most widely used solution is however the reduction in size and mass of the resonators in order to raise their eigenfrequency. Self-sensing alternatives to quartz resonators follow this trend [Ruppert 13, Melcher 14, Buchaillot 14], and quartz tuning forks themselves are being miniaturized [Gil 11, Wei 14] and optimized [Barbic 07]. These solutions are naturally confronted to limitations inherent to the currently available fabrication techniques. Non-self-sensing cantilevers, which are easier to manufacture in micro-sizes, have been used especially in the tapping mode [Ando 08, Ando 12]. Such micro-cantilevers were first developed for fast imaging in a liquid environment [Ando 01]. The goal of reaching higher imaging speeds (100 ms/frame [Uchihashi 06]) has been pursued by several groups for the monitoring of dynamic biomolecular events, applying the microcantilever technique to obtain up to "video-rate" imaging at 20 FPS (human chromosomes in liquid [Picco 08]). This yielded famously impressive results such as the "real time" imaging of a walking myosin V [Kodera 10]. However, the area covered by these systems has remained very limited, around a few micrometers (e.g. 1x4 μm). While this was sufficient for some biological elements like proteins, it didn't allow the observation of dynamic phenomena at a greater scale, or involving greater objects such as cells. Recent efforts have attained yet larger imaging capabilities but may be reaching the limits of such systems with the emergence of greater technical difficulties: 46 FPS imaging on up to a 23x23 μm zone (e.g. 8 to 11 mm/s) has images distorted due to an atomic stick-slip effect [Braunsmann 10]; slower imaging at 3 FPS on a 46x46 μm zone [Watanabe 13] brings to evidence an increasing significance of the actuators' dynamic behaviour (hysteresis, vibrations, etc.).

Aside from AFM research itself, high-speed tapping AFM using the microcantilever reduction model and its so-called "real time" derivation are now commonly used, essentially to observe various biological phenomena [Noi 13] – as the tapping force applied by these microsystems can be very small ($<$ 100 pN [Ando 13]), it is non-invasive. The downsides are lesser resolution and the increased presence of artefacts in the obtained images. Such low-range, real-time and biology-oriented applications will however not be the goal of this work, as they are highly specific and cannot be adapted together with the advantages of self-sensing probes at this time.

3 Objectives

Current research in micro-robotics and atomic force microscopy (AFM) shows that there is interest in self-sensing and self-exciting resonator probes for applications in imaging, force sensing, and mechanical characterisation. Sensors destined for such micro-applications must first of all be embedded in global actuation and control setups adapted to the scale and phenomena

of the micro-world, including some degree of visual feedback. Beyond the limitations of optical microscopy, Scanning Electron Microscopes (SEM) are notably prized for the *in situ* observation of samples in real time, with greater resolution and field of view. This is evidenced in the integration of micro-robotic platforms into SEMs towards very different experiments, with greater adaptability being pursued through actuation and increased degrees of freedom, the overwhelming majority by making use of piezoelectric actuation platforms. Efficient and flexible experimental systems are to be achieved through complementary work both on specific sensors and their integration and control through these actuation platforms.

With self-sensing resonators, experimental setups benefit from reduced encumbrance and less constraining technical requirements: the self-sensing principle of operation dispenses with the need for laser detection or external excitation. This expands the potential capabilities of micro-systems as a whole in two major ways. The first is dexterous control over the three-dimensional orientation of the end probe, unimpeded by the challenges of laser positioning; the second is compactness, which readily enables the integration of these systems into SEMs, thus making quartz probes suitable tools for SEM-controlled profilometry and characterisation on targeted areas of samples. The aim here will be to build on self-sensing AFM technology as it is used in such applications, by studying, improving and exploiting self-sensing probes, their environment and their control in flexible experimental systems.

This work will hence focus on quartz probes. The questions raised will be how to build and calibrate probes with known properties, how to achieve quantitative results and handle the actuation control of the sensors towards these results, and how to raise their frequency for faster operation.

In addition to both the excitation and sensing of quartz probes being conducted electronically and therefore easy to remove outside of a confined SEM chamber, the lower heat dissipation and temperature sensitivity (compared to the lasers of optical AFM setups) are of interest in controlled environments. The use of off-the-shelf, standard electronic components also allows the fabrication of customisable systems in a standard lab environment. Inversely, while one of the most direct ways to improve the performance of these tools is to increase their fundamental operating frequency for greater reactivity and speed, the common solution found in the literature, which consists in reducing their size down to the micro-scale, comes with significant demands in design, optimisation and manufacturing, and is confronted with the limitations of current fabrication techniques.

The popularisation of quartz tuning fork (QTF) probes has made it possible to build characterisation and imaging systems without the need for micro-machining equipment, by attaching a tip to a standard resonator, and we seek to expand this to higher frequency components. The next chapter will therefore be dedicated to examining the design and fabrication process of quartz probes, and how it may be adapted to higher frequency quartz resonators. The selected sensors will be tested and compared to QTF probes for ambient imaging in chapter 3. Using an actuation platform designed for a SEM and vacuum environment and tailored control tools, Chapter 4 will then study the specificities and challenges related to this environment, before establishing a proof-of-concept for stiffness characterisation applications by quartz probes together with SEM vision.

Chapter 2

Micro-robotic probes designed from standard quartz resonators

The quartz resonators used in this work are standard electronic components. We follow in this the design of self-sensing probes based on tuning forks seen in the previous chapter, which benefit from the wide availability of consistent, standard and optimised models. Although such components are sensitive enough to detect micro-scale phenomena, their dimensions are above a millimetre, and they are adapted to local micro-scale experiments only through the addition of a tapering micro-tip. In addition to selecting a suitable component, the improvement of quartz probes by using different base resonators will therefore be subjected to considerations as to how to adapt them with a tip, as informed by their oscillation properties.

This chapter thereon deals with the characterisation, fabrication and improvement of force-sensing probes with various off-the-shelf quartz resonators, starting with tuning forks as in the literature (32.768 kHz). First examined are the mechanical properties of these resonators and the manual fabrication process of adding a tip to the quartz component, which will be relevant to every experiment conducted in this work. We then evaluate the available options for higher-frequency resonators and their adaptability, in order to select likely candidates for the fabrication of higher-frequency probes. The chapter concludes with the finite element modelling of a thickness shear quartz resonator, selected for the fabrication of a MHz-range sensor, in order to understand its oscillation mode and how to fit it with a tip. The resulting probes will be tested for their performance in AFM imaging in the next chapter.

1 Mechanical properties of tuning forks

The first step in fabricating probes using pre-existing quartz components is understanding the workings of resonators as relate to sensing, in order to select one accordingly. This section hence deals with the characteristic properties of tuning forks – their quality factor, stiffness and sensitivity – and how they will be used to gauge their potential performance as force-sensing probes. These same properties will be the parameters to be considered for quartz resonators of different kinds, and all the experiments conducted in this work will similarly rely on these concepts.

1.1 Quality factor

The quality factor Q of a quartz resonator, as mentioned in the previous chapter, is defined as the quotient of its fundamental resonant frequency by the -3 dB bandwidth at the resonance:

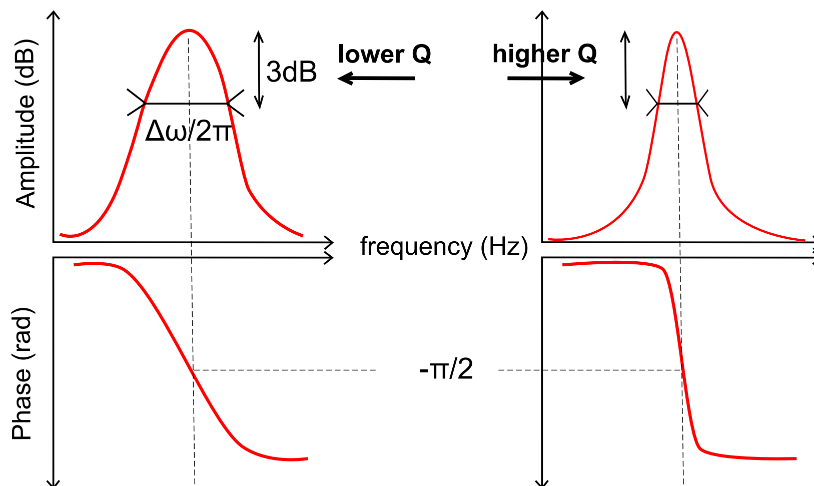

Figure 2.1 - *Q factor and -3 dB bandwidth of a resonance curve.*

Q is a dimensionless indicator of how dampened the system is, i.e. the number of oscillations the resonator will yield for a given amount of energy if the initial excitation is no longer maintained. As such, it will decrease the more factors there are that impede the oscillating motion. Typical Q values for tuning forks are up to 50,000 in a vacuum, and 5,000 to 10,000 in air due to the friction with air molecules. When a significant part of a tuning fork probe is immersed in liquid, Q easily drops to less than a few dozen units.

A high quality factor corresponds to a "sharp" resonance amplitude on an amplitude-phase

Bode diagram. Generally speaking, a high quality factor is desired when using quartz resonators as sensors, be it for mechanical characterisation or AFM imaging, as it increases the sensor's sensitivity i.e. its resolution (see Sect. 1.3 below). However, [Giessibl 11] when aiming for atomic resolution states that with given electronic equipment, too high a quality factor can be detrimental to the system's performance. In addition, for the purpose of AFM scanning, the optimal value of Q may be subjected to a compromise between speed and sensitivity. Methods have been developed for this value to be electronically enhanced or decreased, by injecting energy in or out of phase, respectively prioritizing sensitivity or response time (and with it scanning speed) as desired [Jahng 07]. Due to the nature of AFM applications and the many parameters involved, there has yet been debate regarding the extent to which electronically increasing the value of Q affects the optimal performance of given systems. The effects of environment- or load-related dissipation, as correlates with their impact on Q, will be studied more in depth in Chapter 4.

1.2 Stiffness

The stiffness referred to here is again that of the quartz resonator itself, k_{probe}, and not the stiffness of a sample as measured by a probe, k_{sample} (described in Chapter 1, Sect. 2.2.4). Stiffer resonators will tend to be less sensitive (see Sect. 1.3 below); however, a balance must be struck between sensitivity and practicability, since a sensor that is too flexible will be attracted and snap to contact when brought close to a surface. Both in tapping and near-contact modes, the ideal stiffness is one that allows the sensor to be brought close enough to the surface for the desired degree of contrast and detail to be obtained.

An accurate value of the sensor's stiffness will be critical to obtaining quantitative measurements in force or stiffness sensing. However, simply considering a tuning fork as a couple of clamped beams can be erroneous, as the base of a tuning fork doesn't constitute true clamping (Fig. 2.2): the effective length of a tine, if the classical beam model is to be applied to it, isn't equal to the free length of the tine and is therefore unknown. Some mechanical coupling between the two tines has besides been hypothesised, as well as a weak piezoelectric reaction resulting from the quartz deformation during the oscillation – though the latter effect is thought to be negligible.

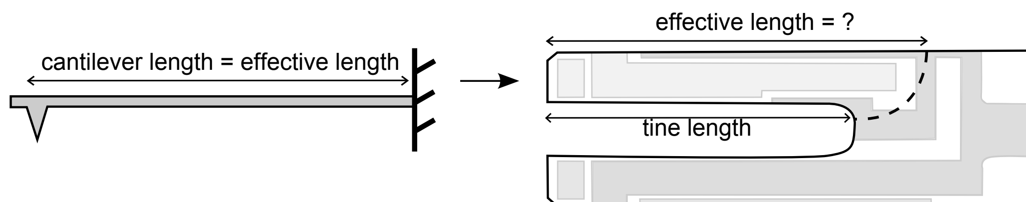

Figure 2.2 - *Disparity between cantilevers and QTFs with regard to the mechanical model of a fixed beam: the effective length of a tuning fork is uncertain, as there is no actual delimitation for each quartz tine (or prong).*

The stiffness value of the whole tuning fork system will be referred to as the effective stiffness. Several methods exist to physically evaluate a tuning fork's effective stiffness [van Vörden 12]. The Cleveland or thermal noise methods, which give experimental results, are due to their technical requirements often overlooked in favour of geometrical estimations based on mechanical models [Gonzalez 15].

A convenient theoretical method [Kim 14] consists in eliminating the effective length from the stiffness of one tine:

$$K_{tine} = \frac{Ew}{4}\frac{t^3}{l} \tag{2.1}$$

with E Young's modulus, and w, t, l the width, thickness and length of the tine; by using the theoretical expression of its fundamental frequency f_0. The result provides the effective stiffness using its fundamental frequency value, which is well-known and very easy to measure, through the following relation:

$$K_{tine} = 3.83(E\rho^3)^{\frac{1}{4}} w t {f_0}^{3/2} \tag{2.2}$$

with ρ the mass density of the prong.

1.3 Sensitivity

Sensitivity corresponds to the smallest difference in signal which can be sensed, and is thus directly affected by noise. [Giessibl 11] identifies four relevant sources of noise: deflection detector noise, thermal noise, oscillator noise and thermal drift noise. During AFM scanning, the relatively high-speed operations and large bandwidth make deflection noise the prevalent source. This deflection noise is not affected by stiffness k; but at a finer level, the sensitivity of the probe is subjected to three other sources of noise which increase with $\sqrt{k}$ and k and decrease with the quality factor Q. Oscillator noise is cited as arising especially in low-Q environments, and thermal drift noise is associated with changes in ambient temperature. Lastly, the lowest noise limit as regards sensitivity is thermal noise.

It has been determined in the literature [Dürig 86] that the thermal noise limit of force measurement through non-contact frequency shift is:

$$\delta f_{th} = \sqrt{\frac{2k_{eff}k_B T}{Q\omega_0 t_0}} \tag{2.3}$$

with k_{eff} the effective stiffness of the probe, ω_0 the fundamental angular frequency, Q the system's quality factor, k_B the Boltzmann constant and T the temperature – whence the corresponding lowest magnitude force which can be sensed:

$$F_{min} = \sqrt{\frac{2k_{eff}k_B T}{Q\omega_0}B} \tag{2.4}$$

with B the bandwidth of the measurement. The quality factor Q is defined as

$$Q = \frac{\omega_0}{\Delta\omega} \tag{2.5}$$

Further, the classical model of a dampened oscillating system with mass m yields

$$\omega_0 = \sqrt{\frac{k_{eff}}{m}} \tag{2.6}$$

Therefore eq. 2.4 can be written as:

$$F_{min} = \sqrt{\frac{2k_B T k_{eff} {\omega_0}^2 B}{Q\omega_0}} = \sqrt{\frac{2k_B T m \omega_0 B}{Q}} \tag{2.7}$$

$$F_{min} = \sqrt{2k_B T B m \Delta\omega} \tag{2.8}$$

The factors of interest here being the mass m and resonator's -3dB bandwidth $\Delta\omega$ – with stiffness being notably absent from this expression, its influence transpiring completely into the -3dB bandwidth, for which experimental values are directly measured. As this bandwidth invariably increases ten- to a hundredfold for mass-produced quartz resonator components in the MHz or higher range of frequency, it becomes easy to estimate how the ultimate sensitivity that can be achieved with probes based on these components will compare to that of standard (32.768 kHz) tuning forks.

The above mentioned properties characterise the suitability of a resonator as regards sensing, and will onwards be used to vet probes and to judge and select any new resonators. These properties are also notably subjected to changes – due to added mass affecting the quality factor and, through it, sensitivity – by the fabrication process which follows.

2 Probe fabrication

The fabrication of a tuning fork probe mainly consists in endowing the resonator with a tapering tip. The process is detailed here and, even where not mentioned in the following chapters, applies to all the probes used for the experiments conducted in this work.

Tuning forks vary in size in the range of 3 to 6 millimetres long, and weigh around 2 to 7 mg, with the smallest models (e.g. Micro Crystal MS1V series) being softer and more sensitive. The vacuum canister that encapsulates tuning fork components is removed by simply applying pressure around the base of the tuning fork, where it is sealed with adhesive – whereas for other resonators sealed within non-cylindrical canisters, it is most practical for the canisters to be cut off – in this case a precision model-making saw was used. The base that supports the pins soldered on the electrodes (Fig. 2.3) can technically be removed without affecting the

performance of the component; however, this structurally weakens the contraption. As an aside, the ring surrounding the ceramic base can also be removed without damaging the ceramic base, though at great pains – this has been said to have improved the final quality factor of some models after a tip had been attached to them, supposedly by removing a loose dampening effect, but such a result has not been reproduced since.

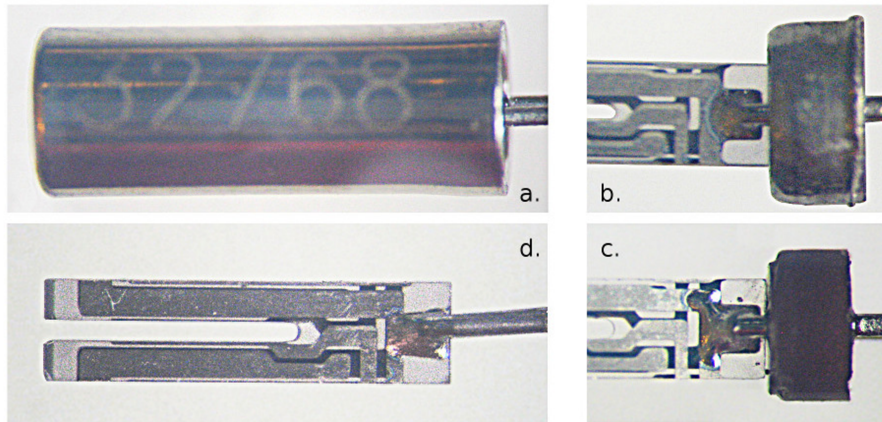

Figure 2.3 - *Tuning fork (Abracon AB38T), a. – in its standard vacuum container; b. – base ring with the container removed; c. – ceramic base with the ring removed; d. – quartz and electrodes only.*

Tuning forks will be here kept with the base and ring intact. In the case of the qPlus scheme, one prong is also affixed to a supporting structure with adhesive, halving the stiffness of the resulting resonator and reducing its quality factor; here the tuning forks will be kept whole.

2.1 Probe tip

The tip of the probe is typically a tapering piece of wire which serves as intermediary between the macro-size quartz resonator it is affixed to, and the micro-size surface or object the sensor will interact with. The length of a tip varies thus: a longer tip, up to a couple millimetres long, may lower the risks of damaging the probe or the samples; but a shorter tip is usually desirable when aiming for resolution in AFM – a length under a millimetre helps with avoiding lateral motion or excitation of the fundamental resonance frequency of the tip itself through the quartz. While its overall length may be macroscopic, the diameter of the tip progressively diminishes up to a microscopic apex.

The fabrication of these tips and consideration of the various relevant parameters constitute a research subject in and of themselves; suffice to say that standard, commercially available tips routinely end in a diameter around 100 nm or less, while custom-built tips can reach less than a dozen nanometres with various curvature angles. The tips used in this work are either commercial tungsten tips for the stiffness characterisation experiments (Chapter 4), or electrochemically etched Pt-Ir (platinium-iridium) tips with an apex diameter around 50 nm, fabricated through a process (Fig. 2.4) developed by Jérome Polesel-Maris, José Meran Meza and François Thoyer

at the SPCI (CEA, Saclay).

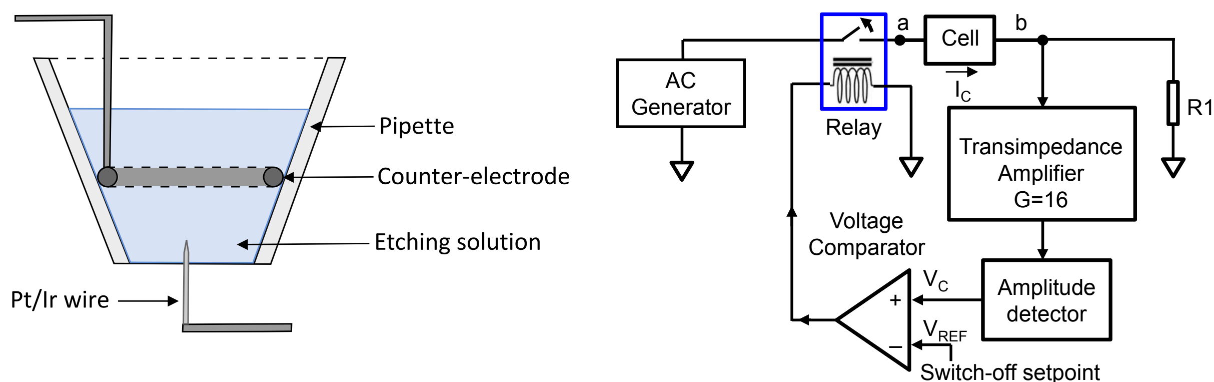

Figure 2.4 - *Electrochemical etching of a Pt/Ir wire – periodical waveforms between the wire and a counter-electrode set inside the pipette progressively shape a tip.* © *Jérome Polesel-Maris*

Figure 2.5 - *Direct etching of a tip on a tuning fork.*

This etching process consists in immersing a set length of wire into an inverted solution-holding cell, around the inside of which an electrode loop delivers pulses of voltage in periodic sequences between itself and the electrically grounded wire. The electrochemical reaction progressively shapes the wire into an apex the shape of which depends on the immersed length, preset cut-off voltage and pulse settings. While extremely elongated tips might more easily result in extremely sharp apices, they are also much more likely to bend while in use. The preferred shape for the tips as they are used here tends towards a larger curvature radius, though the optimal shape is of course dependent upon applications (Fig. 2.6).

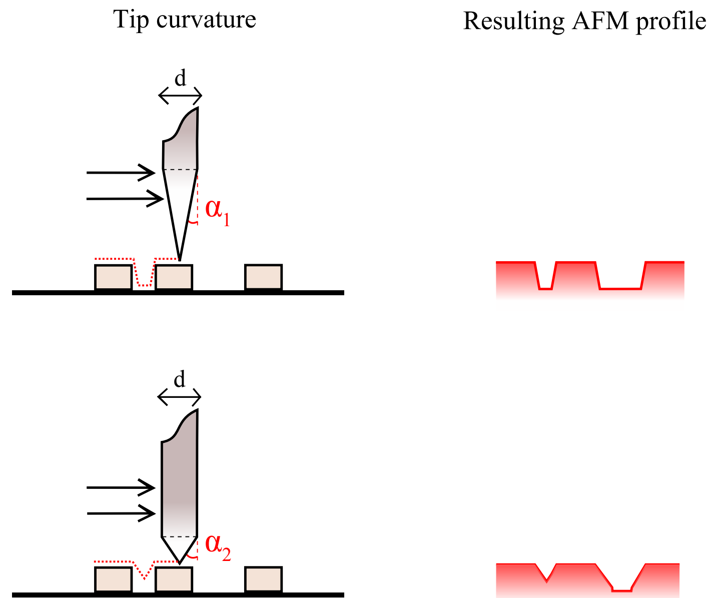

Figure 2.6 - *Influence of tip curvature on the profile obtained by AFM imaging.*

2.2 Adhesive and balancing

The tip is manually fixed on the resonator. The chosen adhesive must create as stiff a fixation as possible, and be applied in the least possible amount. Several types of adhesive can be used for that purpose; those that were used in this work are strong glue (cyanoacrilate), epoxy, and hot-air soldering paste. Although no extensive testing procedures were conducted, it would seem that glue has the least fricative impact on the deformation of the surfaces it is applied to, while still being a satisfactorily stiff fixation at least in the case of non-contact sensing. When a conductive adhesive is required, conductive epoxy, despite taking curing times of up to an hour in order to polymerise, is the best choice – for its spread is better controlled and its density ($\sim$ 2.35 g/mL) lower than that of soldering lead paste ($\sim$ 4 g/mL). When conductivity isn't necessary, glue is by far the least dense ($\sim$ 1 g/mL) and lightest in the applied quantities.

- When relying on custom-made tips, a non-essential yet non-negligible advantage to using conductive adhesive is that it allows the electrochemical etching of a tip *after* it has been stuck to the resonator (Fig. 2.6), eschewing the considerably more minute task of manipulating an already-etched and therefore shorter and fragile tip; its disadvantage, on the other hand, is passing up on the opportunity to examine and pre-select the best possible tip from an etching batch, especially if there is much variation in the results yielded by the etching process. (Another shortcoming of this operating short-cut when using the previously described etching procedure is that the protruding length of the tip can not be made much shorter than a millimetre, as the liquid meniscus formed under

the cell tends to expand downwards as the solution becomes more densely charged with platinum particles, thus threatening upon the merest contact to join through capillary action with the quartz or electrode material on which the tip is stuck.)

- When using epoxy, a thicker paste will help prevent the position of the tip from shifting and the adhesive from spreading across the surface while it cures – which spread would otherwise result in greater surface dampening on the resonator. Using standard mixing proportions for a given epoxy product, a thicker epoxy paste can be obtained towards the end of its allowed conservation time, as the resin will have thickened while preserved at low temperatures. On the other hand, a more liquid and permeating paste may be a better choice when dealing with electrodes of a material less amenable to surface adhesion, such as gold.

The density and applied quantity of adhesive are significant not only because of the dampening effect on the surface of the quartz, but because added mass unbalances the center of mass of a tuning fork [GmbH 05], resulting in a less sharp resonance (lower Q factor) or even separate resonances for each of the two tines in the case of a heavy imbalance. Balancing must therefore account for both the weight and position of the tip and adhesive, by adding a similar mass on the other tine. This can be done using only adhesive, or another tip of equal length; or if subsequently required, any substance suitable for fine-tuning, such as lacquer varnish.

2.3 Tip positioning

The tip is positioned along the axis of the oscillating motion, and in most cases its verticality relative to the samples needs to be ensured. This is the transverse mode, as opposed to the shear mode in which the tip is set perpendicular to the direction of motion in order to sense friction forces, and which is not considered here. In the case of tuning forks, three positions were thus used: (Fig. 2.7)

The fabrication of these probes does not easily lend itself to a reliable, systematic study of the ideal position of the tip along the geometry of the tuning fork, because the rest of the process itself is not repeatable enough to isolate this influence on the performance obtained with different probes. One would assume that positions that do not break the geometrical symmetry of the tuning fork, nor that of its oscillating motion, would be better adapted. As for the effect on the quality factor of the probe, no difference could be noticed between positions 1 and 3; the first was therefore preferred, as it is much more practical to achieve and ensures that the desired direction of the tip is respected.

However, on many tuning fork models, the electrodes either do not reach the tip of each quartz tine, or are divided near the end of their length (see Fig. 1.13). If the tip needs to be connected to ground, as is the case when the probe is to be used under an electron microscope, bridging the electrodes and the tip requires the application of additional conductive material on the quartz, further shifting the center of mass of the tuning fork and complicating balancing considerations. For this reason, SEM applications may rather opt to fall back on position 2.

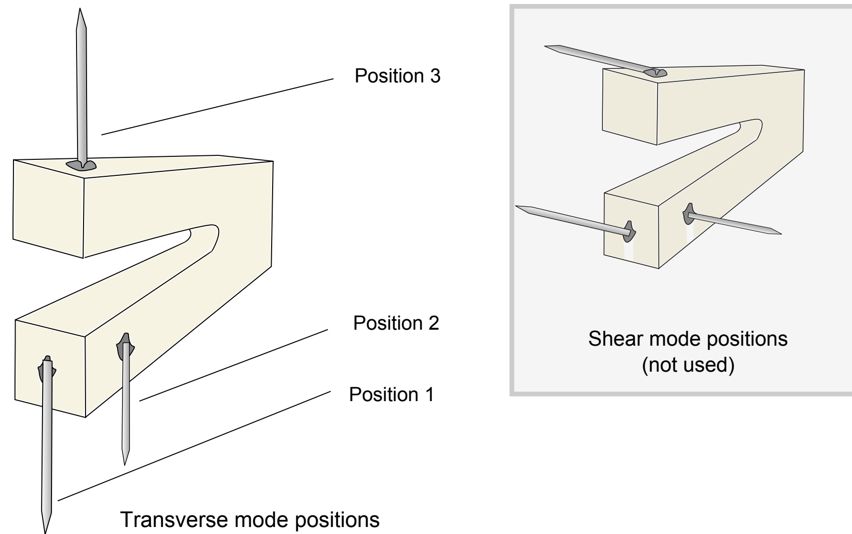

Figure 2.7 - *Possible positions of the tip for the transverse mode on a tuning fork, flexural oscillation based probe. (Right: shear of friction mode positions, not used in this chapter).*

2.4 Probe holder and fixation

The sensitivity of quartz crystals and tuning forks in particular makes the fixation of the component itself significant, as the probe will be sensitive to the slightest defect in stability. Since tuning fork components have already been designed and optimised by manufacturers, they are, aside from the removal of their canisters, kept in their original state: with the quartz electrodes soldered on two pins held by the ceramic base. For our purposes, these two pins are then soldered on a connector that can be snapped in or screwed on the final probe holder, which is the manipulating end-effector of the robotic system. Soldering, snapping or screwing on the pins guarantees the rigidity of the fixation.

From there the fixation must be not only rigid, but also "at rest": whichever way the pins are held, their natural shape may to some extent have to be adapted to a new configuration, for instance by bending the pins. Stress may thus be introduced to the fixation. The sensitivity of tuning forks is indeed such that the very small internal stress resulting from a small deformation of the pins can have an effect on the performance of the resonator. If the pins are soldered, it is therefore advisable to first bend the pins or their stubs into the desired positions, so that minimal stress, ideally none, is applied by the soldering of the second pin. One must note that internal stress may otherwise take up to a few hours or a few days to dissipate, with variable effects on the quality factor of the probe.

With the mechanical properties and fabrication process of quartz probes having been covered, it is now possible to inquire into which models of quartz resonators will advantageously lend themselves to making higher-frequency probes.

3 Towards higher frequencies

Tuning forks have been extensively used as sensors and AFM probes, but studies in the literature are largely limited to the most standard 32.768 kHz models. There is interest in operating such sensors at higher frequencies (see Chapter 1, 2.4) while still using currently available, off-the-shelf sensors rather than, in the absence of specialised manufacturing equipment, micromachined cantilevers or custom-made resonators. An examination of the other existing types of resonators or different ways of driving them is therefore warranted.

The appropriateness of a resonator towards use as a probe is determined by several factors:

- its size and total encumbrance, only in the case of constrained systems,
- its sensitivity, which can be evaluated as seen in Sect.1.3,
- the oscillation mode and direction of motion,
- the possibility of attaching a tip without hindering its performance.

The placement of the tip is dictated by the last two criteria. The resonator must offer a location which is consistently displaced along the desired direction during the oscillation, i.e. away from the fixed vibration nodes. On the other hand, if the tip is glued at a section of the quartz which is itself deformed during the oscillation, additional friction from the presence of the adhesive will dampen the resonance. It may be hypothesised that the electrodes themselves adapt to the deformation of the quartz surface they are attached to, since their stiffness has an influence on the performance of the resonators [Jing 07]; in which case applying the adhesive on the electrodes instead of the quartz does not necessarily prevent all losses due to friction. Overall, the tip should be positioned not at the center but further along the portion of the electrodes or quartz that is deformed during the oscillation – ideally at a free end of the resonator.

Here, we investigate several possibilities for the fabrication of higher-frequency probes based on off-the-shelf quartz resonators: overtone-driven tuning forks; tuning forks with higher eigenfrequencies; and three types of thickness shear resonators. All resonator characterisation experiments were conducted using a Zurich Instruments PLL and lock-in amplifier (ZI HF2LI), and a wideband high-frequency-compatible preamplifier designed by Jérome Polesel-Maris (CEA, Saclay) – the functioning of this oscillation setup is explained in greater detail in Chapter 3 (Sect. 1.1).

3.1 Tuning fork overtones

A resonator can be excited at a higher frequency than its fundamental mode, and aiming for its harmonic modes is one way of operating at a higher frequency. Overtone modes are besides used concurrently in bimodal AFM or dFM [Kawai 09] for increased contrast at the atomic scale,

albeit with commercial cantilevers or micro-cantilevers and not quartz resonators.

Tuning forks, as tools originally designed for musical tuning and later for minimal harmonic dissipation, have a very pure resonance. Little to no energy goes towards higher frequencies until around six times the eigenfrequency, which is close to the overtone mode of clamped beams – i.e. in the case of a 32 kHz tuning fork, the first overtone is around 190 kHz. With most commercial models, these being designed for fundamental excitation, the quality factor of the overtone is dramatically lower and therefore harder to exploit for force sensing purposes. In such cases, it is not as interesting a solution in a vacuum as the tuning fork at its fundamental frequency (Fig. 2.8), and even less so in ambient conditions. Table 2.1 here compares these values for several models of tuning forks. In one notable exception (Micro Crystal MS1V-T1K), the overtone mode is found to display a quality factor of comparable value to the fundamental mode, which also remains relatively high in air and with a tip.

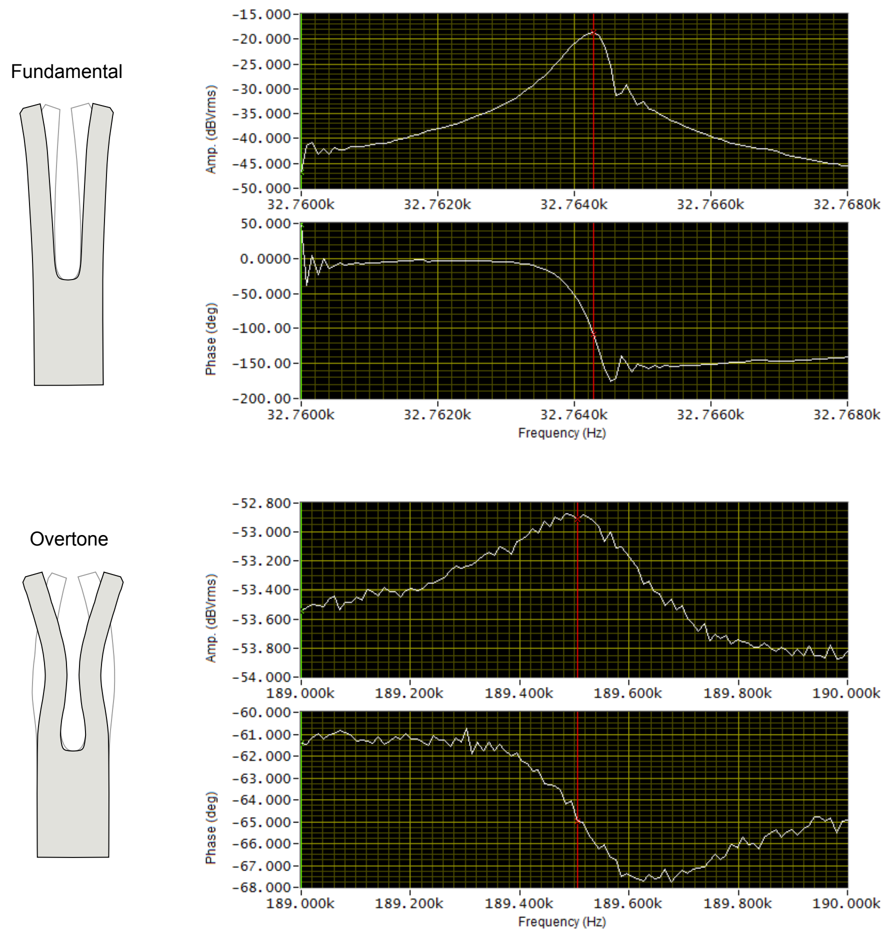

Figure 2.8 - *Amplitude-phase diagrams of the fundamental and overtone resonance of a usual 32.768 kHz tuning fork in its vacuum sealed container.*

Table 2.1 - *Quality factor (rounded) of the fundamental and overtone resonance measured for several commercial models of QTFs. *Measurement with tip in ambient air. All other measurements are taken in the original vacuum-sealed container of the QTF.*

TF Model	**Overtone freq (Hz)**	**Q (fundamental)**	**Q (overtone)**
CFS206	189505	50400	860
AB38T	189505	74500	760
XT32K	191263	80300	2100
MS1V-T1K	198120	64300	70700
MS1V-T1K with tip *	197685	4200	9200

3.2 Other tuning fork frequencies

Although the frequency attainable by commercial tuning forks is limited by their dimensions, optimisation of geometric parameters [Wei 14] and the corresponding mass-fabrication techniques, there exist commercial tuning fork models with eigenfrequencies in the range up to 200 kHz. Most tuning forks with frequencies above 65 kHz are designed with shorter prongs than the 32 kHz models of otherwise corresponding dimensions (Fig. 2.9); this results in a much higher stiffness (up to 4-6 times higher [Kim 14]).

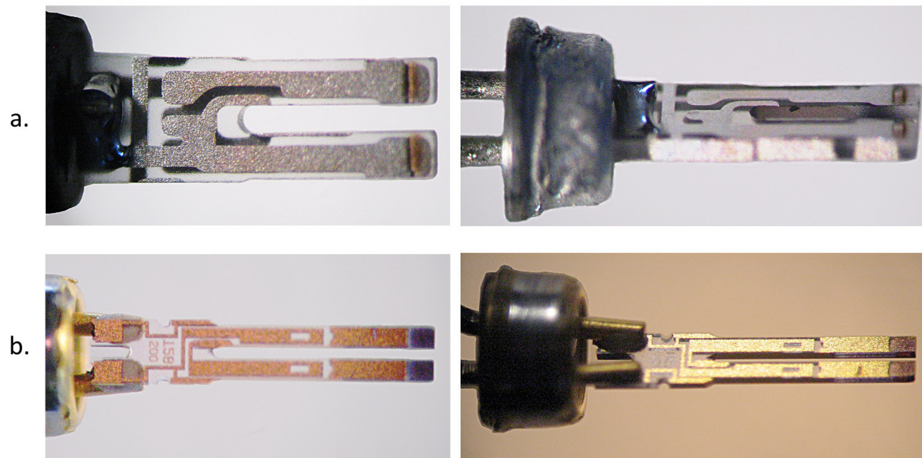

Figure 2.9 - *Prong length and thickness comparison between: a. – a 153 kHz tuning fork (ECS Inc XC978); and b. – a 32 kHz tuning fork of the same total length (Micro Crystal MS1V).*

While the fundamental frequency being higher is invariably accompanied by a larger bandwidth on existing components, the reduction in mass might in part make up for it regarding thermal noise. How appropriate these tuning fork models are for use as probes may depend more on the particulars of each model than on the design of shorter-pronged tuning forks itself: one 100 kHz tuning fork model (Citizen CFV206 100kHz) consistently displays a bandwidth of 0.7 Hz in a vacuum and 7 Hz in air, which is proportionally comparable to typical values for 32.768 kHz

models. However, the only available 153 kHz model (ECS Inc XC978), while it performs well in its vacuum-sealed container, is when in air subjected to a phase shift which normally results from a change in the internal stray capacitance, i.e. seems subjected to inharmonic perturbations. This behaviour could not be explained, but was reproduced on three individual components, as well as one for which the container was merely pierced instead of removed, confirming that the process of removing the canister is itself not responsible for the phenomenon. A similar effect can seemingly be found on some 40 kHz tuning forks (Citizen CFV206 40kHz).

3.3 Thickness shear quartz resonators

Little exists in the way of quartz components at frequencies between 200 kHz and AT-cut crystals, starting in the MHz range with thickness shear resonators (TSR, Fig. 2.10). Three main types of these high-frequency quartz resonators have been investigated: flat, "horizontally mounted" resonators held on both sides (Fig. 2.11), "disc-shaped" resonators (Fig. 2.14) and "contoured beams" (Fig. 2.17). While the latter may seem to be held in a way that is similar to a tuning fork, all three oscillate not flexurally but in the thickness shear mode. This is validated through simulations conducted with the COMSOL software: with the proper dimensions as input, finite-element frequential analyses yield fundamental frequencies corresponding to those of the real resonators, hence of the oscillation mode at chosen points.

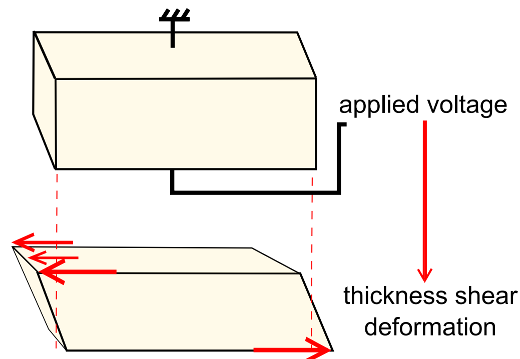

Figure 2.10 - *Thickness shear quartz deformation.*

3.3.1 Horizontally mounted resonators

These resonators exist with fundamental frequencies above the MHz range, and consistently offer a high quality factor, between 35k and 70k. Unlike tuning forks, for which the quality factor falls to a tenth of its initial value outside of its vacuum canister, their oscillation is barely affected when exposed to ambient conditions – i.e. Q = 50k *in vacuo* and Q = 40k in air. Their mass, consistently around 7.6 mg for several manufacturers, is barely higher than that of the

larger tuning forks. Because it is held at each end, the deformation during the oscillation of this type of resonator is essentially applied at the center of its length (Fig. 2.13).

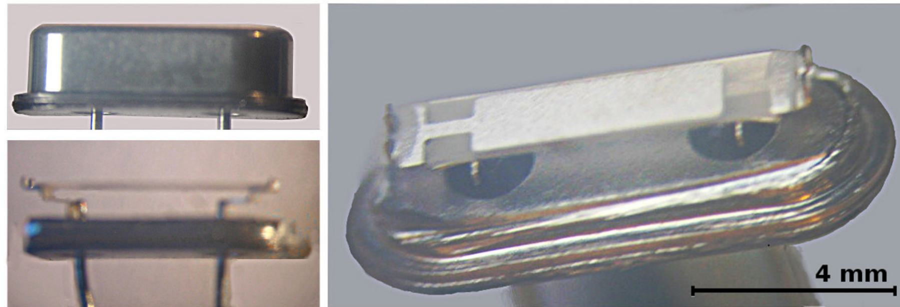

Figure 2.11 - *Horizontal thickness shear quartz resonator (QZ2768 7.68 MHz).*

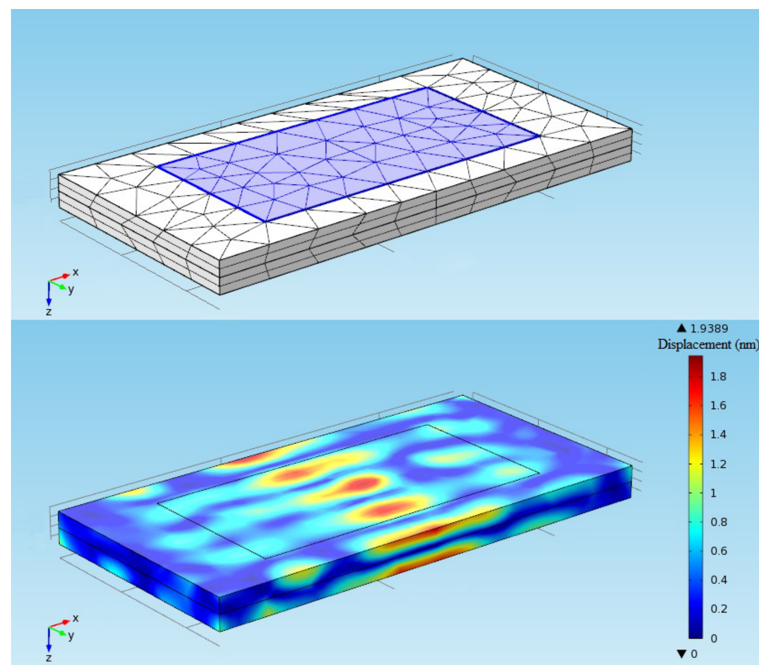

Figure 2.12 - *Horizontal thickness shear quartz: Finite Element Analysis 3D displacement plot in the COMSOL software.*

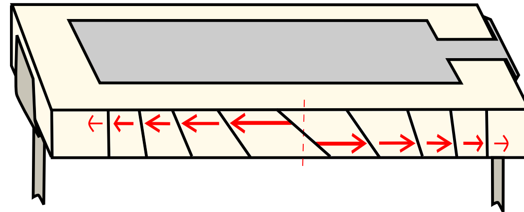

Figure 2.13 - *Horizontal thickness shear quartz: resonance mode and deformation.*

The thickness shear oscillating mode of these resonators dictates that a tip be both unusually long and positioned closer to the center of the resonator if it is to be operated in transverse oscillation (vertical to the sample surface). Attempts at adding such a long tip to these resonators were unsatisfactory, suppressing the resonance properties entirely (with epoxy) or hardly leaving any noticeable amplitude (with cyanoacrylate glue). No further investigations were conducted on these models, but their oscillation profile would better lend itself to shear-force (friction) sensing probes.

3.3.2 Disc resonators

Like the previous horizontal models, these MHz-range resonators (which also exist in rounded square shapes) offer high quality factors and are not discountenanced when exposed to air (e.g. Q = 40k *in vacuo* and Q = 35k in air). Less advantageous is their typical weight of around 60 mg and high stiffness. However, in this case the thickness shear resonance mode leaves a free end on which a tip could be located (Fig. 2.16) without affecting the resonance in the least – no major differences are observed in Q factor between the vacuum pressure of its canister, open air, and open air with a tip.

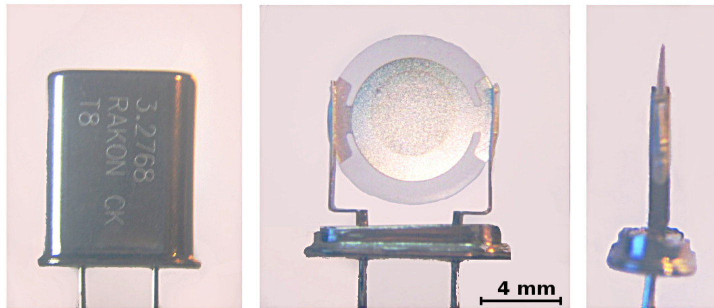

Figure 2.14 - *Disc-shaped thickness shear quartz resonator (Rakon XTAL 3.255 MHz).*

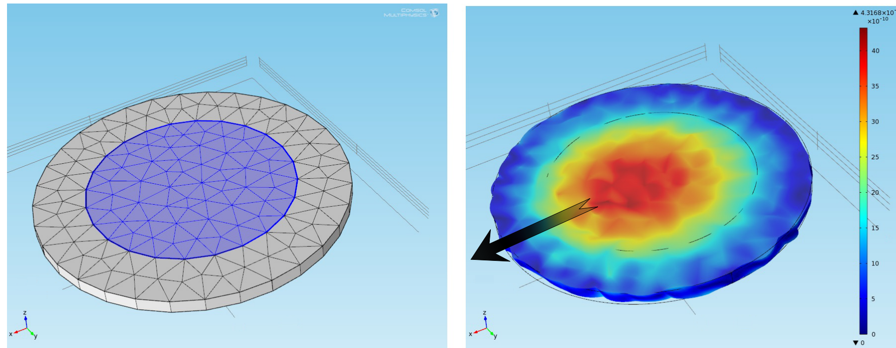

Figure 2.15 - *Disc thickness shear quartz: Finite Element Analysis 3D meshing grid (left), and 3D displacement plot (right) in the COMSOL software.*

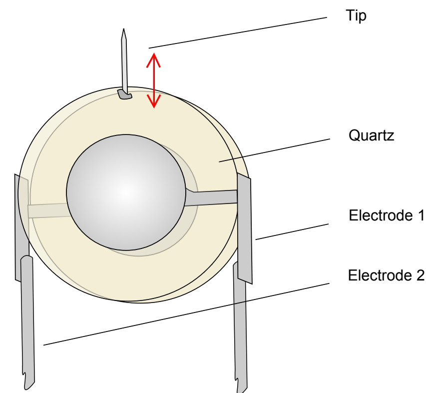

Figure 2.16 - *Electrodes and oscillation on a disc-shaped thickness shear mode MHz quartz resonator.*

Experiments using this probe suggest that their sensitivity is too low to be worth exploiting, especially compared with the next model. They may yet be exploitable for large-scale fast tapping, though with poor expectations for resolution.

3.3.3 Contoured beam resonators

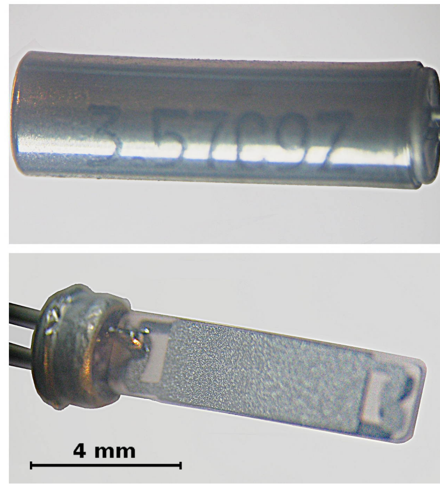

Figure 2.17 - *"Contoured beam" thickness shear quartz resonator (CSA31, 3.579 MHz).*

These MHz-range "contoured beam" resonators are mounted in a way reminiscent of tuning forks, but consist of a single monolithic crystal cut for thickness shear. Values are given for a Citizen CSA31 3.58MHz model (Fig. 2.17). They are stiffer and have twice the weight of a tuning fork of comparable dimensions (16.6 mg). They possess an excellent quality factor in a vacuum (Q = 90k), and while it diminishes when opened (Q = 45k in air) or assembled, the end result is still satisfactory (Q = 20k after glueing a tip).

These resonators are good candidates for the fabrication of quartz based probes. Their oscillation mode is obtained by thickness shear, and further analysis is conducted on their exact oscillation profile in Sect. 4, after the following comparison.

3.4 Comparison

A comparison of the commercially available resonators investigated above (Table 2.2) shows that likely candidates for use as higher frequency probes are tuning forks of a higher fundamental frequency up to 100 kHz, the 190 kHz overtone of certain select models, and "contoured beam"-type thickness shear resonators. Most tuning forks in overtone excitation lose too much of their fundamental quality factor, and it does not seem possible to achieve a functional transverse-mode probe with horizontally mounted resonators. Disc shaped resonators, while seemingly viable, have a poor sensitivity – considering their mass and -3dB bandwidth and using the thermal noise sensitivity evaluation (Sect. 1.3), their smallest attainable sensitivity would be at least

Table 2.2 - *Qualitative comparison of various resonators using an approximate thermal noise sensitivity ratio relative to the average 32 kHz standard tuning fork.*

	-3dB bandwidth, vacuum (Hz)	**-3dB bandwidth, air (Hz)**	**Mass (mg)**	**Thermal noise sensitivity w/r/t standard tuning fork**
32 kHz Tuning fork	0.5	3	2 - 6.8	1
191 kHz TF Overtone	300	?	2 - 6.8	N/A
100 kHz Tuning fork	0.8	7	3 - 5.2	0.7
153 kHz Tuning fork	1.5	?	3 - 5.2	N/A
7.68 MHz Horizontal TSR	60	60	7.6	N/A
3.27 MHz Disc TSR	85	90	61.8	1/30
3.58 MHz Contoured TSR	35	66	16.6	1/5 - 1/7

17 to 30 times worse than that of the bulkiest tuning forks. Contoured beam resonators are in comparison evaluated as only 5 to 7 times less sensitive, and are hereon further analysed towards their adaptation as probes in the MHz range.

4 MHz-range contoured beam quartz analysis

The "contoured beam" quartz models are commercialised as resonators made from AT-cut crystals. However, as for other quartz components, their specifications are tailored towards electronic applications, and manufacturers do not specify in which direction they oscillate at their resonance. Being held at only one end, their geometry can conceivably point to total resulting oscillation in the flexural as well as shear modes. In order to determine how to position the tip for transverse mode oscillation (as opposed to shear mode oscillation for friction sensing), the oscillation mode of the previously selected 3.58 MHz resonator is therefore studied here.

4.1 Hypotheses

Because of the dimensions of the resonator, an in-plane flexural mode (comparable to a phase oscillation mode of a tuning fork, as illustrated in Fig. 2.18), while possible, would have to be found at frequencies much inferior to that of their given eigenfrequency – in the case studied here these frequencies are found only under 1 MHz. Given that the crystal is known to be AT-cut, the deformation of the quartz is expected to be thickness shear, and the resulting main mode of oscillation is to be found, depending on the angle of the cut with regard to the orientation of the crystal block, as either an out-of-plane flexural mode or a lengthwise shear mode (similar to that of the disc resonator in Section 3.3.2).

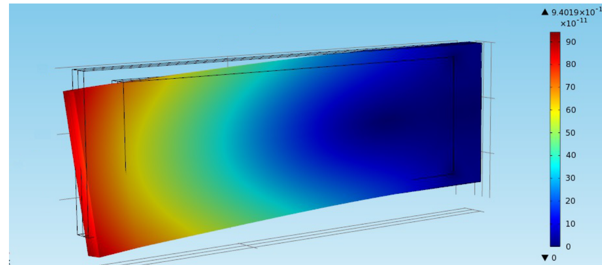

Figure 2.18 - *Contoured beam quartz: Finite Element Analysis 3D displacement plot of the in-plane flexural oscillation mode with a simplified model in the COMSOL software. This oscillation mode is never obtained at the operational frequencies of this model, above 3 MHz.*

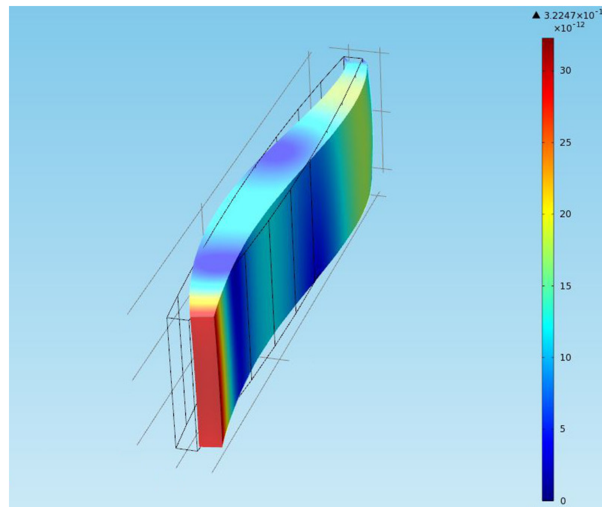

Figure 2.19 - *Contoured beam quartz: illustration by Finite Element Analysis in the COMSOL software of an out-of-plane flexural mode of oscillation. This oscillation mode may manifest as a spurious mode at the operational frequencies of these models, which their contoured geometry aims to prevent.*

A FEM (Finite Element Method) analysis was conducted with COMSOL by replicating as best possible the dimensions of a real 3.58 MHz crystal model (around 8.5 x 2.5 x 0.5 mm). The contoured shape of the rectangular crystal was roughly approximated – the purpose of this contouring in the fabrication process is to lessen the influence of spurious modes [Wang 13], such as out-of-plane flexural modes (Fig. 2.19), by energy trapping. Differences in the orientation of motion resulting from the deformations displayed by FEM analysis between a non-contoured and a contoured profile indeed show a great diminution in such secondary modes.

Quadrangular meshing was used in the swept mode (Fig. 2.20) between the two lateral faces of the model, with a maximum element size of 0.1 mm, maxium element growth rate of 1.5, and curvature resolution at 0.6. The quartz material was defined according to the 1987 IEEE

standard for AT-cut crystal orientation. Geometry nodes were fixed at one end, corresponding to where the electrode pins are welded, the rest of the material being free. Arbitrary voltage was applied across the material in a frequency domain simulation first between 0 and 10 MHz with steps of 10 kHz, then between 2 and 5 MHz with steps of 1 kHz.

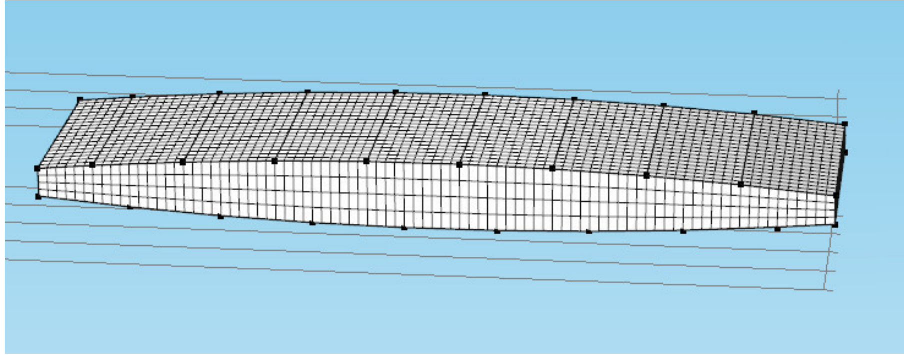

Figure 2.20 - *Single beam quartz: Contoured geometry and display of the Finite Element meshing.*

4.2 Results

The piezoelectric device solver analysis indicates a resonance frequency at 3.8 MHz (Fig. 2.21) which is so dominant as to correspond without doubt to the real resonator's eigenfrequency of 3.58 MHz. The 5% difference is to be explained by a combination of: slight inaccuracy in the dimensions measured on the real quartz crystal; the approximated angle of the contoured profile in the model; and possible inaccuracy in the analysis. We therefore conclude that the oscillation mode of these resonators at their operating frequency is the lengthwise shear mode (Fig. 2.23). The simulation yields oscillation amplitudes of 5 to 9 Å per volt of driving excitation.

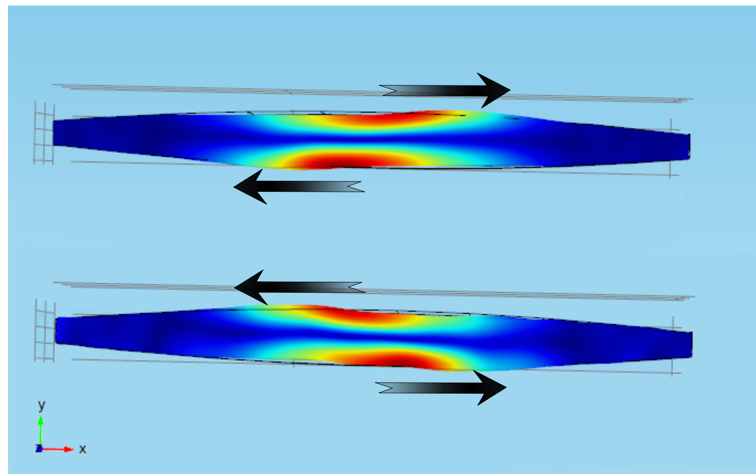

Figure 2.23 - *Contoured beam quartz: 3D displacement illustration of the thickness shear oscillation mode. This mode is the one displayed by FEM analysis at the eigenfrequency of the component.*

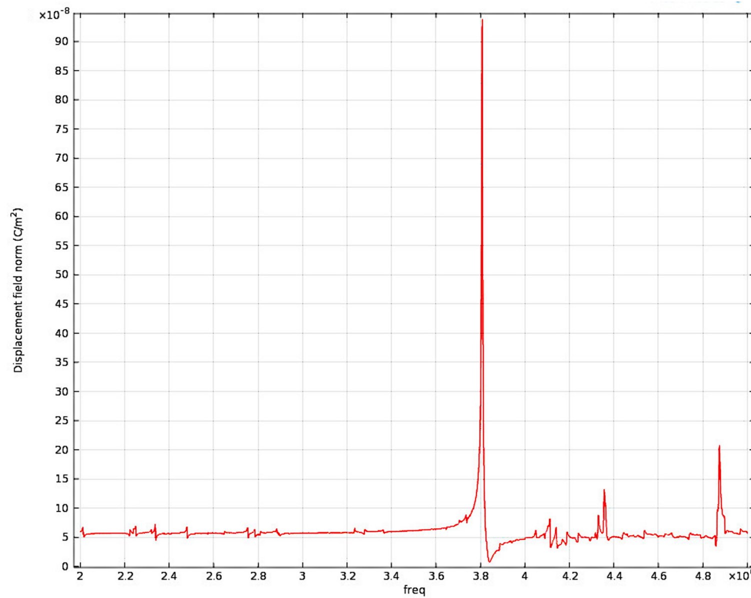

Figure 2.21 - *Contoured beam quartz: Electric displacement field (C/m^2) graph by FEM analysis of the quartz under a 1V driving excitation between 2 and 5 MHz. The resonance for the model is found to be clearly situated at 3.8 MHz.*

This analysis confirms the experimental observation that the nearer an additional charge (glue and tip) is added to the middle of the resonator, the more influence it exerts on the resonant frequency and quality factor of the probe. An immediate interpretation is that the presence of glue creates all the more additional friction and dissipation when its location is one of greater deformation, which is to say of greater oscillation amplitude and greater absolute speed. The placement of the tip is thus the result of two compromises: the first between the transmission of the oscillation amplitude from the resonator to the tip and the mitigation of added dissipation to preserve the quality factor of the probe; the second between an angle closest to the direction in which the crystal oscillates, while maintaining a reasonable tip length and distance between the tip and the crystal.

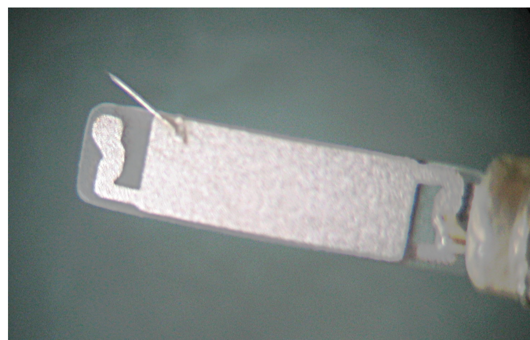

Figure 2.24 - *3.58 MHz probe with tip, here glued closest to the end of the resonator.*

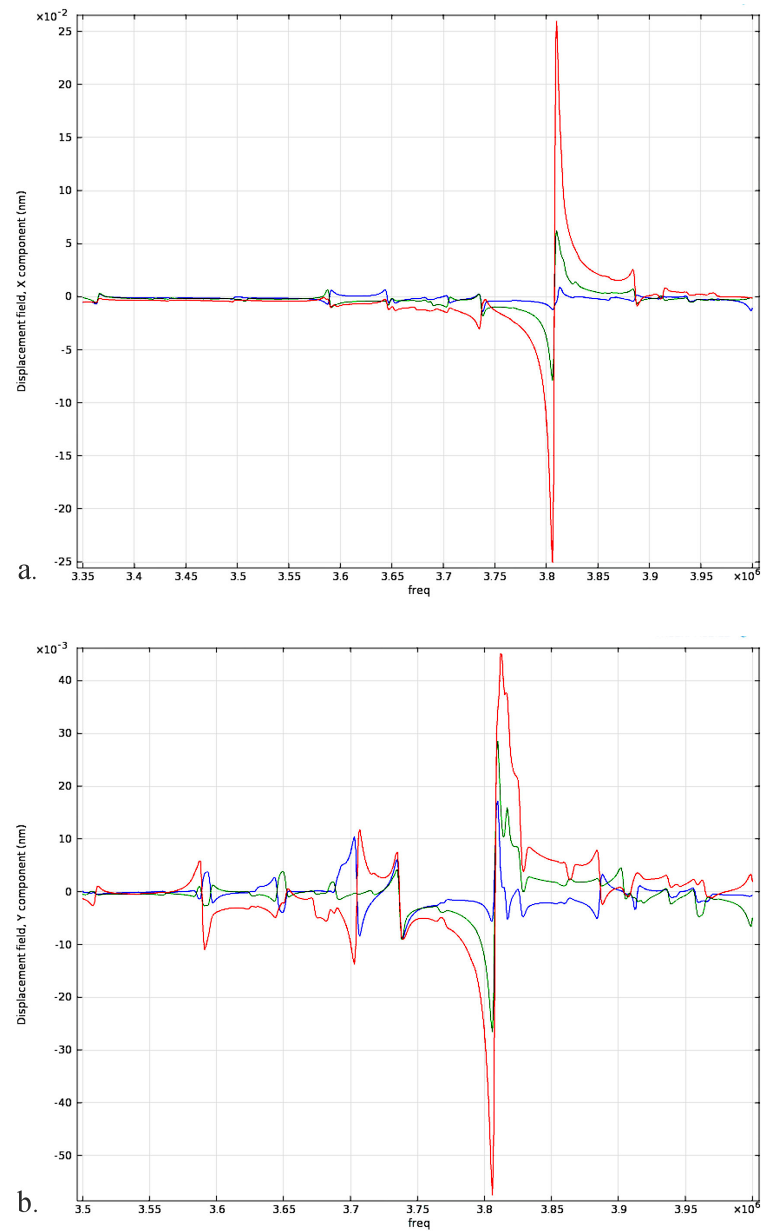

Figure 2.22 - *Contoured beam quartz: Displacement graph by FEM analysis on three points (A,B,C) of the quartz under a 1V driving excitation at its resonance frequency; – a.: Along the X axis, the main direction of oscillation. The oscillation amplitude for the point closest to the center is of 5 Å; – b.: Along the Y axis. Comparatively, the oscillation amplitude for the point closest to the center along this direction is of 1 Å.*

5 Conclusion

The sensing parameters, fabrication and mechanical characterisation of probes based on quartz tuning forks has been covered. Based on this, an enquiry has been made into other quartz resonators which can likewise be used for the fabrication of higher-frequency probes.

In the kHz range still, tuning forks driven at the first overtone and other models of tuning forks have first been examined and judged based on their quality factors in air and with a mounted tip. While the 190 kHz overtones of commercial tuning forks from most manufacturers were not found to be exploitable, one exception was pinpointed and along with one 100 kHz tuning fork from shorter-pronged models has been selected for potential use.

At frequencies one order of magnitude higher have thickness shear quartz resonators been investigated. Experimental results have shown that MHz-range quartz resonators are less affected by the application of glue than tuning forks, which is in line with the demonstrated result that surface loss is only the dominant effect on quality factor for low frequency resonators. [Najar 15] Criteria for high-frequency quartz have instead here pertained to their sensitivity with regard to greater dimensions and higher stiffness, and the applicability of a tip to their oscillation mode. Amongst the three types of high-frequency thickness shear resonators examined in this chapter, contoured beam resonators have been selected for use as probes, and their oscillation mode has been analysed by FEM with the aim of understanding their behaviour and determining viable tip positions (Fig. 2.24). The next chapter will be dedicated to the testing and application to imaging in ambient conditions of the probes selected in this chapter.

Chapter 3

Ambient imaging with quartz probes

Surface topography is a direct application of the self-sensing quartz probes studied and selected in the previous chapter: AFM imaging will here provide a way to validate their design, and characterise their performance with regard to that of the more common 32 kHz tuning fork probes. This chapter thus explores the imaging capabilities and speeds of these probes in both attractive and repulsive modes, on hard micrometer-scale calibration networks or soft wax surfaces, with profile heights in both cases under a micrometre. The difficulty lies in drawing conclusions from results in which scanning speed and image resolution are interconnected, as well as dependent on such other factors as: the hand-made fabrication of the probes; environmental conditions and humidity in ambient air; the control scheme of the actuators; or the optimal operation range of the oscillation control hardware. In order to extract information from experiments in which not all parameters can be fully tracked, this study relies on the qualitative comparison between results taken on the same set-up and samples. While the comparison is here specifically made in ambient imaging (both because of the available equipment and as a step towards biological conditions), the improved scanning speed which is desired from higher-frequency components would be expected to likewise affect imaging or micro-robotic experiments in a vacuum.

The first section describes the experimental apparatus operating the quartz probes and its control parameters, from the actuators to the quartz oscillation electronics. The second section deals with preliminary considerations: the general experimental protocol which is observed before conducting a scan; an assessment of the position performance on the actuators of the system using its end probe; and the characteristics through which the quality of an image is to be evaluated. The last sections display the imaging results obtained with several probes, for the purpose of comparing their respective performances and attainable speeds.

1 Experimental setup

This section describes the oscillation control hardware and software driving the quartz probe and their operation; the actuators used to vertically approach and horizontally scan samples; and the control parameters for both oscillation and actuation, which will be relevant to understanding and comparing the performance of the quartz probes.

1.1 Quartz control, electronics and software

The setup used throughout this chapter includes transimpedance electronics of a model similar to that used to measure resonance frequencies and quality factors in the previous chapter: a transimpedance pre-amplifier designed by Jérôme Polesel-Maris for use in the high-frequency range up to 10 MHz, set as intermediary between the quartz probe and a ZI (Zurich Instruments Ltd., HF2LI) Lock-in Amplifier and Phase-Locked Loop (PLL).

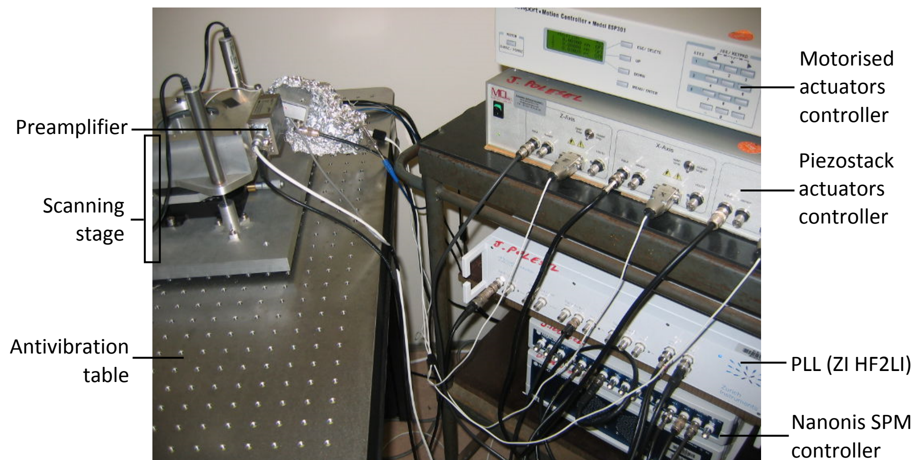

Figure 3.1 - *Experimental setup.*

The ZI PLL system locks in on a user-specified phase value while exciting the quartz at a constant drive voltage, and is configured to transmit frequency shift data (dF) as well as oscillation amplitude (A) and phase (P) through three analog channels into a Nanonis SPM Controller (SPECS Zurich GmbH, RC4 Real-time Controller and SC4 Signal Conditioning). This signal is oversampled by a factor of 2 to 10. The Nanonis SPM package does not control the oscillation, but it manages the coarse and fine actuators:

- It handles the initial tip-sample approach sequence as an automated cycle composed of two steps, with frequency shift feedback from the quartz probe being used to stop near the surface at a given dF set-point. First, the fine Z-axis actuator sweeps through its whole range (51 µm). Once it reaches the end of its course, the fine actuator is raised

back to its top position and the large-range coarse actuator lowers the system by a preset amount (roughly 40 µm). The fine actuator then repeats the sweep, and so on.

- While imaging, it controls the Z-axis (height) of the probe, with a PI controller applied on the frequency shift feedback value. It also coordinates standard raster scanning operations using the X and Y axes, sweeping the chosen area at a given speed and with a set number of lines: each line is scanned back and forth once before the actuators switch to the next line.
- The Z-axis data gathered while scanning a surface is rendered into a 2D overhead picture, colour-coded for elevation (as later shown in Fig. 3.8). The software includes such standard operations as scale shifting and linear compensation post-processing. In addition, the hardware was also used to provide a stabilised power supply to the pre-amplifier, which is critical to the mitigation of electronic noise.

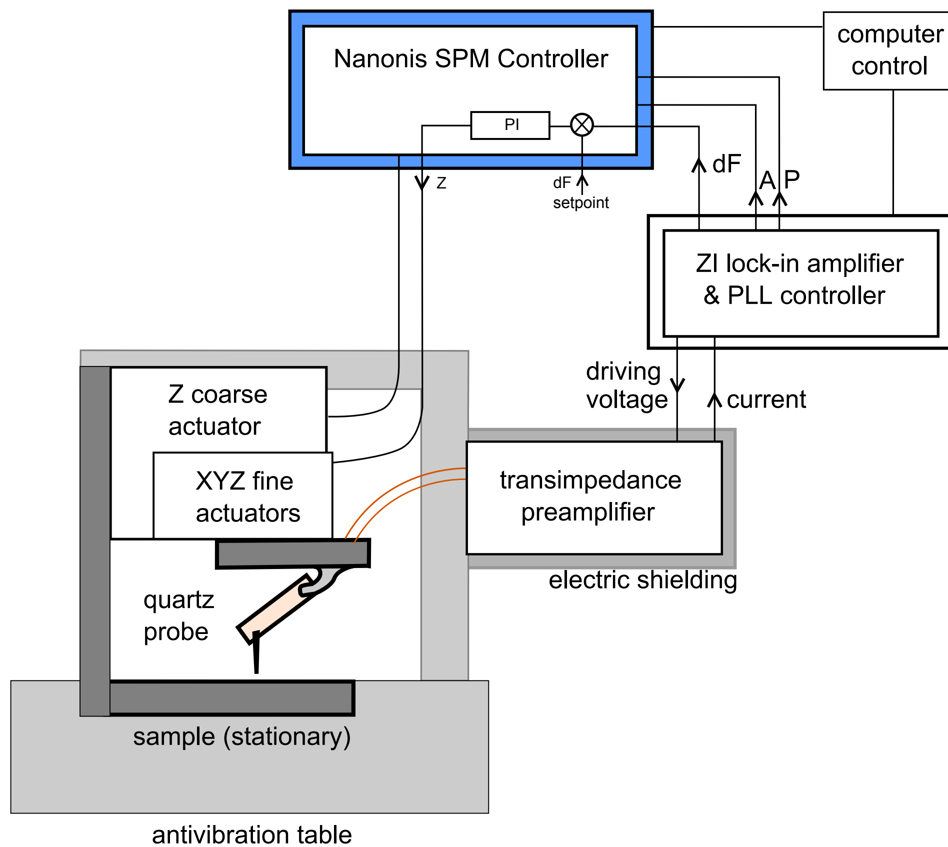

Figure 3.2 - *Overall structure of the experimental setup.*

When it comes to oscillation control modes used for imaging, the ZI electronics package can be operated in two FM-AFM modes: [Zurich Instruments 12]

- Constant phase and constant drive amplitude (FM-AFM): in which the PLL feedback loop

locks the value of the phase relation between driving frequency and cantilever excitation. The frequency shift dF between the oscillating frequency of the probe and the frequency set-point conveys properties related to both elastic and inelastic tip-sample interaction (resp. conservative and dissipative forces, Sect. 2.2.3),

- Constant phase and constant oscillation amplitude (FM-AFM and AGC): in which the automatic gain control keeps the measured amplitude of the probe constant. Damping or dissipative effects are largely removed from the frequency information, so that the frequency shift dF mainly conveys properties related to elastic (conservative) tip-sample interaction.

In the imaging experiments conducted in this chapter, the first operating mode for the PLL setup (FM-AFM) was chosen, as the image is constituted from a dF-controlled Z profile, and including the dissipative effects leads to increased dF contrast. The second mode of operation may however result in more sensitive control, especially for high-resolution imaging.

1.2 Actuators

The choice of actuators is not a marginal factor, in that their control and performance will be reflected in the results obtained through their displacement of the probe – be it range, resolution, time response, behaviour when the direction of motion is reversed (as is the case with raster scanning)... Commercial actuators are here used with the control scheme provided by the manufacturers.

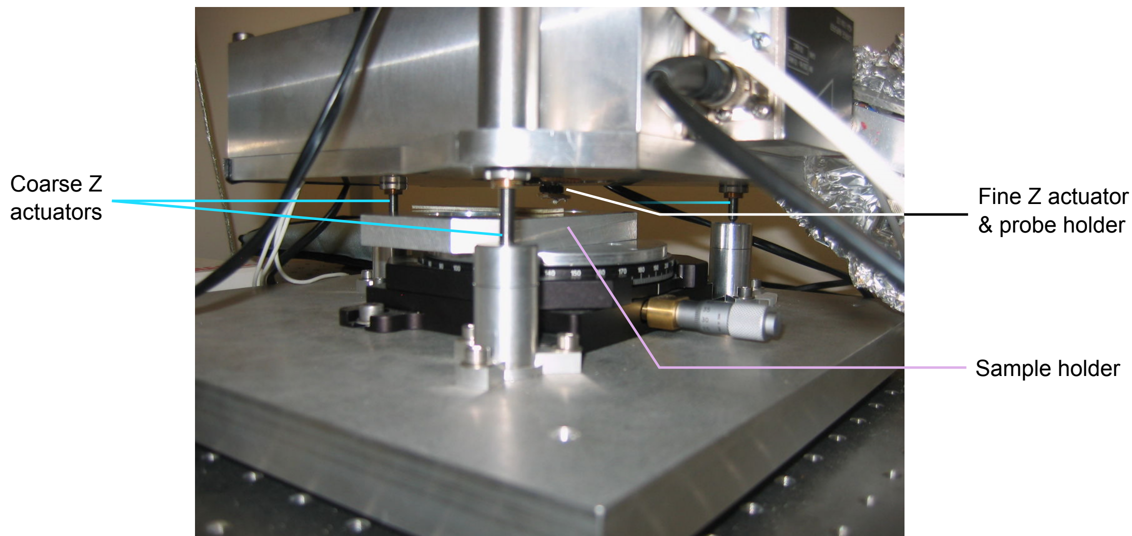

Figure 3.3 - *Actuators setup and probe holder.*

The actuators used in this setup are:

- Fine actuators: Nano-PQD375HS (Mad City Labs Inc.), closed loop nano-positioning system with Nano-Drive® controller ND85-ARIO-OC4 and PicoQ® sensors. The system provides large load capacities with a large center aperture suitable for use with a microscope (Fig. 3.4). Its characteristics are as follows (Table 3.1):

Table 3.1 - *Characteristics of the nano-positioning system. Step response is defined as the time taken to traverse 10-90% of the commanded input value.*

Axis	**X**	**Y**	**Z**
Range of motion	76.865 µm	76.525 µm	51.190 µm
Resolution	0.15 nm	0.15 nm	0.1 nm
Resonant frequencies	1080 Hz	840 Hz	265 Hz
Step response	2 ms	4 ms	6 ms

- Coarse actuators: 3x Newport TRA25PPD, motorised actuators with a 12 mm travel range.

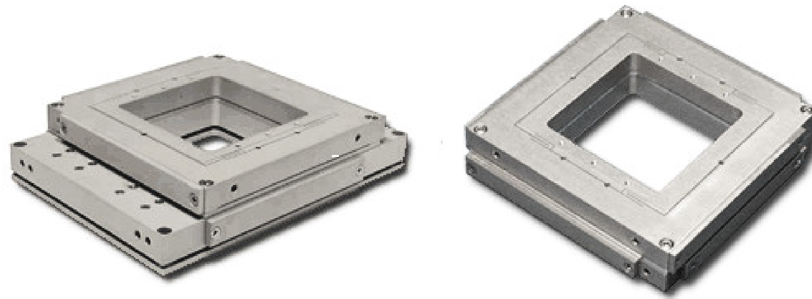

Figure 3.4 - *X/Y/Z nano-positioning actuator Nano-PQD375HS (Mad City Labs Inc.).*

The frequency of the Z/vertical axis is expected to be one of the limiting factors for scanning speed. The control scheme is the one provided with the actuators, and precise informations on accuracy are not given. Further on, the accuracy of the micron-range actuation within the system will be roughly evaluated using the probe and according to a basic procedure (see paragraph 2.5.1).

1.3 Control parameters

The main parameters relevant to imaging performance which can be set throughout the setup are of two categories: resonator excitation and oscillation control parameters (ZI PLL), and actuator control parameters (Nanonis). The values which will be used for the upcoming experimental comparison are given here; where no value is given, it should be understood that the selected parameters will later be whichever yield the best performance.

- ZI: Driving amplitude (V): the sinusoidal tension which goes through the transimpedance preamplifier before being applied to the quartz resonator. It is directly proportional to the oscillation amplitude of the probe. While low oscillation amplitudes are desirable in FM-AFM, signal-to-noise ratio and lock-in stability are negatively affected if the driving amplitude isn't high enough with regard to the chosen bandwidth. Values used range between 30 mV and 300 mV, depending on resonator types. The chosen value is typically chosen safely above the lowest value for which the PLL indicates a successful lock-in at a given bandwidth.
- ZI: PLL bandwidth (Hz): the higher the bandwidth, the faster the output of the control loop. Too high a bandwidth can lead to unstable control. When not otherwise specified, the value used here is 1.6 kHz.
- ZI: PLL PI settings, gain (Hz/deg) and time constant (s), applying on the output frequency.
- ZI: PLL Phase set point (deg): this is the phase value on which the PLL locks in. The value aimed for is that which corresponds to the height of the resonance curve of the quartz probe: once the parasitic capacity (from the quartz resonator) and cable length capacity are balanced, and in the absence of delay, the resonance phase is $-\frac{\pi}{2}$, i.e. -90°. Note the importance of setting (or rather resetting) the PLL phase reference once the probe has been brought near the surface: its value may change due to long-range electromagnetic forces, and very repeatable phase and frequency shift variations are indeed observable even up to several millimetres above the surface.
- ZI: PLL Center frequency (Hz) and range (Hz): the configured frequency value to which the phase-locked frequency value is compared. The "frequency shift" or "differential frequency" Δf refers to this comparison. The range defines the acceptable frequency shifting range beyond which the PLL is to cease operating. The center frequency is chosen as a value as close as possible to the natural or "free" resonant frequency near the surface, which is to say: the frequency at which the probe resonates while it is at close distance but not in contact with the surface, as well as free from any strong attractive forces (e.g. 1 µm away from the surface).
- Nanonis: Z-Controller frequency shift set point ΔF: this is the frequency shift value of Δf for which the controller aims. This value is chosen depending on the sensitivity of the probe and noise levels of Δf in the given environment. In the attractive mode, ΔF is negative and its absolute value must be small enough to always be attainable and for the controller never to drive the probe into contact with the surface; in the repulsive mode, it is positive and must be the smallest possible value above signal noise, since greater Δf values correspond to progressively stronger forces and friction on the tip. Values used will range between 50 and 300 millihertz.
- Nanonis: Z-Controller PI settings, proportional gain (m/Hz) and time constant (s): for the dynamic control of the fine Z-axis (i.e. vertical) actuator when sweeping over surface topology during imaging. The Z gain is proportional to the frequency shift Δf.
- Nanonis: Linear speed (m/s): the speed at which the X and Y-axis (ie horizontal) fine actuators scan lines during imaging.

The PLL parameters are chosen so that the oscillation control will be as fast as possible while retaining stability in the chosen operation range. This range must not only comprise the desired set-point, which is always less than a few Hertz, but also allow any peak values which may be reached within the controlled oscillation.
The choice of actuator parameters here consists in a compromise between a linear X-Y scanning speed which takes the fullest advantage of the oscillation control speed and, on the other hand, Z-axis PI settings fast enough to drive the probe to the full range of depth of the given sample at that linear scanning speed, without damaging the tip of the probe by collisions or friction.

2 Experimental protocol and testing

Preliminary considerations to the upcoming imaging experiments are here covered. First comes the choice of operating mode and how it is informed by an approach cycle between the probe and sample, then are described the two main types of samples used for imaging in the chapter. The next two parts expound on how the quality of an image will be evaluated towards a comparison of the probes, and what phenomena can be expected to manifest as artefacts during a scan. The section closes with a basic self-characterisation of the system, from the performance of the actuators to how they relate to *in situ* tip-sample interaction during imaging.

2.1 Attractive and repulsive modes

At the operating range and resolution of the probe and actuations, attractive interaction is typically of much smaller strength than repulsive interaction. Identifying sensitivity to attractive forces requires an approach procedure displaying distinct pull-in and contact phases (see Chapter 1, Sect. 2.1.1 - Fig. 1.8). In FM-AFM, attractive forces are denoted by a negative shift in frequency, though this in itself is not proof that attractive or "non-contact" forces are being sensed. "Non-contact" is besides a controversial term (see "near-contact"), and it can be argued that sensing attractive forces is only an indication that attractive forces are overall dominant on the tip, and does not preclude locally repulsive contact between the endmost apex and surface.

In regular environmental conditions, meaning ambient air and atmospheric pressure, greater ambient humidity facilitates the formation of a meniscus between the probe tip and the surface. As a result, it can often become impossible in these conditions to stay in a true "non-" or "near-contact" imaging mode limited to attractive forces. The necessity of combining small oscillation amplitudes and low noise for sensitivity to shorter-range forces in order to achieve attractive mode imaging is thus more demanding in ambient conditions.

2.2 Samples

Two main types of samples are used in this chapter: calibration gratings and paraffin wax surfaces.

- **Calibration gratings**: (Fig. 3.5) NT-MDT calibration gratings with a 3 µm (± 0.05 µm) period, here TGZ02 (110 nm step height) or TGZ03 (520 nm step height). These samples are formed on SiO_2, and meant for Z-axis calibration (respectively ± 2 nm and ± 3 nm on a constant base height of ± 10% the specified value). Their specific function as AFM samples is to confirm that the scaling calibration of the system is valid.

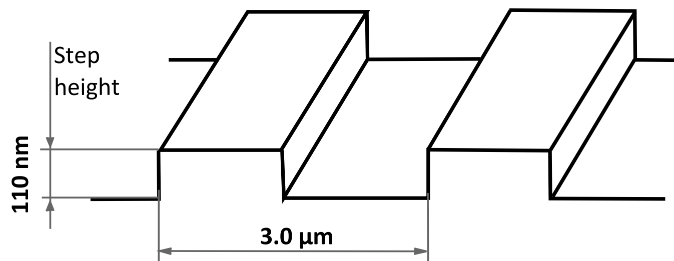

Figure 3.5 - *Calibration sample: NT-MDT TGZ series.*

- **Paraffin wax**: hexatriacontane ($C_{36}H_{74}$) beads, melted on a nondescript silicon surface. A surface thus constituted provides a significant advantage over calibration samples in prolonged AFM testing, since it is soft and will be much less taxing to the tip of a probe. This reduces the inevitable wear damage and is more permissive of fast Z approach phases, as well as of collisions during raster scanning, which may happen when test parameters are still in the process of being tweaked.

2.3 Imaging criteria

The purpose of scanning calibration samples is to ascertain that the obtained images and surface profiles match expectations, thanks to known distances and heights. When an AFM system is used for actual imaging purposes, however, different questions apply as to whether the results properly reflect an unknown sample. Whether images are taken on calibration samples or undefined surfaces, they will here be evaluated, be it qualitatively, through the following criteria:

- **Accuracy and sharpness** of edges: while there is no absolute measure of edge accuracy, edges or height profiles must match and follow between the successive lines of a raster scanned image. This is made easier on calibration samples, which guarantee clear-cut

edges along at least one dimension. Sharpness (as opposed to blurriness) is greatly dependent on the shape and size of the tip relative to the geometry of the sample, as well as the reactivity of the system and scanning speed.

- **Forward and backward** images: on a similar note, comparing the height profile obtained while scanning in one direction to that obtained while scanning the same line in the opposite direction (before switching to the next line) may reveal differences either related to errors, or resulting from the shape of the tip or nature of the sample. While some difference may thus be unavoidable, adequation between the profiles and images constituted by backward- and forward-directional scans (Fig. 3.6) is well indicative of local repeatability, and serves to discern whether certain details are descriptive of the surface or the result of flaws in the system (over- or under-reactive actuator control, recurring noise patterns, or spurious errors of any kind).

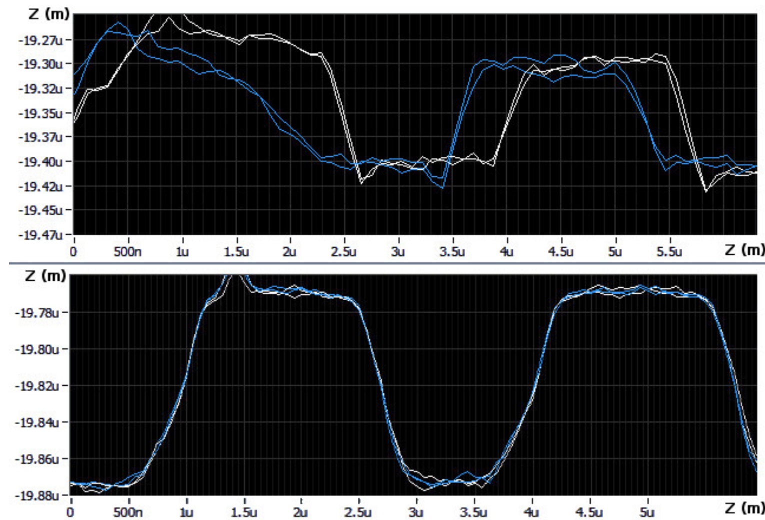

Figure 3.6 - *Difference between the backward (blue) and forward (white) scanned profiles being discordant (top) or concordant (bottom).*

- **Stability** and imaging mode: a stable image requires that the frequency shift control loop not switch between attractive and repulsive modes. In the case of attractive mode control, the probe tip must remain in the attractive zone during the whole scan. Making sure that the measurement is indeed being taken in the attractive mode in the first place requires the prior acquisition of an approach-retract frequency shift curve, which displays both attractive (pull-in) and repulsive (after contact) zones.
- **Rotation**: the image obtained over the same zone after rotating the raster scanning orientation at an angle must provide correspondingly rotated results. This is a most certifiable way of confirming that the details found in each image indeed correspond to elements located on the sample surface.
- **Speed** comparison: while not strictly a measure of image quality in itself, scanning speed is to be increased along with the parameters for both PLL and Z control while making sure the above criteria are respected. A criterion which may nevertheless be significant as to the accuracy of the image itself is that while increasing speed may introduce various

errors, the quality of the image must in no way deteriorate when *decreasing* speed. Any such deterioration would be related to issues with stability or, especially in the case of patterned samples such as some molecular structures, would indicate that the observed patterns are merely the result of noise, or of the combined effects of the actuator and quartz control loops.

2.4 Artefacts and causes

Of the many types of artefacts potentially found in AFM images, some of which are illustrated and examined in [Yong 12], those encountered here include the following:

- **Parachuting** occurs when tip-sample interaction is lost and the vertical controller is slow in adjusting back towards the surface while the linear horizontal controllers keep scanning. This can be the case after any sharp shifts in height, including after upscale overshoot. Together with the admissible vertical controller gain, this is an inherently limiting factor for linear scanning speed.
- **Blurred edges** can be the result of vibrations, insufficient probe sensitivity and noise, sluggish control or of tip size (tip-sample convolution), while **horizontal scars** or choppy edges may result from any reference shift (between the coordinate frame at the point of interaction i.e. the apex of the tip, and the coordinate frame of the actuators) taking place while switching from one line to the next.
- **Adhesion** between the tip and sample as well as menisci due to humidity generate pervasive distortions of various kinds, some of which can be the above mentioned incongruities between lines.
- **Vertical creep** gives the impression of a sloped surface, and if the scanning speed is slow enough can create wide distortions between the forward and backward directions due to reversed slopes. Horizontal creep or X-Y coupling stretch images in one direction or towards a corner.
- **Horizontal slant** or tilt between the actuators and sample (i.e. equivalent to an actually sloped surface), especially when it induces an angle between the tip and sample, effectively implies a basic coupling of vertical Z control to horizontal X-Y motion. This is still the case to some extent when the angle is measured beforehand and compensated for, which is yet critical (see Fig. 3.7).
- **Hysteresis** in the actuators causes easily identifiable distortions. Hysteresis in the dynamics of the probe, however, affects the whole regulation, and is evidence of either inelastic energy loss (damping) or adhesive effects which can only be identified on an approach-retract curve.
- **Thermal drift** slowly increases or decreases the resonance phase and frequency of the quartz probe, and if not addressed causes the frequency shift set point to slowly vary during the scan, which affects tip-sample interaction throughout.
- Finally, **electrical noise** from any source directly translates into image noise.

Although it makes it harder to evaluate image accuracy, apparent drift will not be discussed further when evaluating the probes: its cause lies either in the behaviour of the actuators, or in the probe's eigenfrequency magnitude. The imbalance in frequency-absolute sensitivity to temperature is due to thermal drift specifications being, in the electronics industry, controlled in percentile proportion to the frequency eigenvalue of a quartz – whereas in their use in AFM, the acceptable frequency shift which is controlled during imaging operations is regardless of eigenfrequency of a similar order of magnitude (always less than a few Hz): probes based on MHz-range commercial quartz will thus inevitably suffer from much greater frequency drift than kHz-range components.

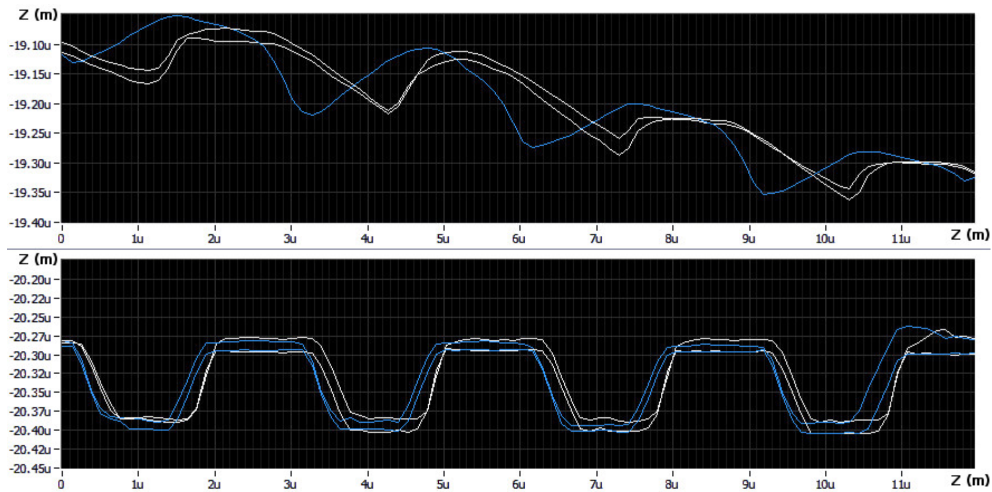

Figure 3.7 - *Initial scanned profile of a calibration grating before (top) and after (bottom) a compensatory tilt of merely 1.33° and 1.37°, respectively on the X- and Y-axis.*

2.5 Preliminary internal characterisation

Just as a quartz probe is here the tool collecting topographical data towards the reconstitution of images, so can it be used within the very same setup as a contact detector in order to evaluate the performance of its other constituents: namely, the actuators and overall mechanical assembly. Here, testing is conducted to find out how accurately the system can be expected to effect the medium magnitude Z displacements which will be used in the course of experiments, notably during the approach towards the surface, as well as whether the system is afflicted by any creep or drift on the Z-axis which would affect the slope of the obtained images.

2.5.1 Actuator overshoot

A quartz probe with tip (3.58 MHz, Q=5k) was used as a contact sensor to determine the Z coordinate of the surface (Z0) at a given point using the smallest possible steps from the nanopositioner. The actuator was then raised back by about 10 micrometers to a reference

position (Z1). From there, single steps going down by a set distance, starting at about -9 µm then incrementally increased, were applied one by one. Each time the actuator was reset to its reference position Z1 before a new step was undertaken. The lowest single step value resulting in a surface contact detection was recorded. Afterwards, the actuator was again slowly brought down to contact using the smallest possible steps in order have the initial surface coordinate Z0 confirmed, which it invariably was. This process was repeated at three different points on a nondescript aluminium alloy surface. At each point, the final value resulting in contact was tested ten times starting from Z0, each time resulting in contact detection. The results show that for this range of values, a systematic overshoot is obtained: meaning that the distance travelled by the actuator is always, and at a given point repeatably, higher than the input distance targeted by the control software. The values of the overshoot range between 2 to 4 %. The difference in value between locations can be accounted for by a variable degree of humidity across locations, as well as the wear and shape of the tip, and shape of the surface.

Raw data: - Location 1: Z0=-19.05 µm; Z1=-10 µm; minimal travel range to contact: -8.85 µm ± 0.01 µm; corresponding overshoot: 2.26 %
- Location 2: Z0=-19.03 µm; Z1=-10 µm; minimal travel range to contact: -8.70 µm ± 0.01 µm; corresponding overshoot: 3.79 %
- Location 3: Z0=-19.05 µm; Z1=-10 µm; minimal travel range to contact: -8.78 µm ± 0.01 µm; corresponding overshoot: 3.08 %

2.5.2 Overall Z-axis drift

Strong Z creep was observed in the distance between the tip and sample, decreasing at a speed between 0.1 nm/s and 0.3 nm/s several days apart and with consistent values at a given time. Possible causes are:

- Actual Z drift from the actuator. This would be confirmed by the fact that the X and Y scans over a same region also drift slightly over time, and is the most likely explanation.
- Expansion of the wax substrate, which however is here unlikely to reach such amplitudes long past recrystallisation.
- Mechanical drift on the snap-in contacts between the probe holder and actuators.
- Any combination of electromagnetic forces, quartz stiffness, tip angle and stiffness or meniscus effects attracting the tip towards the sample.

Considering these hypotheses, the tip was placed up to several micrometers above the surface. At rest, meaning in the absence of any actuator input, the system was subsequently found to enter into contact with the sample surface at the expected time given the observed drifting speed, discounting the influence of proximity forces as a cause. As it can not be related to the oscillation control of the probe, here used as a contact detector only and with repeatable results, this drifting effect was therefore considered as an exclusively mechanical or piezoelectrical phenomenon, and compensated for accordingly in any long-running scans.

2.5.3 Adhesion and meniscus effect

Adhesion effects may be noticed, wherewith raising the tip after it has entered in contact with the sample surface does not immediately break this contact according to the probe feedback signal (here Δf), despite the closed loop actuators indicating a higher position through their sensors – a higher position at which previously no contact had been established with the surface. This can be the result of a meniscus having formed, or local adhesion from attractive van der Waals or electrostatic forces overcoming the rigidity of the system. Adhesion can understandably lead to unpredictable but undesired behaviour during the course of scanning.

In high ambient humidity conditions, testing was conducted (on nondescript wax, silicon or steel surfaces) to find out how far up the tip may need to be withdrawn to disengage from the meniscus that could be assumed to form at the interface. After initially entering in repulsive contact with the surface, the probe had to be raised upwards of 500, 650 or 750 ($\pm$ 50) nanometers before breaking free of the Δf values indicating contact. In such high humidity conditions, pushing the probe further into a hypothetical second degree of contact with a solid surface beneath revealed no clear step but rather an uninterrupted gradient, making it impossible to distinguish between the meniscus and the surface through the probe and suggesting that a meniscus is only formed upon coming near solid contact to begin with. A takeaway of this experiment is that when the formation of a meniscus can not be avoided, it is better for the entirety of the experiment to be conducted within the meniscus.

In regular ambient conditions, adhesion effects of a lower range have been observed, varying between 2 and a few dozens of nanometers required before breaking off contact (no discernible difference was found in this regard when modulating the quartz oscillation amplitudes, multiplying or dividing up to threefold). An approach-retract curve can hence seem affected by hysteresis. While minding the downwards drift identified on the system, it was also noted that the Z coordinate at contact would vary after adhesive effects, resulting in a loss of relative reference between the tip and sample. This may help explain irregular height differences on otherwise similar profiles between several lines of a raster scan.

Note however that another cause which provokes or strengthens these adhesive effects is the state of the tip, the end of which can have decayed due to prolonged use. For a larger end-area of the tip, greater adhesive forces are to be expected. Furthermore, if the tip is not rigid enough or if it ends up being crushed or bent into an angle at its end, it may be driven to couch against the surface, at which point its deformation may be accountable for changes in relative tip-sample positioning.

2.6 Adopted conventions

In the following experiments, the fabrication of all probes based on single-crystal models (3.58 MHz or 10 MHz) was conducted according to the design settled on in the previous chapter, with tip lengths between 0.5 and 2 mm. Fig. 3.8 presents the colour scale used in the images obtained. "Forward scan" will refer to the topographical data obtained from the left-to-right direction of raster scanning, and "backward scan" the reverse (right-to-left) direction of the same scan. Images are oriented as scanned from top to bottom.

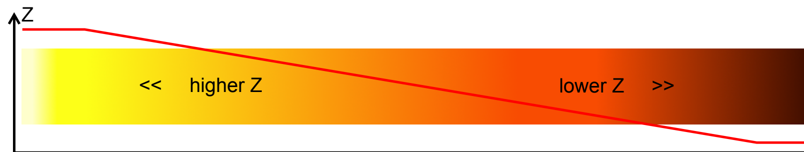

Figure 3.8 - *Colour scale used to represent relative height contrast in this work: lighter colours will denote higher Z coordinates (top surfaces), darker colours lower Z coordinates (bottom surfaces).*

Two-dimensional overhead images are as provided by the Nanonis software. Three-dimensional images were constructed from raw data by Gwyddion [Nečas 11].

3 Attractive mode FM-AFM

In this work, the "attractive mode", "non-contact mode" or "near-contact mode" is acknowledged when distinct pull-in and contact phases (see Fig. 3.9 & 1.8) can be identified during an approach-and-retract procedure between tip and sample. When the attractive zone isn't attainable or cannot be applied to scanning in a stable fashion, either due to the probe, sample or external conditions, we will default back to the repulsive mode in the next section.

3.1 32.768 kHz probe on calibration grating

32.768 kHz tuning forks exist in several models from various manufacturers. Based on data from over a dozen probes fabricated from the Citizen CFS206 series, they can only irregularly achieve attractive mode imaging in ambient conditions. Probes fabricated from another model, the thin Micro Crystal MS1V-T1K series, have been found to be rather more consistently operable in the attractive mode, supposedly due to their smaller mass, lower stiffness and greater sensitivity. Probes based on 32.768 kHz tuning forks are the earliest and most commonly found in the literature, and imaging results with any different quartz components or overtones selected in the previous chapter will be compared to those obtained here on the same setup with 32.768 kHz based probes.

The probe used in the displayed images (Fig. 3.10) is based on a CFS206 quartz tuning fork.

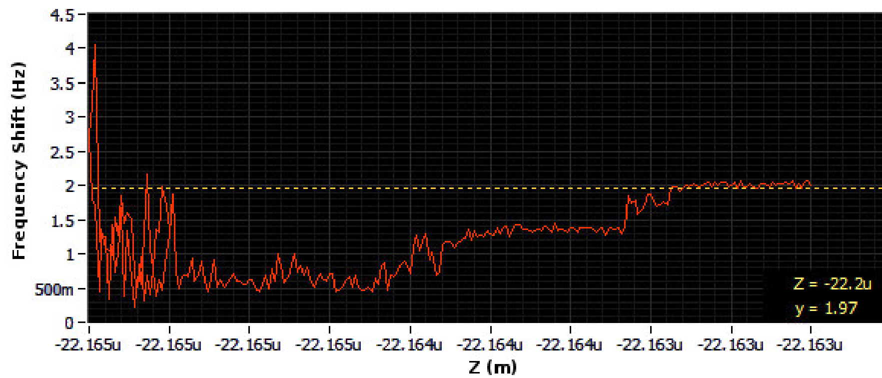

Figure 3.9 - *Approach-retract curve at a very slow speed (0.1 nm/s). In ambient conditions, attractive forces are here sensed approximatively 2 nanometres before repulsive contact forces are first detected (positive frequency shift, to the left).*

The probe with mounted tip has a fundamental frequency f_0=32.32 kHz, quality factor Q=3200, and is used at a ΔF set point of -0.10 Hz, with a drive amplitude of 50 mV. Overall stable scanning speeds attain 1 to 1.6 µm/s. A drawback of attractive mode imaging, with a simple PI controller, is that any accidental contact with the sample results in a switch from negative to positive Δf and results in instability, as can be partly seen in Fig. 3.11.

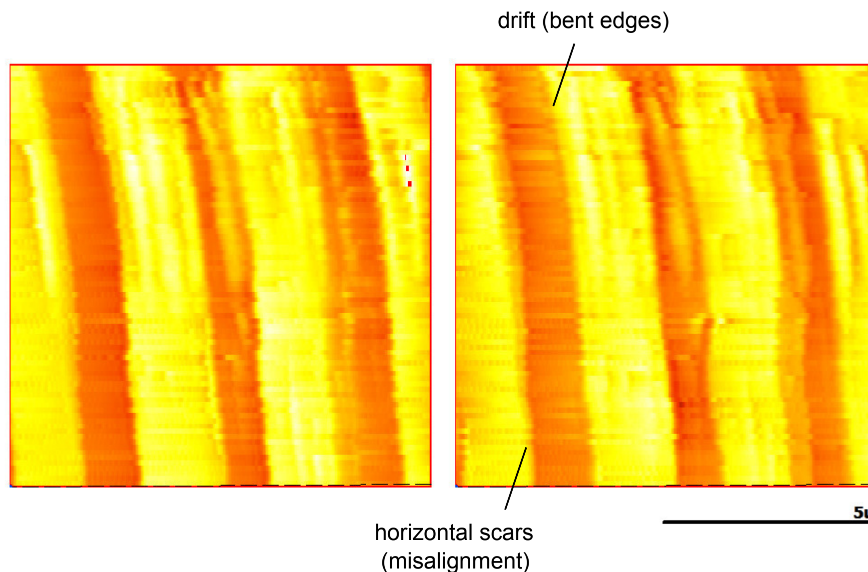

Figure 3.10 - *Attractive mode image on a calibration grating pattern (3 µm pitch, 100 nm ridge height) using a 32.768 kHz probe imaging at a linear scanning speed of 1.6 µm/s. Backwards (left) and forward (right) scans. The same longitudinal bumps and ridge flaws are revealed in both scanning directions, which confirms that they are indeed physically present (ie. the result of wear on the sample) and not mere imaging artefacts.*

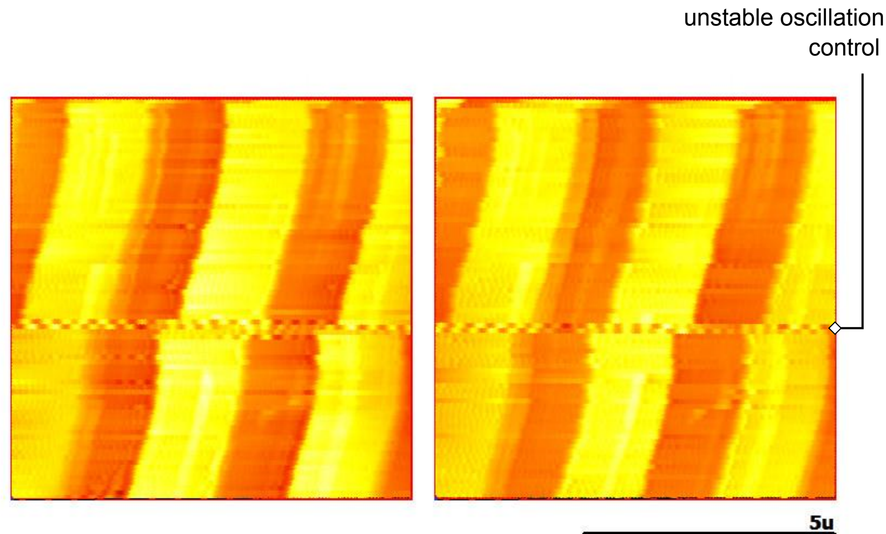

Figure 3.11 - *Attractive mode image with the same calibration sample and probe, at a linear scanning speed of 1.1 µm/s and scanned at an angle. Backwards (left) and forward (right) scans. The middle section is interrupted by a period of instability during the scan, which results in a cut in the image as well as an apparent distortion effect shortly afterwards.*

3.2 32.768 kHz and 196 kHz overtone probes on paraffin wax

Two different probes based on the same model (CFS206; frequencies with tip f_0=32.3k and 32.4k, and quality factors respectively Q=6600 and 8300) showed consistent pull-ins, i.e. sensitivity to attraction, within 2 nm above the surface on paraffin wax. However, due perhaps to significant drift and the hazardous nature of the sample, the attractive mode was not found to be stable, and the repulsive mode was resorted to instead.

Additionally, the overtone mode of another model (MS1V-T1K), previously mentioned for having a high quality factor comparable to that of the fundamental mode, was tested. While the fundamental resonance of these probes (frequencies with tip f_0=32.7k and 31.6k, and quality factors respectively Q=4200 and 2400) proved to be satisfactory and repeatably sensitive to attractive forces, within 2 nm above the surface as well, their overtone modes (frequencies with tip f_0=197.7k and 195.9k, and quality factors respectively Q=9200 and 3200) were found to have low signal-to-noise, with noise at least one order of magnitude higher than at their fundamental resonance, and therefore unusable for attractive mode imaging, as well as comparatively too lacking for repulsive mode imaging. This underwhelming performance finds confirmation in the results of simultaneous works on similar components from the same manufacturer [Babic 15].

3.3 3.58 MHz probe on silicon surface

Out of over ten probes based on a CA206 3.58 MHz quartz, only one was found to be intermittently sensitive to attractive forces 1 to 2 nm above the surface. This result was non-reproducible, and may possibly be attributed to either environmental conditions such as humidity or polarisation at the apex, or to the presence of intermediary elements between the tip and sample. Probes based on these large "contoured beam" models are therefore considered generally unsuitable for attractive mode imaging in ambient conditions.

3.4 Overview of the attractive mode

In uncontrolled ambient conditions, standard 32 kHz tuning forks are sometimes suitable for attractive mode imaging, and the smaller models are more consistent in this regard. Of those models that were tested, most were not optimised by the manufacturer for their overtone resonance, and ultimately none presented any advantage over the fundamental mode. The higher frequency quartz models did not yield any repeatable results in the attractive mode.
On one hand, attractive mode FM-AFM seems to offer better stability with lower frequency shift values as stable set points, which in turn allows for faster and more reactive Z control, and therefore greater scanning speeds. On the other hand, any shift between attractive and repulsive zones during a scan has the potential to be at best compromising for the image, and at worst destructive for the tip and sample. As accidental contact is more likely at high scanning speeds and for larger objects with greater ridge heights, the attractive mode seems to suit greater speeds for rather flat surfaces only.

4 Repulsive mode FM-AFM

As opposed to attractive mode imaging, this is the dynamic "contact" mode which consists in sensing repulsive van der Waals forces. Since repulsive mode imaging involves greater friction and is more damaging to the tip, the positive ΔF set point is chosen as the lowest possible shift with which to reliably operate above noise.

4.1 32.768 kHz probe on paraffin wax

The speed comparison in Fig. 3.12 was taken on uncontrolled wax steps of height in the hundreds of nanometers range, with a probe based on a CFS206 quartz tuning fork (with mounted tip, f_0=32.427 kHz and Q=8300). From 2.3 µm/s and below, the improvement in image quality is greatly due to the increased time available for the Z actuators to scan down to the surface, i.e. a reduction in parachuting-related artefacts.

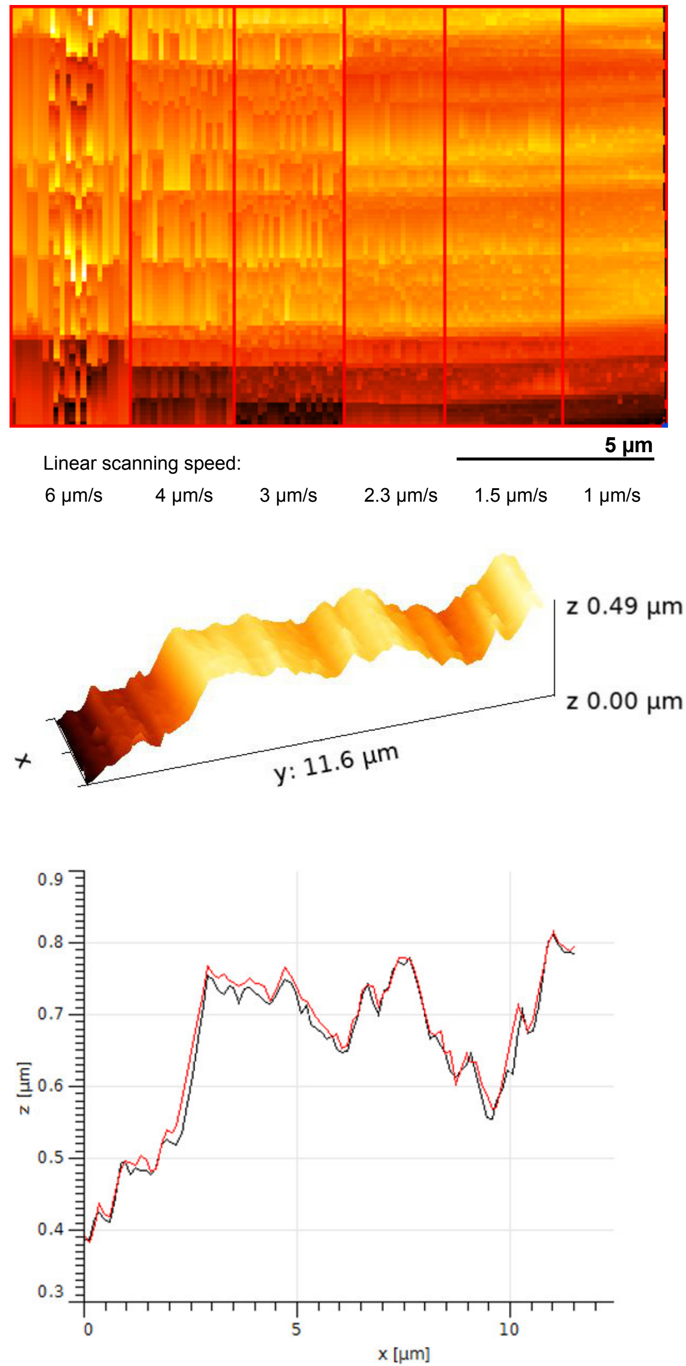

Figure 3.12 - *Paraffin wax image, repulsive mode: 32.768 kHz probe speeds comparison; 3D illustration applied in combination with the colour scale, and profile curves (black=forward scan, red=backward scan) corresponding to the scanned area for the slowest speed (1 µm/s).*

4.2 100 kHz probe on paraffin wax

Testing with several probes based on CFV206 100 kHz tuning fork models showed no improvement over their 32 kHz counterparts in performance; noticeably, either the PLL bandwidth has to be reduced (halved to 800 Hz) or the oscillation drive amplitude greatly increased (to 200 mV or above) to maintain a stable phase lock-in on the resonance of any probes based on these models. In addition to the lower PLL speed, signal-to-noise levels were significantly worse than with the previous models, and heavy compromises were required in order to obtain stable scanning results. The image taken on paraffin wax (CFV206 probe, with mounted tip at a fundamental frequency f_0=97,797k and Q=9200) shows early degradation past low scanning speeds (Fig. 3.13) and pronounced parachuting artefacts due to the necessary Z-controller compromises (Fig. 3.14).

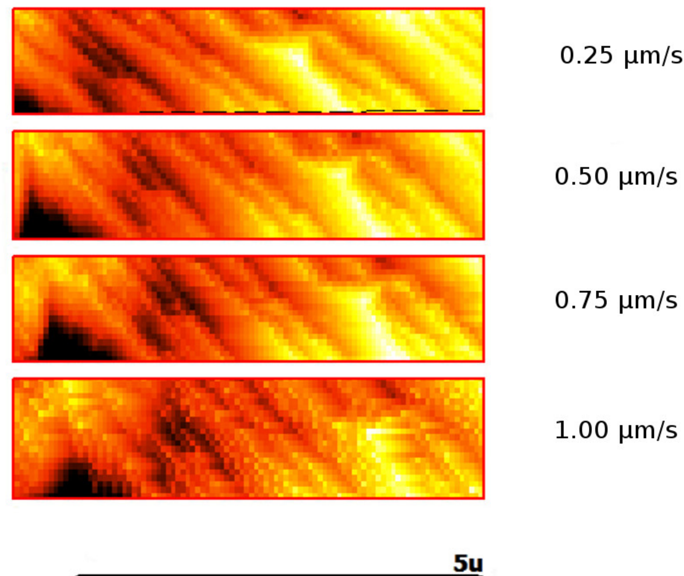

Figure 3.13 - *100 kHz probe speeds comparison on wax. The image noticeably degrades past low speeds (note however the scale, here greater than in the previous figures).*

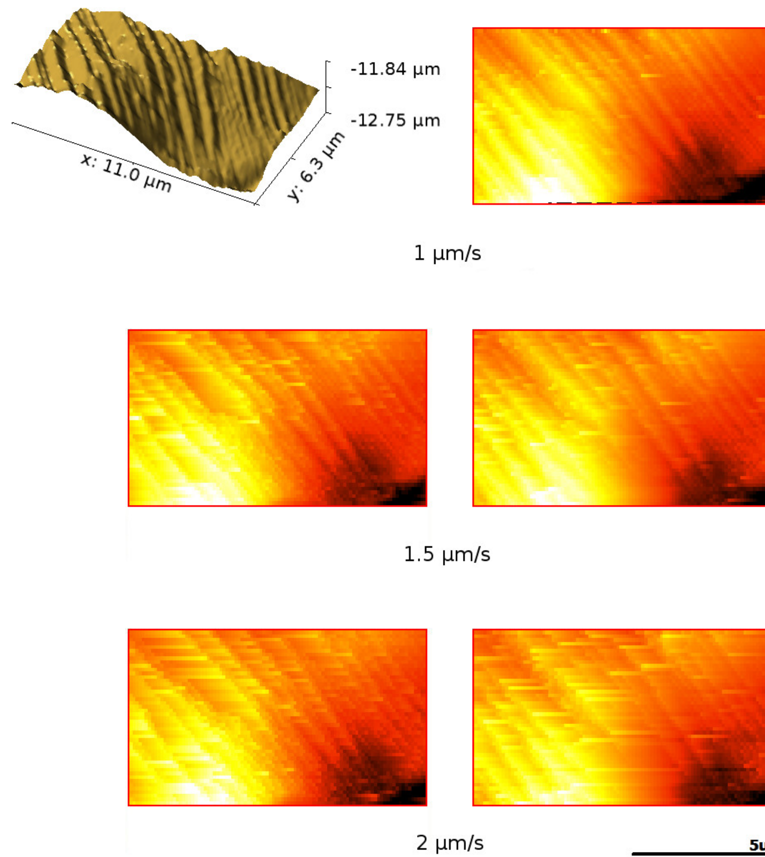

Figure 3.14 - *100 kHz probe speeds comparison on another wax area, backward (left) and forward (right) scans. Heavy parachuting artefacts are visible due to a necessarily slow Z controller.*

4.3 100 kHz probe on calibration grating

Again, the same tuning fork model (CFV206 probe, with mounted tip at a fundamental frequency f_0=97,797k and Q=9700) shows unremarkable performance relative to 32 kHz based models (Fig. 3.15). It is notable that scanning with these shorter probes only accommodates a very narrow range of parameters on the Z-controller, even at slow speeds. This is revealing, in that it means the probe is not adaptable to a wide range of samples with a same set of parameters – and therefore singularly unsuitable for any unknown samples which could alternate between large and low-height topography.

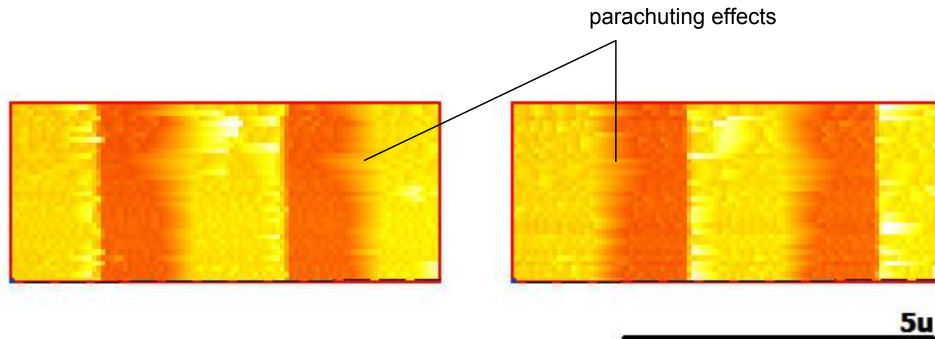

Figure 3.15 - *100 kHz probe on calibration grating (3 µm pitch, 100 nm ridge height), scanned at 600 nm/s. Forward (left) and backward (right) scans already display parachuting artefacts down the corresponding direction, which are made worse at higher scanning speeds.*

4.4 10 MHz probe on calibration grating

Initial testing with higher frequency resonators was conducted with a 10 MHz thickness shear quartz (here Abracon AB308, with mounted tip f_0=9.997536 MHz and Q=13000). Fig 3.16 displays a slow speed scan on a calibration grating. An immediate downside of resonators in the 10 MHz range, as excited by the equipment used in this setup, was found to be the resonance phase, which after capacitance balancing was of -160°. This likely evidence of phase delay may be linked to the limits of the pre-amplifier electronics. Due to this, further testing on thickness shear quartz resonators was relegated to 3.58 MHz models.

4.5 3.58 MHz probe on calibration grating

The first images obtained at a faster scanning speed with a 3.58 MHz probe (based on CA206, with mounted tip at a fundamental frequency f_0= 3.579144 MHz, with Q = 16600, and at a set point ΔF = 0.3 Hz) seem accurate on a line-per-line basis, but show inconsistencies when the lines are assembled into a complete image (Fig. 3.18) as they are misaligned. Images taken at an angle (bottom Fig. 3.18), however, emphasise issues with the scanned shape itself, despite being taken at a lower speed. Fig. 3.19 explores the imaging artefacts encountered at scanning speeds above 40 µm/s, with apparent noise patterns, then increased blurring, and warping at the corners of the scanned area which highlights the issue of brutal speed inversion happening in the vicinity of surface details, i.e. non-flat areas.

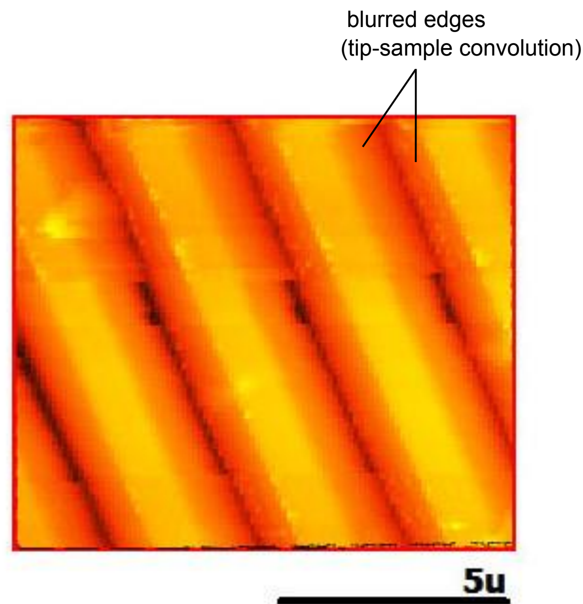

Figure 3.16 - *Repulsive mode image on a calibration grating pattern (3 µm pitch, but 500 nm ridge height) using a 10 MHz probe imaging at a linear scanning speed of 1 µm/s. Although the edges of the upper surface seem well contrasted, the greater ridge height of this sample is not satisfactorily rendered due to the shape of the tip (Fig. 3.17).*

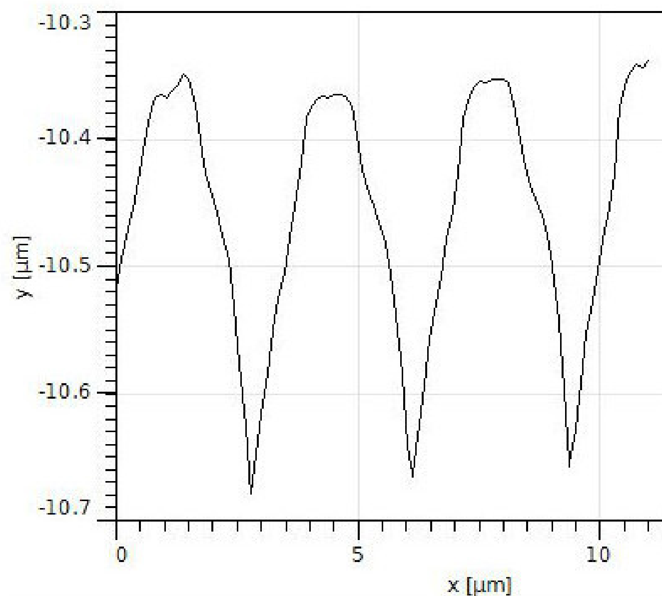

Figure 3.17 - *The corresponding graph profile of a line scan from Fig. 3.16 reveals the influence of the radius and shape of the tip, which cannot probe down to the bottom surface of the sample as it is stuck at about 60% of the 500 nm ridge height.*

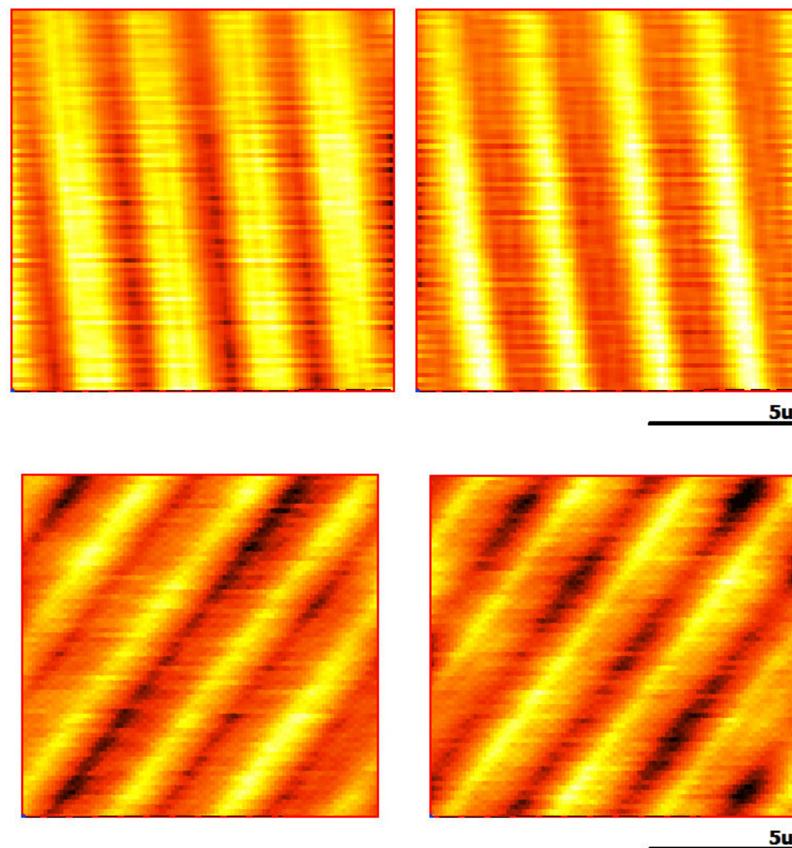

Figure 3.18 - *Repulsive mode image on a calibration grating pattern (3 μm pitch, 100 nm ridge height) using a 3.58 MHz quartz probe. Top: scan with a linear scanning speed of 28 μm/s (12x12 μm, 80 lines in 75 seconds). Backwards (left) and forward (right) scans are in concordance, but slashed edges or horizontal scars are a result of base height errors from switching between scanned lines. Bottom: scan of the same area at an angle, with a linear scanning speed of 22.3 μm/s.*

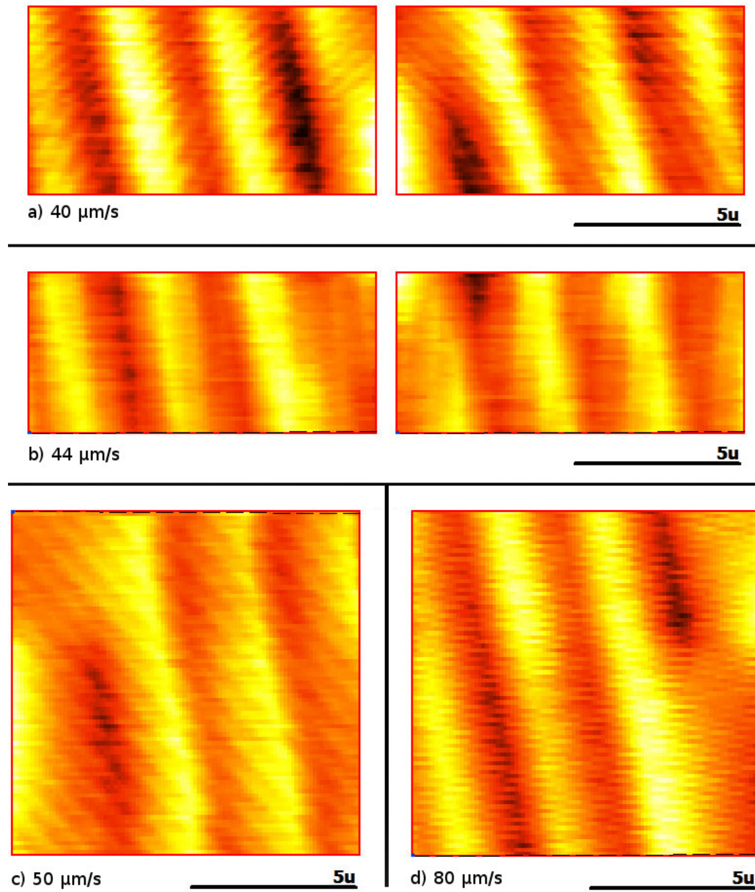

Figure 3.19 - *Repulsive mode image with the same calibration sample and probe, at 40 µm/s (a) to 44 µm/s (b). Blurrin, rippling and warping of the image become increasingly apparent, as well as dimorphism between the backwards (left) and forward (right) scans; at 50 µm/s (c) and 80 µm/s (d), blurring increases and edges are no longer consistently aligned even in the direction of the scan, not merely due to height errors but also X and Y errors, especially at the sharp turns at the end of the raster area.*

Fig. 3.20 illustrates a more progressive comparison of performance according to speed, conducted on the same calibration sample with a similar probe (CA206, with fundamental frequency f_0=3.578861 MHz and Q=18800 at a set point ΔF=0.2 to 0.4 Hz under the influence of thermal drift). The previously identified artefacts indeed begin to appear around and beyond 20 µm/s. Performance at lower speeds is similar, which is next confirmed on a wax sample.

4.6 3.58 MHz probe on paraffin wax

Images were taken with the same probe (CA206, with fundamental frequency f_0=3.578861 MHz and Q=18800 at a set point ΔF=0.15 to 0.5 Hz) here on an non-regular sample with varying step heights. Fig. 3.21 shows no obvious difference with a scanning speed alternated

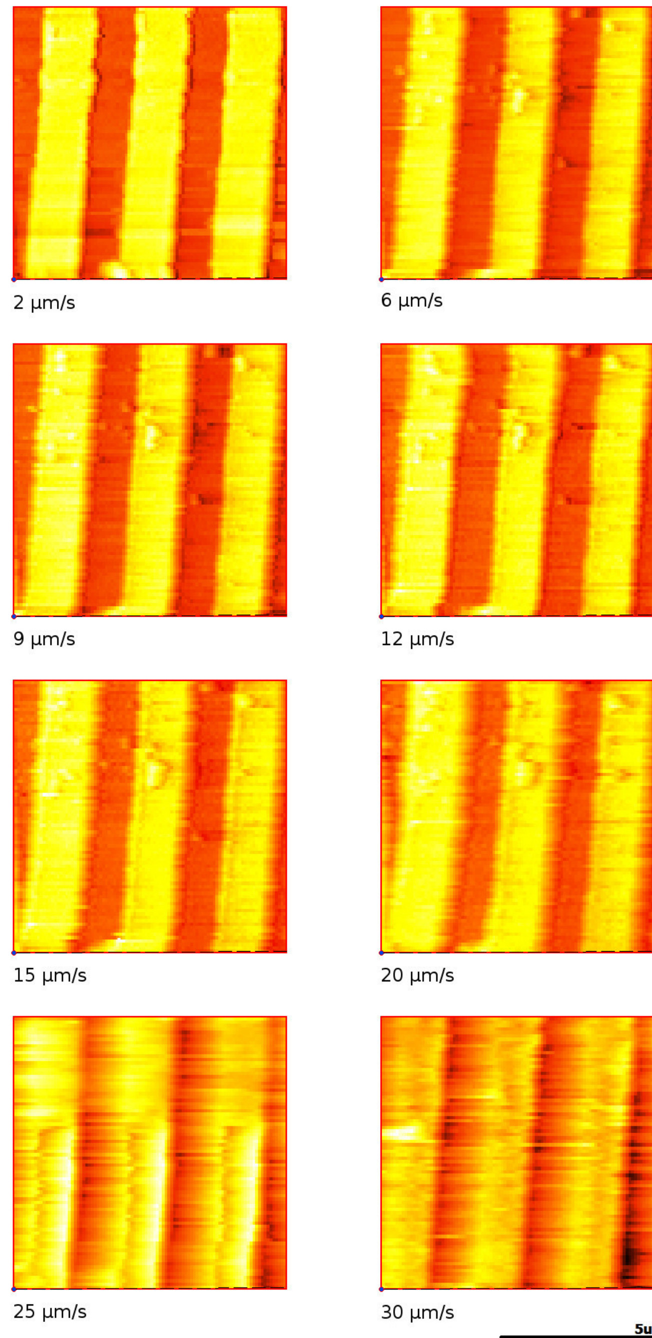

Figure 3.20 - *Repulsive mode image with the same calibration sample with a 3.58 MHz probe at various linear scan speeds. Only forward scan images are displayed. Backward and forward scans are by and large identical. Image quality drastically drops beyond 20 µm/s.*

at and between 0.5 and 7 µm/s throughout the area. Fig. 3.22 establishes a progressive speed comparison on another area, with the appearance of corresponding artefacts, notably parachuting on the higher ridges and the blurring and slashing of edges at faster speeds. Unlike images taken on a calibration sample with known dimensions and orientations, the misalignment from line to line is harder to identify, and cannot be reliably corrected through post-processing, as it is not possible to tell from a single take to what precise degree the undulating edges are a result of artefacts or of the actual topology of the sample: the reconstitution of an image in practice becomes a stitching problem. Fig. 3.23 and 3.24 are an attempt at comparing what artefacts can be observed within single scanned lines, and those that appear on the image as a result of the stitched image and compounding of the lines. Where single scanned lines show a gradual attenuation of details and agglomeration of surface features, the cross section profile curve taken across a span of the scanned area would include deformations of the entire shape. A comparison of the images and curves taken at a scanning speed of 15 µm/s, for instance, shows that stitching deformations which are evident on the surface image are, on the cross-section curve, not easily distinguished from the loss in depth-detail that an increased speed entails on the corresponding line scan curves.

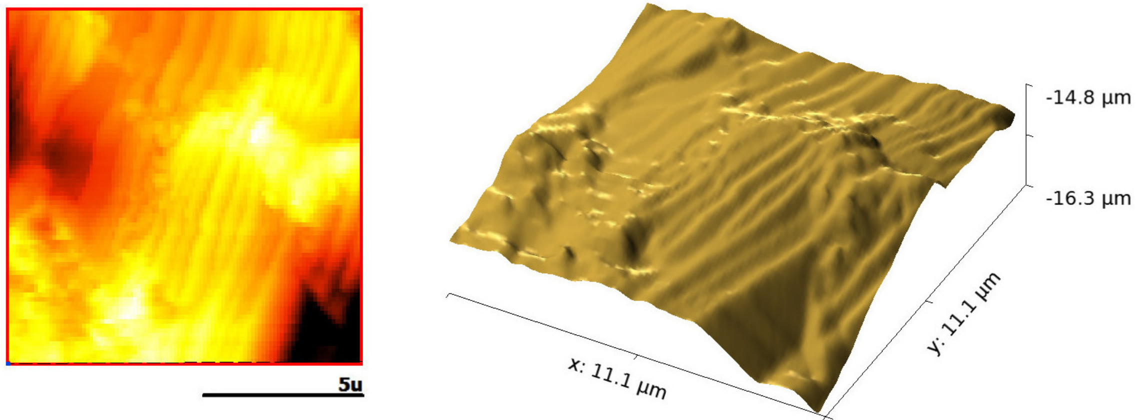

Figure 3.21 - *Repulsive mode image on a non-specific wax surface, with linear scan speeds made to vary throughout between 0.5 and 7 µm/s without any obvious differences observed in topological data quality. Backward and forward scans are identical.*

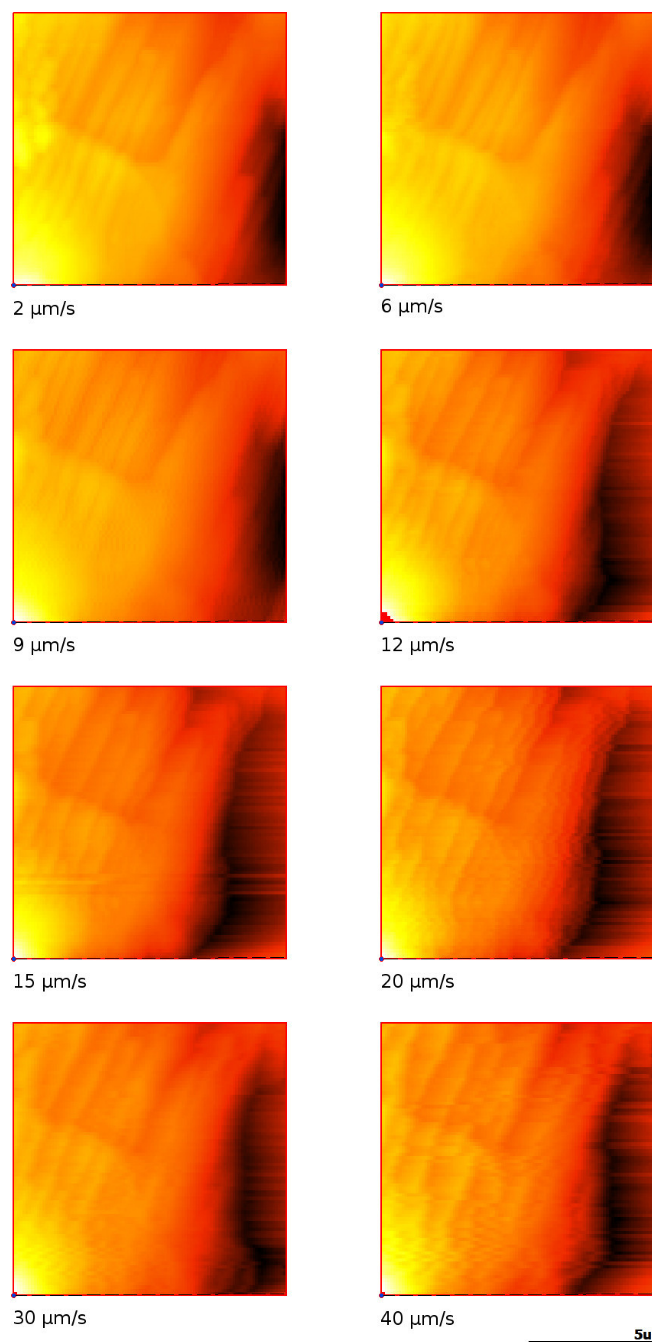

Figure 3.22 - *Repulsive mode image on another non-specific area of wax surface at various linear scan speeds. Only backward scan images are displayed. Backward and forward scans are at first identical, but starting from 9 µm/s forward scans progressively become unexploitable due to the best compromise in settings resulting in heavy parachuting effects for such ridge heights. A clear drop in image quality regardless appears from 12 µm/s onwards.*

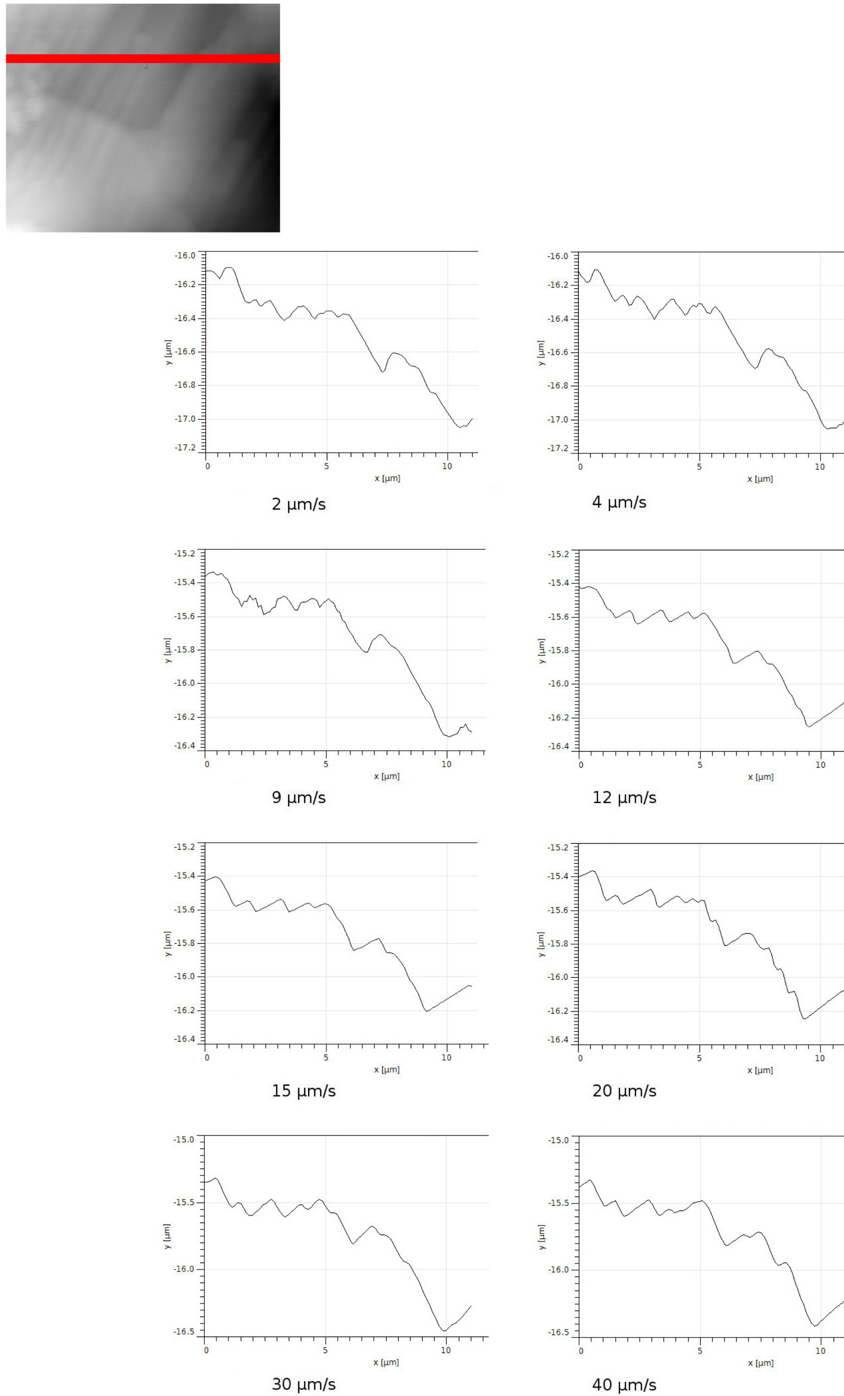

Figure 3.23 - *Profile curves comparison for one corresponding line (top left) of the previous image.*

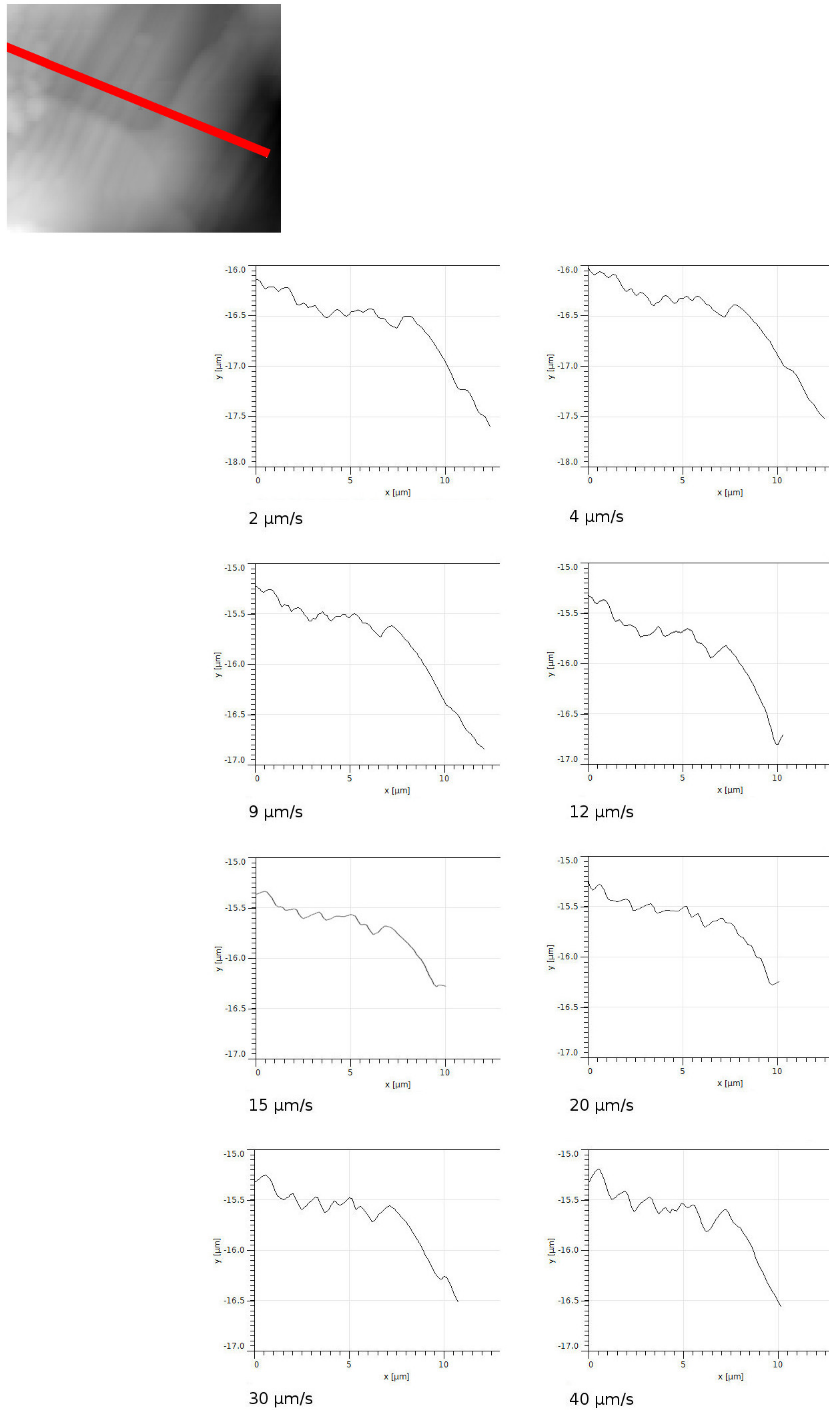

Figure 3.24 - *Profile curves comparison for a cross section (top left) across the area of the previous image. Compared to the previous single line curves, this also includes information on a line-to-line basis.*

Table 3.2 - *Comparison between the FM-AFM scanning speeds attained with probes based on different quartz resonators, for visually comparable image results. * Measurements in ambient air, with mounted tip.*

Quartz	**Frequency ***	**Q ***	**Scanning speed** ($\mu m/s$)
CFS206	32.32 kHz	2400	1.6
CFV206	97.79 kHz	9200	$<$1
XT32K	3.578 MHz	18800	12

5 Conclusion and perspectives

The imaging experiments in ambient conditions conducted in this chapter confirm that the compromise made in using higher-frequency quartz resonators obtained from off-the-shelf components is one between resolution and speed. Compared to lower frequency tuning forks, the thickness shear resonators in the MHz-range selected in the previous chapter can indeed be used for up to ten times faster scanning while maintaining comparable image quality in the repulsive FM-AFM mode. However, the MHz probes investigated in this chapter are not sensitive to the attractive mode in ambient conditions.

A different relation is to be considered between speed and sensitivity: higher sensitivity means that sensor feedback can be used for control around smaller frequency shift set-points, and thus that Z-axis control can remain stable while using faster parameters. Sensitivity is therefore not to be entirely discounted even when scanning speed is prioritised, as Z-axis control would be the limiting factor when probing deeper samples with ridge heights above a micrometre.

Sensitivity and speed must be taken in consideration together with the operating range of a probe, i.e. its versatility: higher-frequency tuning forks were found lacking, in these experiments, due to the nature and design of the resonators themselves limiting the permissible bandwidth of oscillation control, and to the very narrow range of parameters the resulting probes accommodate. This lack of flexibility makes them unsuitable towards use on a wide range of samples, or on samples with unknown topography. Tuning fork overtones were also found unsatisfactory with the models tested here. In conclusion, only the 3.58 MHz probes investigated in this chapter are shown to be well suited for faster scanning at lower resolutions. Perspectives remain to be explored as to whether higher-frequency probes, by yielding more data, could also provide improvements over their lower-frequency counterparts even at low scanning speeds.

Chapter 4

SEM-embedded micro-robotic sensing with quartz tuning forks

Self-sensing quartz probes are deployed towards applications in both topography and quantitative force measurement. The previous chapter has focused on the first aspect in the ambient environment; we now turn towards quantitative measurement, and exploit the specific advantages of self-sensing for a robotic stiffness measurement application on a batch of samples in a scanning electron microscope (SEM). The experimental protocol, with regard to the dimensions of the samples and for the reasons which were expounded on in chapter 1 (Sect. 1.2.3 & 1.3.2), calls for the use of the SEM over optical microscopy. We have seen that electron microscopy is an important observation tool for micro- and nanorobotics, and the interest for quartz probes in this field warrants its study in SEM-embedded conditions. As the SEM chamber is a vacuum environment, which notably due to reduced friction affects the performance of a quartz resonator to a significant extent, this study will first look into the influence of a SEM and of low pressure on micro-robotic sensing systems with quartz probes as a whole. In addition to the quartz probe itself, effects on the piezoelectric actuators displacing the probe as well as the other issues engendered by the concurrent use of a SEM – namely, those related to the electron beam – will also be explained, the objective being here to detail all that must be taken into account when setting up quartz probes for SEM-embedded experiments. The second part of this chapter then moves on to the proof-of-concept application for *in situ* stiffness characterisation on micro-membranes. A 9 Degrees-of-Freedom piezoelectric actuation system, controlling the quartz tuning fork probe holder and sample platform, is embedded in a SEM and complemented by virtual reality and automation tools, showcasing multiple non-destructive and repeatable local results on individual samples of several types.

1 Quartz probe sensing and in air, vacuum and SEM environments

The first difference which presents itself on a resonator when comparing it in ambient and vacuum environments is that of the quality factor being greatly increased from the absence of friction with the air, as seen in chapter 2 (Sect. 1). Vacuum chambers at various pressure levels are indeed used in AFM, both with cantilevers and self-sensing probes. The benefits sought in vacuum AFM can be the increase in Q factor, but also the absence of humidity (at regular temperatures), or the maintaining of specific sample states (at very low temperatures; e.g. the triple point of water[1] for some aqueous samples). The use of a SEM in the following micro-robotic experiments involves a vacuum chamber because of the way a SEM operates, and chiefly for this purpose – global real-time vision with great resolution and depth of field; the overall impact of this vacuum environment on the micro-robotic sensing system will be covered here. The piezo-electric stick-slip actuators used in this setup are to some extent affected, which will be mentioned first. The influence of the higher Q, lower-dissipation environment on the response speed and sensitivity of quartz probes will then be examined; lastly will be addressed those effects which are specific to a SEM environment and linked to the electron beam.

1.1 Setup and pressure

Although the previous parts of this work have taken special interest in higher-frequency probes, all experiments in this chapter are conducted with probes based on 32.768 kHz quartz tuning forks. Aside from the operating frequency being sufficient for the applications in question, this is mainly due to the facilities being in this case equipped with another setup, the quartz control part of which is ultimately only functional in the range of a few dozens of kHz. The actuators are for this section embedded in a Zeiss EVO-LS25 electron microscope and used through manual or custom control (rather than through the previous Nanonis SC4 package); quartz driving and oscillation control are otherwise conducted much in the same way as described in the previous chapter (Sect. 1.1), with a Nanonis OC4 oscillation controller instead of the high-frequency ZI PLL system, and with a lower frequency range design of the same type of pre-amplifier.

Besides the change in quality factor, the eigenfrequency of a quartz tuning fork varies slightly with pressure; it stabilises when a certain vacuum level is reached. Experiments must therefore be conducted after the pressure level has sufficiently stabilised. Here, the frequency change is usually in the order of 6-10 Hz, and the frequency and oscillation amplitude values when pumping the vacuum chamber will have stabilised by the time a pressure of 0.1 Pa is reached, under which any changes are not distinguishable from thermal drift. The "high vacuum" referred to hereon, and at which the SEM operates, corresponds to a pressure down to 5 $\times 10^{-4}$ Pa.

Additionally, in the absence of convection through air, any ambient or local changes in temperature are communicated only by conduction. Any expected thermal drift therefore may take longer to manifest if it is due to the ambient environment surrounding the vacuum chamber, and any heating done within the chamber may take longer to dissipate.

[1] At a pressure of 611.657 Pa – the atmospheric pressure being 100 kPa.

1.2 Effect on the piezo-actuating system

The 9 Degrees-of-Freedom actuation system used in this chapter is a custom platform commercialised by Smaract GmbH, composed of stick-slip piezo actuators (Fig. 4.1). When used in a vacuum, their optical sensors must be switched to a low energy consumption mode, which provides feedback at a limited frequency when not in motion, in order to avoid overheating caused by laser detection with the aforementioned lower thermal dissipation rate.

Figure 4.1 - *Stick-slip piezoelectric actuator component (SLC1720) of the Smaract manipulation system, dimensions 22×17×8.5 mm.*

The actuation in the first section of this chapter is conducted through a control scheme with a dynamic model characterisation of these piezo-actuators [Lu 16]. With it, low-range piezo displacements (under 1.5 µm) have been shown to be, as expected, unaffected by pressure. Larger-range displacements use the stick-slip actuation scheme: with higher-frequency signals being applied on the piezo crystal, pressure having an influence on long-range displacement or displacement speed is not to be discounted. Changes are yet to be verified, and will be the subject of upcoming works.

1.3 Quartz frequency, quality factor and dissipation

To understand how the influence of the environment on the eigenfrequency and quality factor of a tuning fork differs from that of the fabrication process, we must clarify that friction with the air (added dissipation), inertial change (overall added mass), and imbalance (different mass added on the two prongs) are different phenomena. It has been mentioned in chapter 2 that breaking the balance of a tuning fork by adding mass to one prong (a tip) lowers its quality factor, and the more mass is overall added to the resonator (together with balancing), the more its eigenfrequency shifts down. Typical probe fabrication can bring the quartz tuning fork, after balancing, to a few hundred Hz under its original 32.768 kHz eigenfrequency or lower; although the oscillation amplitude is also affected, the quality factor can routinely be brought back to over half its original value in the tens of thousands. A vacuum environment, in comparison,

lowers this frequency by a few to a few dozen Hz, while heavily affecting the quality factor. The presence of air molecules therefore brings low inertial shift, but high dissipation. Inversely, added mass (here epoxy) i.e. a high inertial shift brings on its own only a limited amount of friction on the resonator, and dissipation from the fabrication process primarily comes from the imbalance between the two prongs. In comparison, the presence of an object with low mass but a loose fixation (Fig. 4.2) also entails low inertial shift, but high dissipation due to friction – which relates to the importance of a stable fixation for the glue and tip.

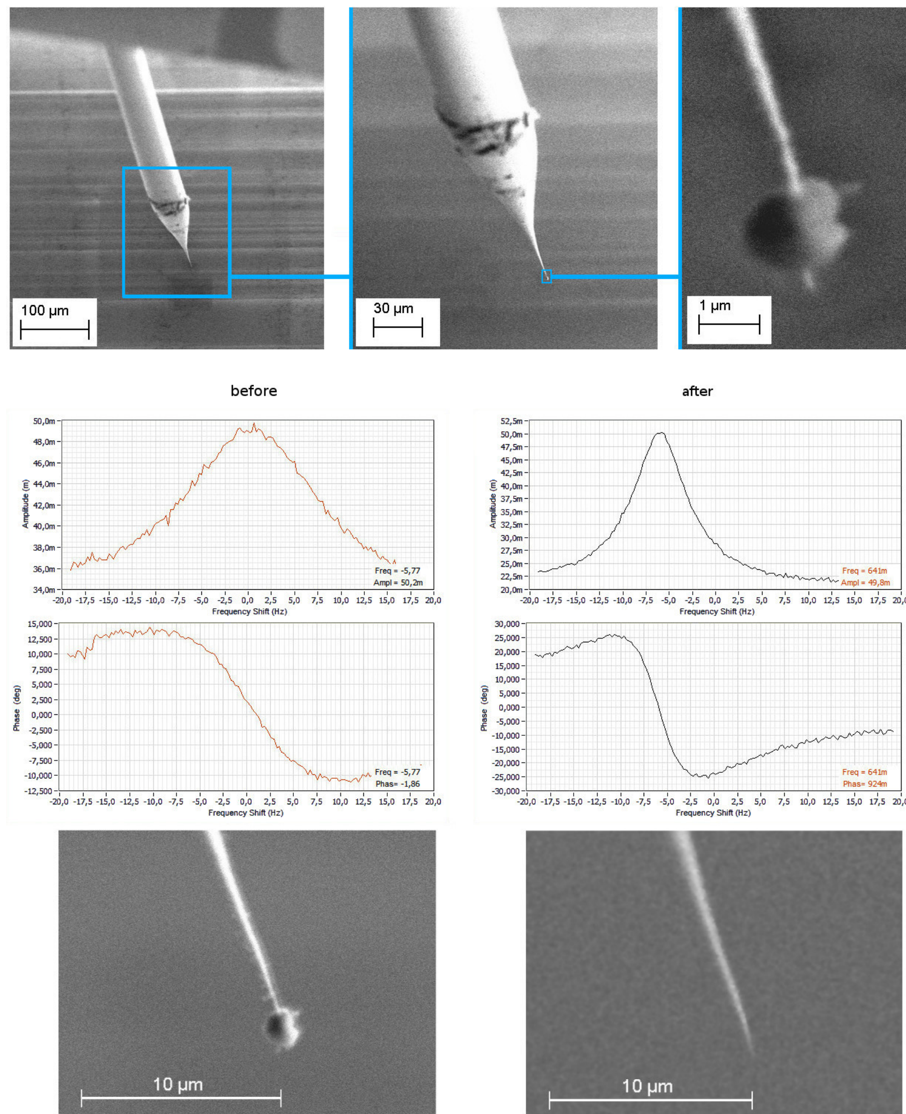

Figure 4.2 - *High dissipative effect of a micro-object impaled on the tip: resonance curves before (left) and after (right) its removal by focused electron beam: the eigenfrequency is shifted by less than 6 Hz (a value similar to the effect of air) by the object, the presence of which nonetheless divides the quality factor.*

The change in Q brought by the difference between air and vacuum environments as well as unbalancing is now to be examined as regards its effects on the settling time and sensitivity of a quartz probe.

1.4 Influences on settling time

While a greater Q improves sensitivity, the increased decay time limits the speed of operation of the quartz probe in operation modes which rely on sensing changes in oscillation amplitude, as does the lateral or shear-force mode [Antognozzi 03]. "Q control" methods have therefore been developed to electronically manage this value [Rodriguez 03, Jahng 07] by injecting energy in- (to increase Q in low-Q environments like liquids) or out of phase (to decrease Q in high vacuum, low-temperature environments) with the oscillation. The results of these methods widely differ and are still referred to as controversial, due to uncertainties as to related effects on signal-to-noise ratio or as to the extent to which the electronically shifted Q itself, rather than optimal scanning control or oscillation control settings, contributes to the measured sensitivity or speed improvements.

The influence of high Q (meaning low dissipation) on the response time of the probe can be understood in simple terms as increasing the time it takes for the oscillation to move from a state of high energy (the resonance, with high-amplitude oscillation) to a state of lower energy (any shift from the eigenfrequency, reducing oscillation amplitude). The difference between the presence or absence of air friction or of imbalance on the dynamics of the quartz probe can be illustrated by measuring the settling time of the oscillation amplitude when shifting the driving signal away from or back to the eigenfrequency (Fig. 4.3) (note that this only involves the driving voltage, without any phase-locking or gain control such as are used elsewhere in this work – the time constant parameters of which directly affect response times).

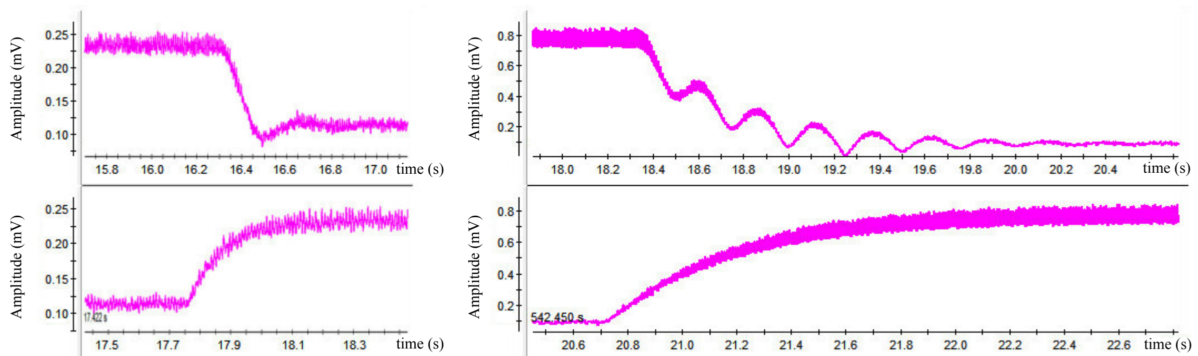

Figure 4.3 - *Amplitude response to shifting drive frequency away from (top) or back to (bottom) the eigenfrequency, in a vacuum at Q=7400 (left); at Q=32000 (right): as the notion of quality factor describes, it takes several times longer for energy to dissipate in the latter case.*

To compare how the different ways Q changes influence response times, we modify the Q

of a given quartz tuning fork by adding mass to one or the other of its prongs, until a lower quality factor close to that originally obtained in the air is reached in a high vacuum (Fig. 4.4) and measure the amplitude response when shifting away from the eigenfrequency by 1, 3 or 5 Hz. Results are grouped in Table 4.1. With the higher quality factors, a shorter settling time is noticeable when shifting the driving signal back to the eigenfrequency (higher amplitude oscillation). With a comparable quality factor (within 5% and with an eigenfrequency about 1.5% lower), the settling times still appear significantly (up to about 30%) higher in a vacuum, in line with a higher oscillation amplitude – the amplitude at the resonance being higher, but the amplitude outside of the resonance also having a higher baseline. Both Q and amplitude should therefore be considered when it comes to evaluating changes in settling times.

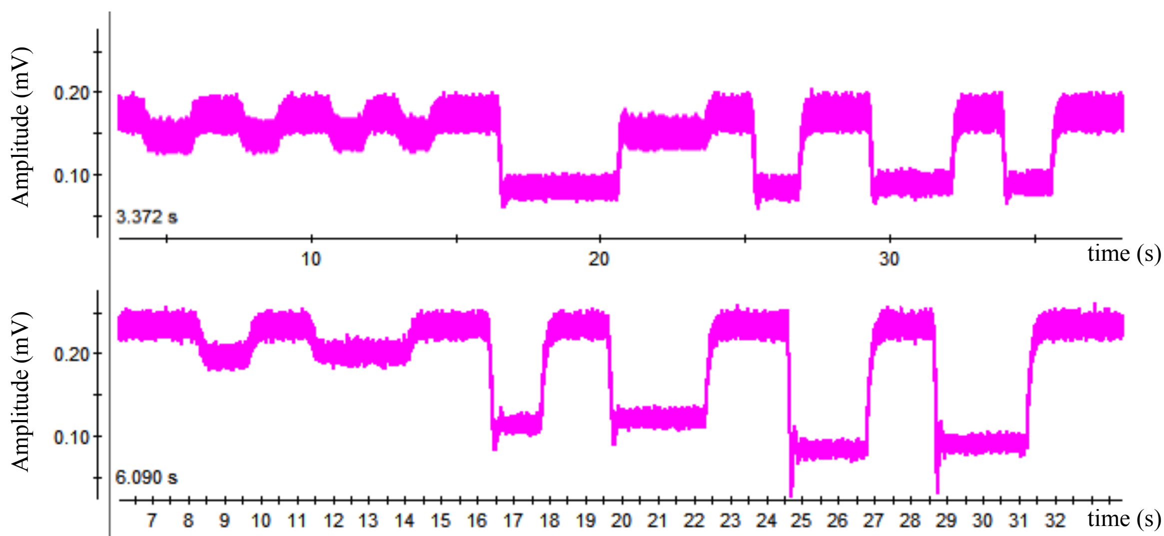

Figure 4.4 - *Amplitude response to successive shifts of 1, 3 and 5 Hz away from and back to the eigenfrequency of a quartz tuning fork originally in the air at Q=7100 (top); in a vacuum at Q=7400 after unbalancing the tuning fork (bottom). With a quality factor difference of less than 5% and a 500 Hz lower eigenfrequency, a significant increase in oscillation amplitude and overshoot is still observed in a vacuum.*

1.5 Influences on sensitivity

The role of the quality factor in the sensitivity of a tuning fork probe, i.e. the smallest amplitude of signal that can be sensed, is found in the expression of noise (Chapter 2, Sect. 1.3). Consequently, the increased sensitivity of a tuning fork probe in a vacuum environment should first be observable through reduced noise. In the setup used here, no significant reduction is noticeable in the phase signal (Fig. 4.5), meaning that the electronic noise level is above any potential difference; the frequency shift which locks onto the desired phase value based on that signal does not locally show greatly reduced noise at a given time, but does have an overall more stable value across durations over a couple seconds (Fig. 4.6).

Any further influence of the environment on tip-sample interaction should be observed in

Table 4.1 - *Amplitude settling time for changes in driving frequency: shifts of 1, 3 and 5 Hz from the resonance frequency are imposed on a single CFS206 quartz tuning fork driven at 100 mV in various states. Settling times are measured before and after removing the canister, in the air or in a high vacuum, and after adding mass (epoxy or glue) to the prongs to change the quality factor. – * Settling time back (if different): at the higher quality factors and as amplitude overshoots appear, the settling time when moving away from the shifted frequency and back to the resonance frequency become noticeably shorter, since the change towards a state of higher energy is less hindered.*

environment & weighing	$f_0(kHz)$	**Q**	δ**f** (Hz)	**Ampl. shift** (mV)	**Settling time** (s)	**Settling time back** * (s)
air (canister)	32,758	7100	1 3 5	28 85 111	0.24 0.29 0.24	
air	32,695	5400	1 3 5	19 73 102	0.24 0.28 0.28	
high vacuum	32,704	32000	1 3 5	500 693 707	1.28 1.85 1.81	1.01 1.12 1.17
high vacuum (added mass n°1)	32,388	4000	1 3 5	17 48 72	0.19 0.19 0.31	
high vacuum (added mass n°2)	32,280	9000	1 3 5	61 151 181	0.44 0.46 0.46	0.35 0.37 0.34
air (added mass n°2)	32,260	2900	1 3 5	7 17 052	0.14 0.18 0.21	
high vacuum (added mass n°3)	32,269	7400	1 3 5	38 120 148	0.31 0.44 0.40	0.27 0.34 0.30

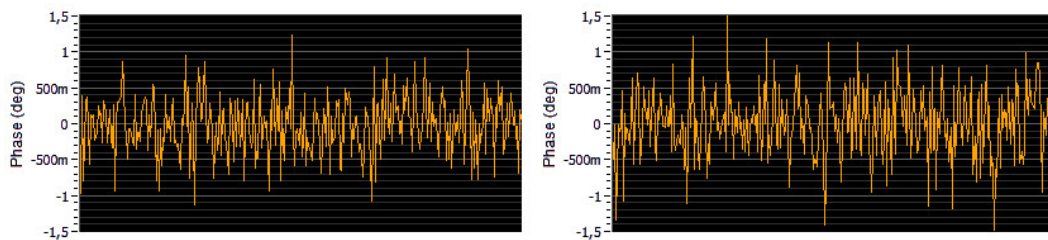

Figure 4.5 - *Phase signal noise in air (left; Q = 5.8k) and vacuum (right; Q=28k), at a given excitation amplitude. This signal which is the basis of frequency shift control is here in both cases identical.*

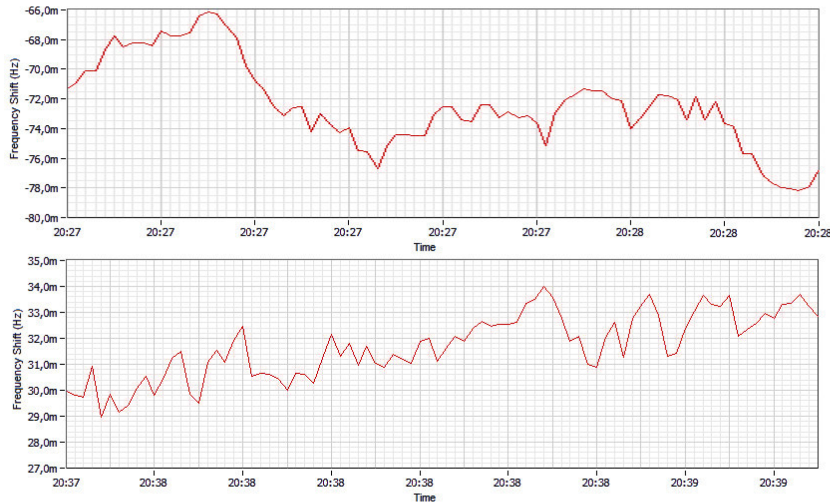

Figure 4.6 - *Corresponding phase-locked frequency shift signal noise in air (top) and vacuum (bottom) at a given excitation amplitude. Over this period of 90 seconds both signals are subjected to drift, but the signal in a vacuum is more stable.*

approach-retract phase or frequency shift curves, or globally in topographic AFM scanning data. In the current setup, SEM vision was used to bring the tip close to the sample, within 40 µm from the surface, before using finer manual or automated Z position control.

This was first done with a tip oriented in the transverse mode (see chapter 2, Fig. 2.7). Approach results were not repeatable enough to lend themselves to a systematic study of the influence of a balanced or unbalanced quality factor in tip-sample approach data. While attractive mode interaction was sometimes observed, a comparison was made impossible due to inconsistent values, or the impossibility of meaningfully distinguishing between attractive and repulsive forces in the negative frequency shift domain (Fig. 4.7). A more commonly consistent approach result with no apparent sensitivity to attractive forces and an increasingly positive frequency shift signal as the tip moves down on the sample is displayed in Fig. 4.8. As Q does not affect the amplitude of the signal generated by the probe, no difference is observed between such approach curves in the air and in a vacuum.

The same approach cycle was then conducted with a tip oriented in the shear mode, which can be used in amplitude or frequency control. After using the preliminary SEM approach procedure, variations in the amplitude signal during the approach were found to be too erratic to allow amplitude-based control (with constant drive and no phase locking). Frequency control (with constant drive and phase locking) did however yield repeatable results, and long range approach curves are displayed in Fig. 4.9. The same results were overall observed between the air and SEM/vacuum environments, albeit with more frequent instability in the latter case. This experiment aside, only transverse-mode quartz probes were used in this work.

The explanation for the inconsistent short-range results obtained even during the course of a same experiment with the same probe can come down to several factors, amongst which are successive changes in the nature or shape of the apex. Van der Waals forces are only sensed at

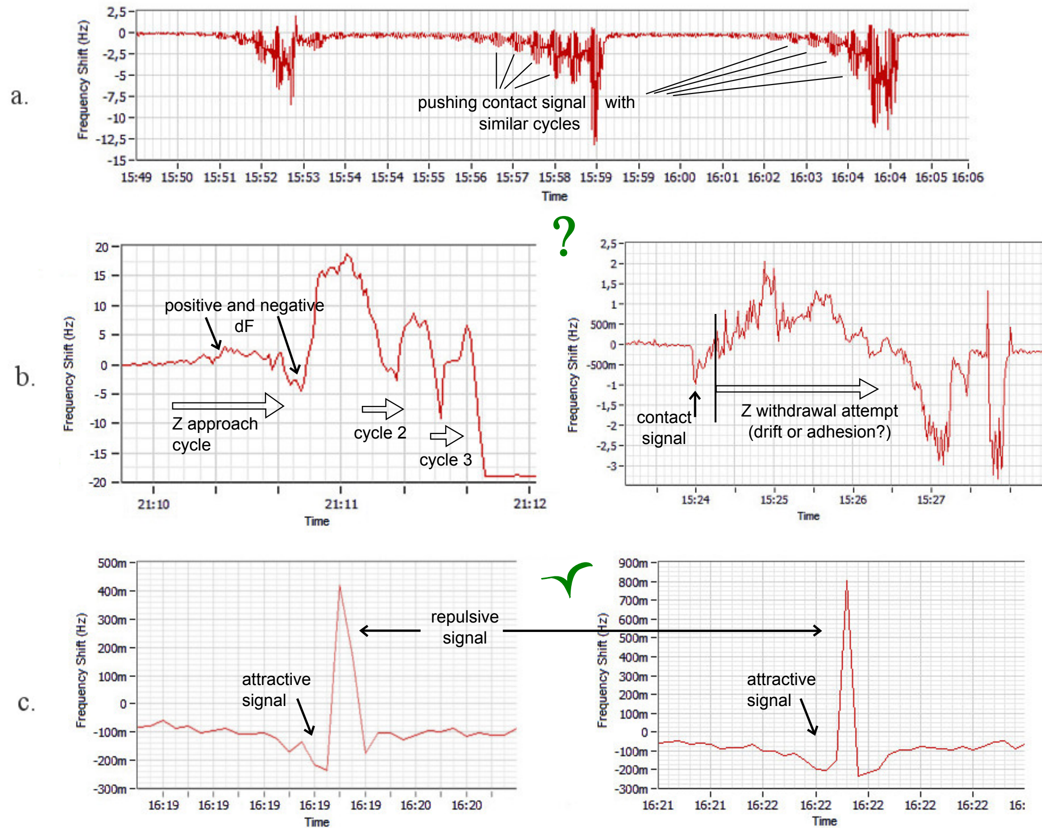

Figure 4.7 - *Transverse oscillation probe: various examples of attractive or repulsive approach curves in the negative frequency shift domain, with tip apices between 50 nm and 1 µm. – a.: slow repulsive approach cycles (at 1 nm/s), with locally repeatable results suggestive of layers; – b.: several successive approach cycles (at 2 nm/s) alternating between negative and positive frequency shift; – c.: approach curves (at 6 nm/s and 2 nm/s) with apparent attractive pull-ins locally repeatable in the 100 mHz range before contact. All results were obtained following tip-sample approach under the SEM beam.*

a very short range, and the electrostatic component of these forces is anisotropic (orientation-dependent), so that a tip with a very small effective apex could on its own yield a variation in the near-contact forces sensed at the end of the approach cycle. The consequences with regard to the size and state of the tip is that while a larger tip should (because of a larger tip-sample interaction surface) yield greater interaction force, it would also average down any such polarisation effect.

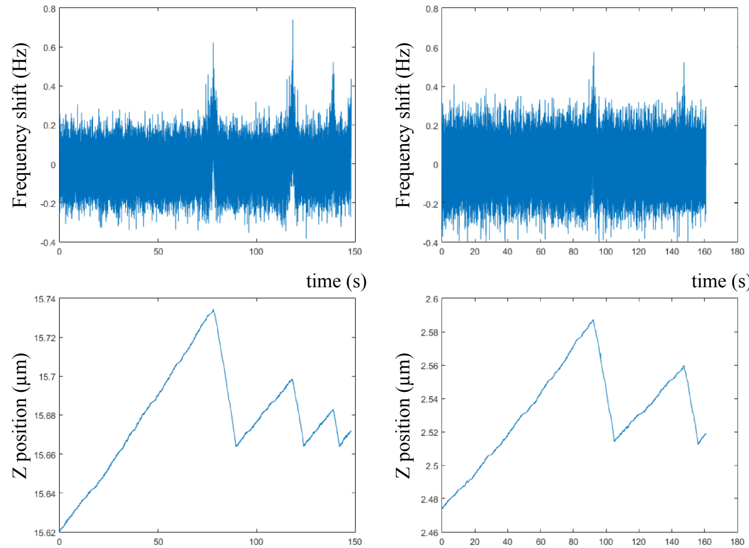

Figure 4.8 - *Transverse oscillation probe: approach and retract curves for repulsive frequency shift in the air (left, Q=5k) and in a vacuum (right, Q=16k) at the nanometre scale. Z position drift is incidentally observed, but these results otherwise display no significant differences due to the environment in the repulsive mode.*

If the higher quality factor obtained in a vacuum does not in this setup lead to increased signal-to-noise, the fact that seemingly attractive forces were still sometimes sensed in a vacuum that were not apparent in the ambient environment could be the result: of an intermediary effect of air molecules (compensating the attractive force at the small range where it can be sensed); of the greater stability in the vacuum frequency shift signal; with larger tips, of the Casimir effect of quantum field theory which is observed in a vacuum (sometimes described as a "relativistic" Van der Waals force [Jaffe 05]); or especially of surface charging under the SEM electron beam, which we will now address.

1.6 Influence of the electron beam in a Scanning Electron Microscope

The technical constraints of embedding an experimental system in a SEM are fundamentally the same as those associated with any vacuum chamber – although the vacuum chambers in AFM experiments can be chosen and built around the system, whereas the sample chamber of a SEM is not expressly designed for AFM-type platforms. Limited space is available and low-outgassing vacuum-compatible materials must be used; as for the quartz probe and its control electronics, electromagnetic shielding and ground circuit architecture are dictated by the SEM

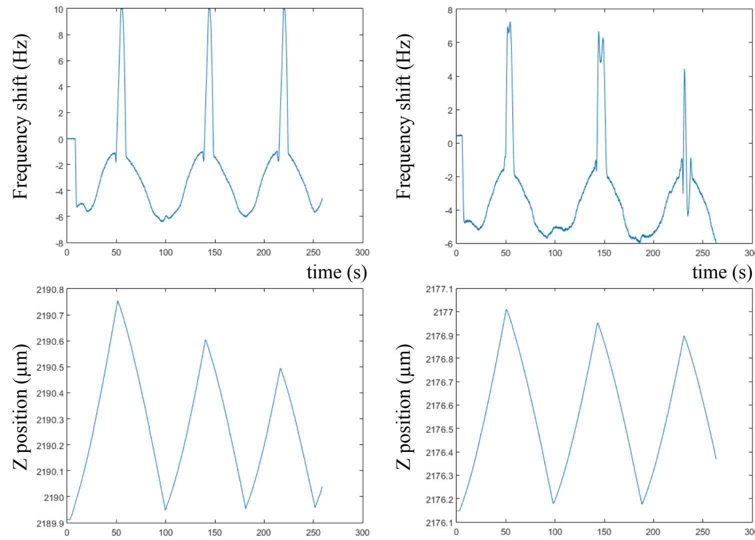

Figure 4.9 - *Shear/lateral oscillation probe: approach and retract curves for repulsive frequency shift in the air (left, Q=1.4k) and in a vacuum (right, Q=6.7k) at a micrometre scale. Equivalent and overall repeatable results are obtained, though with more frequent occurrences of instability in the vacuum.*

model, as are the length and position of cables going towards the outside of the SEM chamber, which affects electronic noise. Aside from these aspects, the greatest impact of a SEM on quartz probe sensing comes from the electron gun either on the tip and probe itself, or on the samples.

The operating principle of a SEM consists in projecting an electron beam on the observed surface, and capturing resulting emissions to recontruct an image of the scanned area. If the impacted surface is not sufficiently conductive, electrons accumulate on it and over time the overcharged surface or object can no longer be clearly observed by the SEM, being intead surrounded by noise on the image (displayed as bright white). For the tip of a quartz probe to be observable without triggering these effects, it is desirable to evacuate the electrons by linking it to the ground electrode of the quartz tuning fork – as previously outlined, this is here done by using conductive silver epoxy in the fabrication. The pre-amplifier used in this setup was designed for this use, so that the oscillation signal does not get disturbed by the electrodes being (directly or through the tip) exposed to the electron beam. Although over long durations, and along the course of various experiments, a few unprovoked disturbances in the oscillation control signals have been observed which could be related to the electron beam, no immediate effect was consistently triggered by its activation or deactivation. It may be worth mentioning that energy charging on the quartz resonator has been observed to affect its resonance frequency (although they are to the best of our knowledge unpublished, studies accounting for energy trapping in a quantified manner were in the past conducted on the subject at the CEA/SPEC with Guy Blaise).

As for the micro-scale components that benefit from being characterised by quartz probes

under SEMs, the sample fabrication process may impose a semi- or weakly conductive substrate – this is the case in the following experiments on micro-membranes. While the objects may still be observed under these conditions, electrostatic charging on the surfaces of the samples and substrate will accrue under prolonged exposure to the electron beam (Fig. 4.11). With or without the tip of the quartz probe being itself exposed, consequences of two types were noticed throughout this work:

- At a very close range, the tip was in a few instances briefly brought down – either deflected or attracted aside – onto a neighbouring area of the sample, before being restored to its previous position. At this scale, such phenomena happen at great speeds and only manifest as a blur on image displays at SEM framerates; they were more reliably evidenced by the sudden and localised destruction of a nearby sample.
- Electrostatic forces were sometimes observed at variable ranges and intensities on the probe frequency shift signal (e.g. Fig. 4.10). Needless to say, these forces interfere with any characterisation or topographical experiment and may either corrupt, as background noise, or negate the sought interaction forces. As the electron beam scanning of several areas or magnifications results in varying electrostatic charging profiles (Fig. 4.11), the effect also differs with the zone where the tip is positioned.

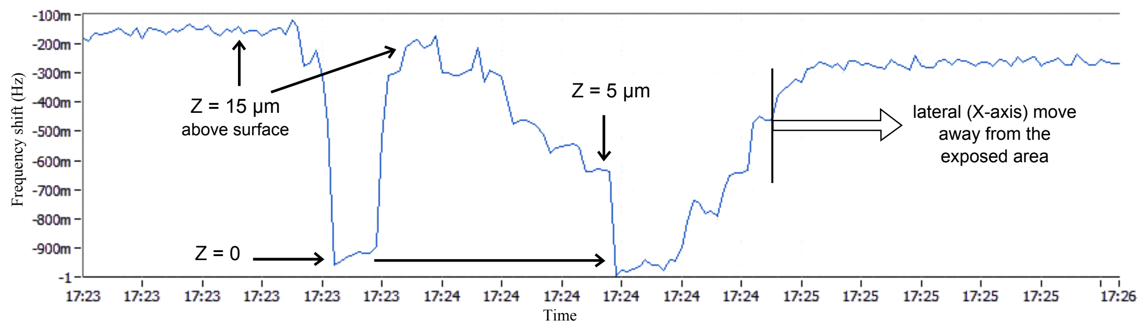

Figure 4.10 - *Example of electrostatic interaction sensed by frequency shift, within a range of 15 µm above the exposed area. Steps closer to the surface yield locally stable values, and the strength of the interaction falls off with distance (half of the 800 mHz shift is observed at a third of the distance). The effect fades entirely when moving away from the electron beam-exposed area and approaching the surface by the same distances.*

The first issue may be attenuated by using stiffer quartz resonators and tips, and electrostatic issues in general by limiting the use of electron beam scanning to short amounts of time. This is made to some extent possible when the purpose of SEM vision is to situate samples rather than monitor all of the experiment: once the position of a known batch of samples is calibrated, the electron beam can be turned off and experiments conducted "blindly" through automation. Long preliminary exposure on poorly conductive samples however leads to changes that remain even without the electron beam being on (Fig. 4.11), either by permanently altering the surface or applying lasting electron charging over the scanned zones.

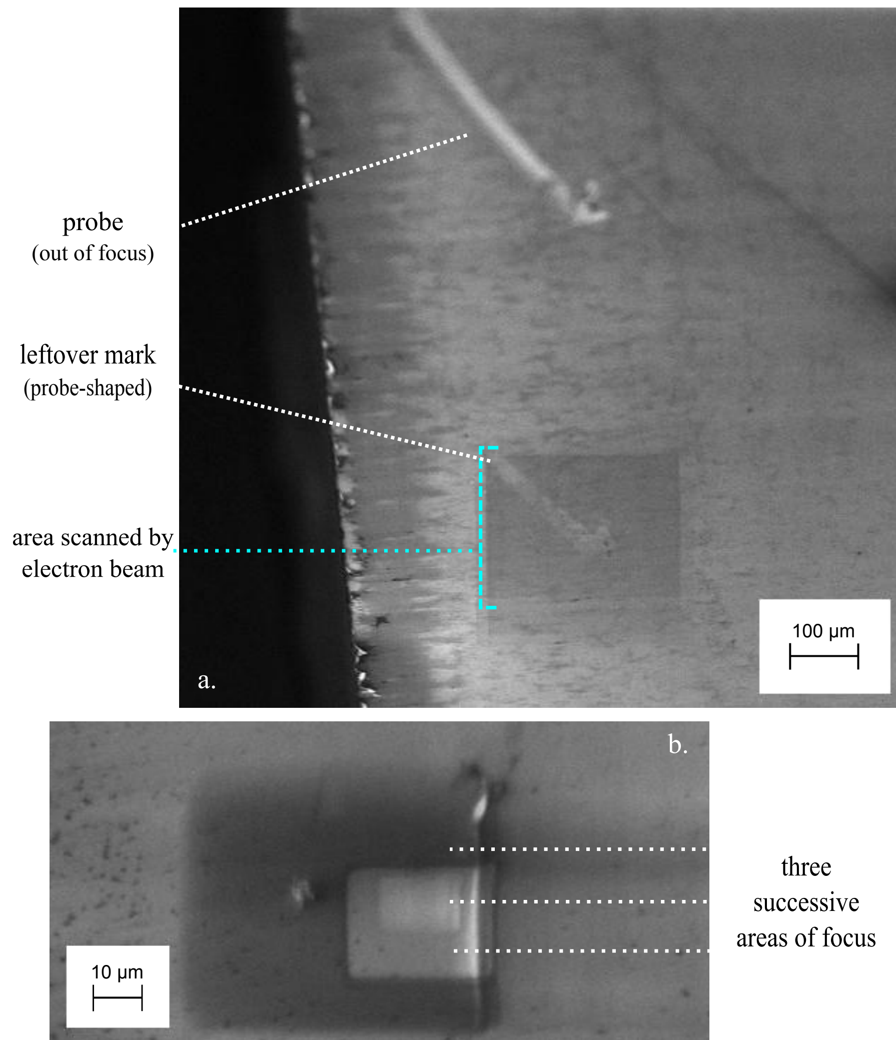

Figure 4.11 - *a.: Effect of several combined hours of SEM exposure on a silicon wafer substrate, still observed days later. (The mark left by the here deformed probe is not due to contact, but to it being interposed between the electron gun and sample, with the SEM sample stage being tilted) – b.: Varying levels of surface electron charge due to successive exposure on increasingly focused areas.*

1.7 Conclusion and perspectives

The impact of the environment – first low pressure, then more particularly a SEM environment – on quartz probe micro-robotic sensing systems has been examined. The high vacuum of a SEM chamber entails an increase in the Q factor of tuning fork probes by a factor of 5. This lower dissipation increases the settling time of the probe in amplitude-based modes, and it is to be noted that while probes with a Q factor lessened by unbalancing reach lesser oscillation amplitudes in a vacuum, this amplitude is still greater than with an equivalent Q in the air, and the driving voltage amplitude still has to be managed accordingly lest longer settling times be incurred. The increase in sensitivity which is also expected from lower dissipation was not clearly observed in the approach experiments conducted in this first section due to various factors, including noise and potential consequences of SEM electron charging. The influence of the electron beam itself is finally hard to predict, and may lead to the presence of spurious forces or other haphazard interaction phenomena: even for materials which are known to be observable by SEM despite imperfect conductivity, there is a greater requirement in local probe experiments for samples and their substrates to be conductive.

2 Membrane stiffness measurement in a SEM

The previous study has covered the issues that must be endured by applications requiring SEM vision, such as the sample characterisation experiment now exposed. The samples in question are micro-scale membranes: micro- and nano-scale mechanical resonators, the behaviour of which is not fully understood due to nonlinearities in their dynamics [Rhoads 10]. In order to characterise the mechanical behaviour of these fragile resonant MEMS/NEMS, non-destructive measurements are required. The mapping of local stiffness variations on a suspended micro-membrane is therefore established here by a quartz tuning fork sensor embedded inside a SEM. Experiments are conducted individually on a batch of InP membranes 200nm thin, using a 9-DoF nano-manipulation system complemented with virtual reality and automation tools. Results provide stiffness values in the range of a few N/m, with variations on single sample depending on the membrane models. The work presented in this section [Abrahamians 14] is supported by the French Agence Nationale de la Recherche, through the NANOROBUST project (contract ANR 2011 NANO 006), and was conducted with Bruno Sauvet. [Sauvet 13]

2.1 Samples and setup

The samples of interest in this work are suspended micro-membranes (Fig. 4.13). Such resonators are critical in the miniaturisation of integrated circuits for resonant sensing and communications. Research on the subject primarily relies on modelling and analysis, hence actual measurements of their mechanical properties are desired in order to better predict and optimise their resonant behaviour. Performing these measurements is not trivial, as typical methods either involve indenting samples or applying enough force to deflect MEMS sensors. These inherently destructive methods can make the measurement itself unreliable [Qiao 13]. Furthermore, they do

not truly allow the mapping of several points on a single sample, as the mechanical properties of the sample are potentially modified after each measurement. More delicate force measurements in the pico-Newton range have been achieved, by complementing the tip of classical probes and observing the deflection of carbon nano-tubes, rather than the cantilever, under a SEM (scanning electron microscope) [Arai 03]. Conversely, this work uses a self-sensing quartz probe, resorting to SEM vision rather to identify samples and position the nanorobotic system. The probe being self-sensing readily allows the automation of the whole nanorobotic measurement process. This automation is not only the end goal of the measurement process, but also brings the duration of experiments down to achievable levels for research purposes. Indeed, manipulation has to be conducted by nanometric steps lest the samples be damaged (Fig. 4.14), which is excessively time-consuming if entirely handled by unassisted human operators. Virtual reality is another useful tool that makes planning trajectories and performing safe manipulation easier and faster. Both of these tools here complement the 9-DoF nanorobotic system to demonstrate a proof of concept for local stiffness measurement and mapping on fragile micro-structures.

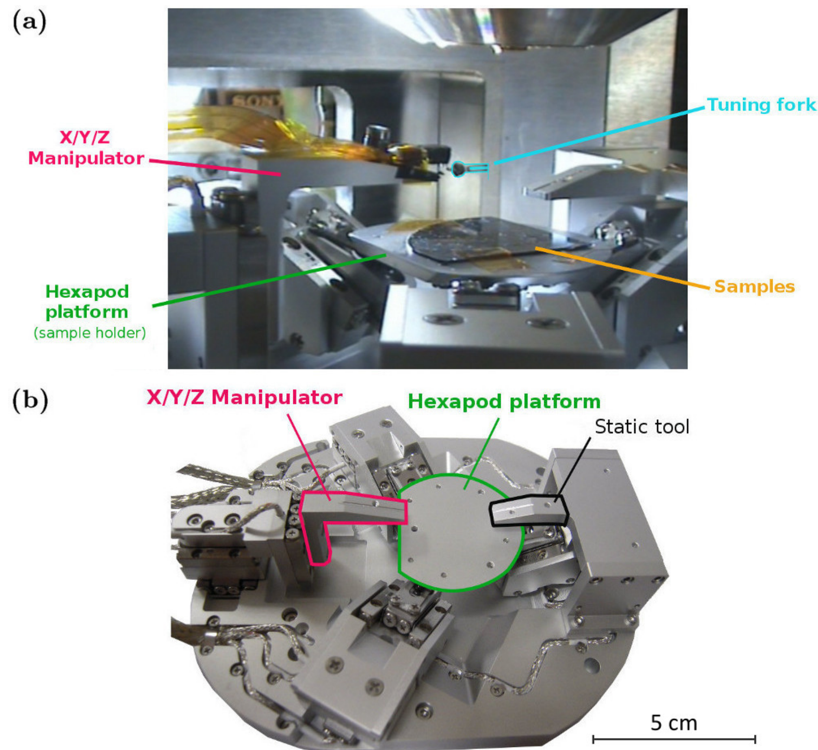

Figure 4.12 - *a) Full manipulation setup inside the SEM vacuum chamber. b) Robotic manipulation platform (SmarAct GmbH); dimensions 11×13×4 cm.*

The nanorobotic manipulation system (Fig. 4.12) is implemented in a Scanning Electron Microscope (Hitachi S-4500). It consists in a 3-DoF Cartesian manipulator and a 6-DoF "hexapod" sample holder platform (SmarAct GmbH, custom-built). Both are composed of closed-loop axial stick-slip actuators. The hexapod's mobility is used to obtain the desired angle between the tool and the sample through its 3 rotational DoF. The actuators offer an ascertained resolution better than 2 nm over a travel range of 12 mm, and are used both for coarse and fine positioning.

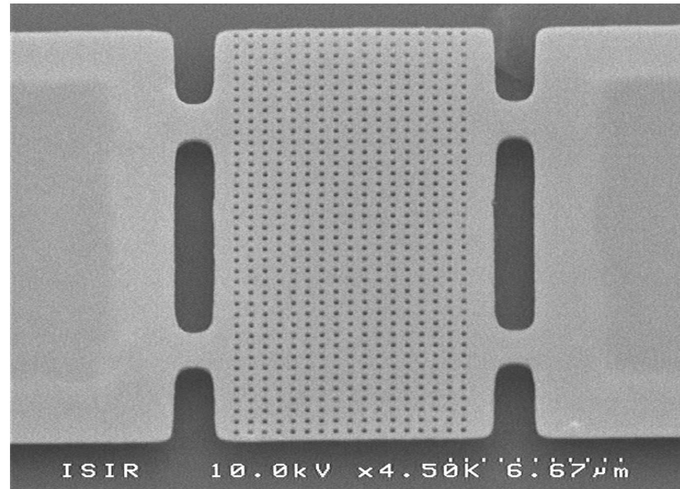

Figure 4.13 - *Suspended membrane. Dimensions 10x20 µm, thickness 200 nm.*

Their closed-loop resolution is determined by the performance of their optical sensors [Zhang 13]. The SEM view and depth of field is used to calibrate the initial positioning of the tool relative to the samples, identify the membrane amongst a batch to operate on *in situ*, and observe its behaviour during experiments. The whole platform can be tilted at an angle up to 45° to discern and accurately control the point where the tip of the probe touches the sample.

The virtual reality interface is a 3D replica of the manipulation unit, rendered in the physics engine of the software Blender. (Fig. 4.15) It relies on data from the actuators' position sensors to calibrate itself and then follows the current state of the system, which can thus be observed even while it is operating inside the vacuum chamber. It was mainly designed as a user-orientated terminal, which allows the planning of position sequences by pre-visualising them on a "ghost" model. It faithfully reproduces the kinematic DoFs of the system and is an interface from which one can directly drive the system, while preventing collisions between elements.

The probes used for this experiment (Fig. 4.16a) are based on 32.768 kHz CF308 quartz tuning forks, fabricated as described in Chapter 2 with a tungsten probe tip, of 1-2 mm length with an apex radius of $<$100 nm (T-4-5 Picoprobe, GGB Industries), manually glued on the side of one prong using conductive silver epoxy (EPO-TEK H21D, Epoxy Technology). The tip is connected to ground through the electrode of the prong it is attached to in order, as mentioned in the previous section, to prevent its electrostatic charging under the electron beam. The tuning fork is then fixed on the manipulator (Fig. 4.16c). The probe is connected to a custom electronic preamplifier adapted for use under the electron beam of the microscope [Polesel-Maris 11a], and the previously described oscillation control system (Nanonis OC4-Station, SPECS GmbH). Data from the controller is then used by a computer for automation.

These measurements use the theoretical model detailed in Sect. 2.2.4. The k_{probe} value used here is 10.7×10^3 N/m [Sauvet 13]. It relies on the geometrical method, which sums up the stiffness of both prongs based on their dimensions and materials, and evaluates a coupling elastic

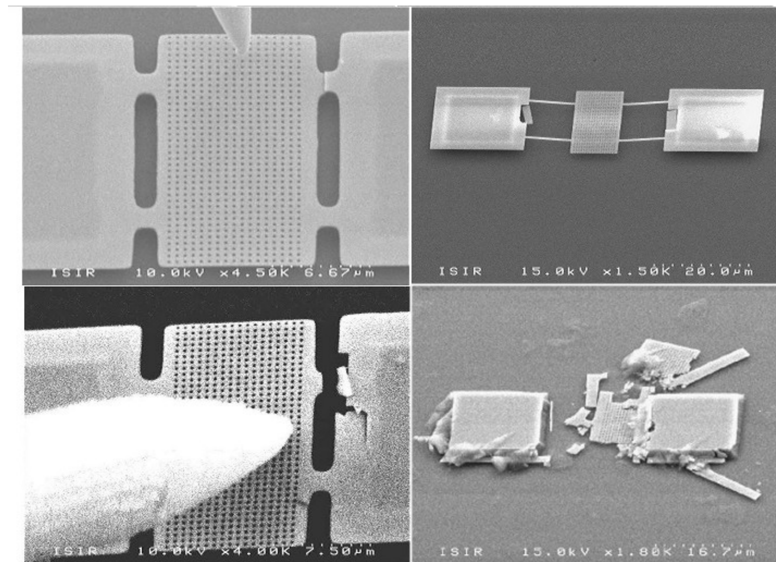

Figure 4.14 - *Above: destroyed hinge (left) or destroyed suspension pads (right) due to electrostatically-induced collisions between the tip of the probe and a sample. Below: consequences of careless manipulation.*

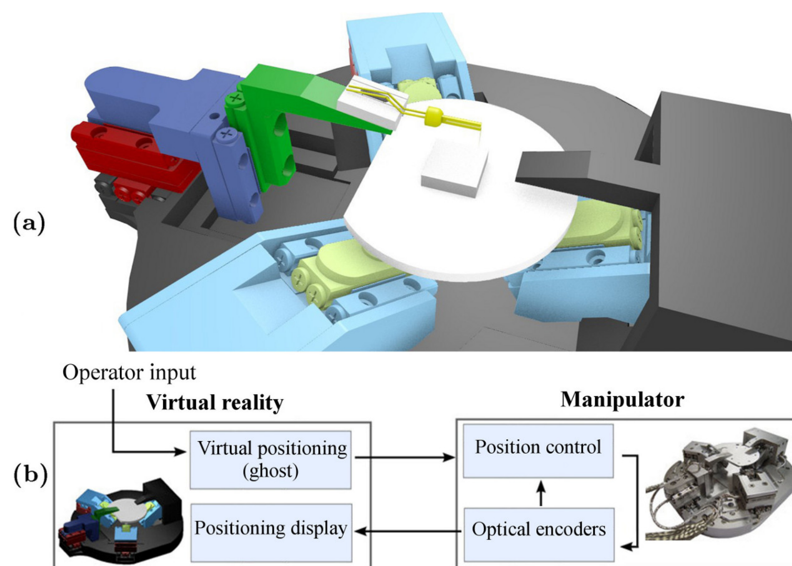

Figure 4.15 - *a) Blender virtual reality system interface. b) Virtual reality control scheme. Trajectory planning uses a "ghost" of the model, whereas the actual position output from the manipulator system sensors is always displayed by the model itself. Travel speed is modulated by discrete position control.*

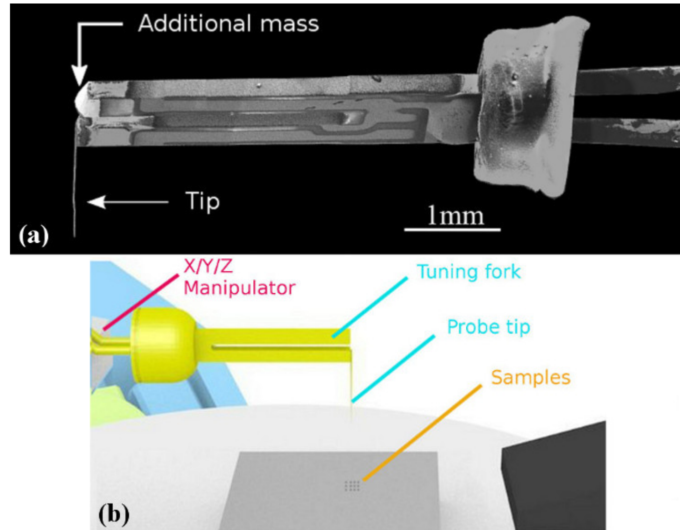

Figure 4.16 - *a) 35° tilted top view of the tuning fork probe by SEM. During a measurement, the apex of the tip is brought into contact with the samples. b) Illustration of the anti-phase coupled oscillation of a tuning fork. c) Illustration of the probe positioned above samples.*

constant as 20-35% of the total [Castellanos-Gomez 10].

2.2 Membrane stiffness measurements

The experiments aim to successively measure the stiffness on several points along the surface of a suspended micro-membrane. They are carried out through the following steps: a model of the samples on the virtual reality system has its position calibrated by bringing the apex of the tip within sensing distance of a sample. After it is calibrated once, the coarse approach is instant thanks to the virtual reality interface, as the probe can be instantly brought down within a safe distance of that sample. The fine approach and measurement itself are then handled by nanometric steps, by a computer using the frequency shift and vibration amplitude data from the controller. Because of the pull-in interaction forces between the probe tip and the substrate (Fig. 4.17), the detection is triggered above the sample without any damaging contact. The angle of incidence of the tip can be adjusted by probing the depth coordinates of three points around the area of interest on the membrane, determining the inclination of the associated plane in the probe's frame of reference, then compensating it with the hexapod. The verticality of the tip relative to the sample is thus ensured, which enables the use of the simplified theoretical model (Fig. 1.15). This is especially useful as compressed InP membranes can take various topographical shapes, bending either inwards or outwards (Fig. 4.18).

The contact between the apex of the tip and the sample results in an increasing frequency shift, and a second order oscillating response of the amplitude which can be observed when the controller starts compensating for the contact with the membrane. A stable frequency shift value is reached after a few seconds. Pushing the probe further down results either in the

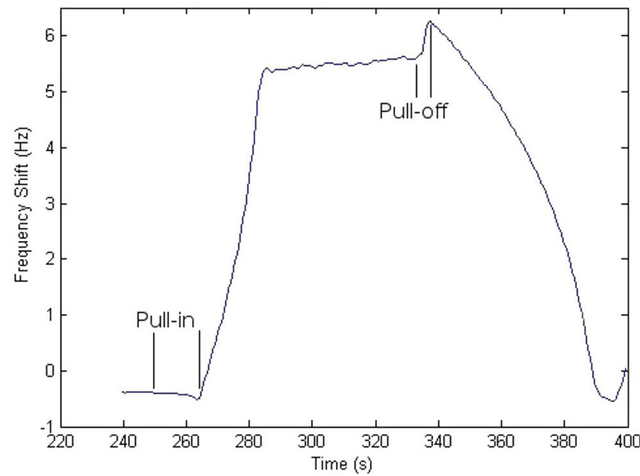

Figure 4.17 - *Frequency shift during a slow measurement operation. The electrostatic and van der Waals interaction forces are observed before reaching the sample: frequency shifts by a few mHz between 150nm and 50nm above the sample (electrostatic pull-in), and by several dozen mHz below 50nm (van der Waals pull-in). After taking a measurement, if the probe is withdrawn slowly, a pull-off resistance resulting from adhesion forces can be observed.*

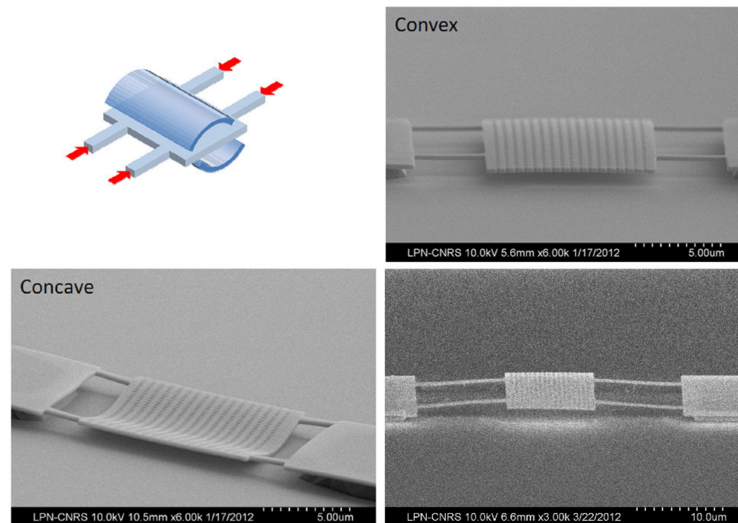

Figure 4.18 - *InP membranes can be stretched or compressed by 20 nm through their fabrication. Compressed membranes can bend in either direction, the exact resulting shape depending on the geometry and position of the hinges.*

membrane hinges visibly breaking, or in unstable values. Measurements can also be unstable in the "non-contact"/"near-contact zone" very close to the sample, but lowering the probe by one nanometre from there on leads to true contact and a stable value. The true measurement point that doesn't affect the sample is therefore the only stable value which can be obtained. These two parts of the measurement process are thus automated through controller data: getting the probe tip in contact with the chosen sample, and recording a stable measurement value (Fig. 4.19), after which the probe withdraws automatically. The choice of sample is done using SEM vision, and the majority of the distance that separates the tip from the sample is first cleared instantly thanks to the reference provided by the virtual reality system. The rest of the procedure is automated. A manual measurement which could take us up to two hours can therefore be conducted automatically within a few minutes.

Stiffness mapping experiments were conducted on dozens of suspended InP membranes 200 nm thin. (Fig. 4.13) The fabrication of these samples was first described in [Strassner 04]: the InP membranes are grown by epitaxy and structured by wet etching. Their shape is rectangular with dimensions 10x20 μm, and they are patterned with air-holes of diameter less than 200 nm. Each membrane is suspended between two supporting pads and held by four hinges. These hinges are the most fragile components of the structure, and the most likely to sever if excessive strain is applied anywhere on the membrane. The samples typically cannot handle being deflected by more than a few nanometres. In comparison, the oscillation amplitude of the tuning fork is non-destructive, as it is estimated under 700 pm using the amplitude calibration procedure described in [Makky 12].

While the InP membranes are themselves semi-conductive, the samples were fabricated on a non-conductive SiO_2 substrate. These *in situ* conditions account for the strong electrostatic charging effects encountered during lengthy experiments, which sometimes resulted either in the disruption of the frequency shift measurement when the probe touches a charged sample, or in destructive electrostatic clamping. The depth performances of electronic microscopy were invaluable in setting up and observing the probe and membranes despite these issues, which were mitigated by shortening the duration of experiments to obtain more measurement points. Faster characterisation procedures hence motivated the development of automated control tools.

2.3 Results

The stiffness values obtained by the local measurements are in the range of a few N/m. Repeated measurements on the same point are found to fall within 5% standard deviation of the hit value, on a sample size of a dozen. This repeatability demonstrates that the measurement method itself is non-destructive. Results vary according to the membrane models, and whether they are compressed or stretched through their fabrication. Hence, we discriminated three membrane types depending on their curvature:

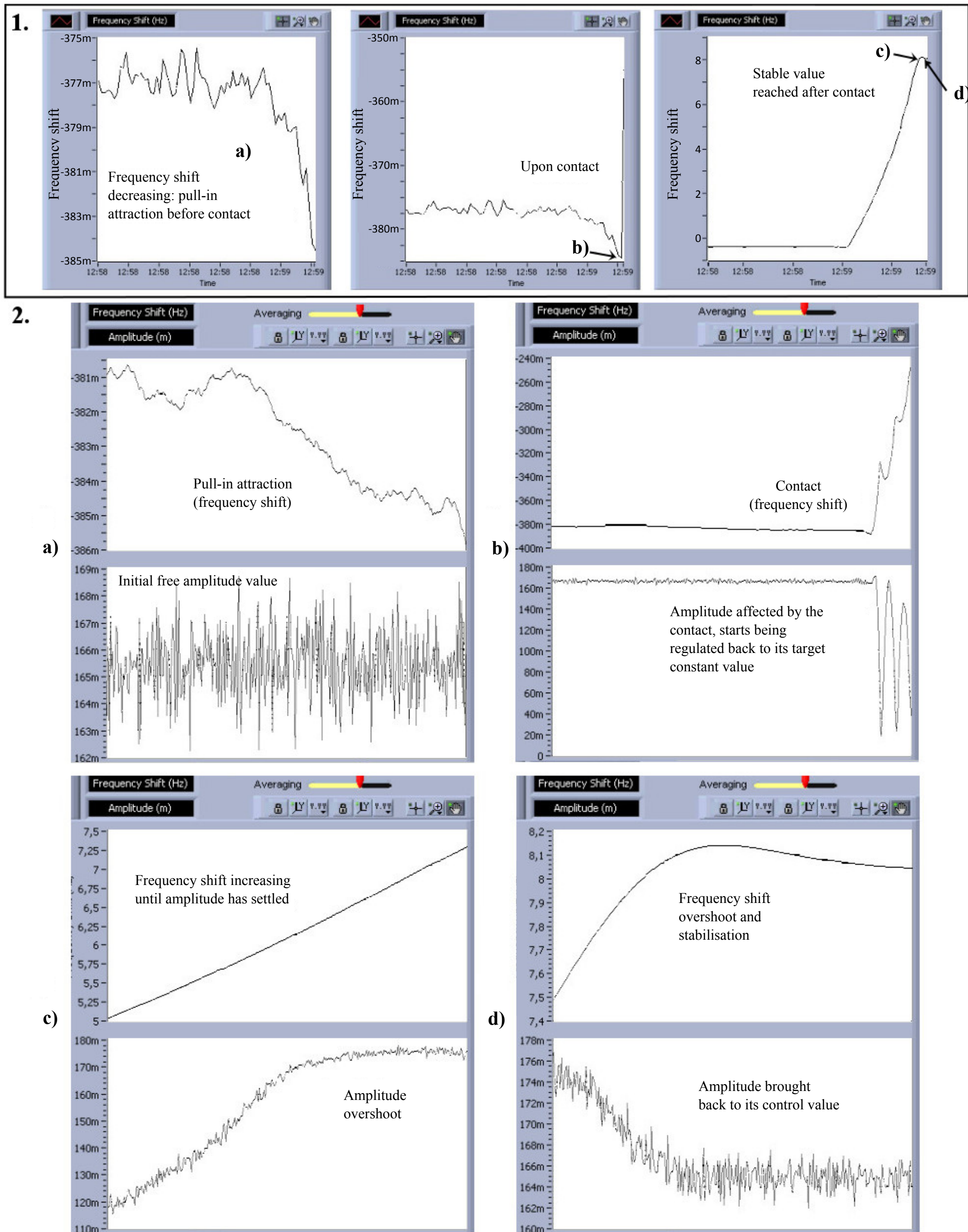

Figure 4.19 - *Automated measurement: data as seen on the Nanonis software. 1: dynamic long-term frequency shift data; 2: frequency shift and amplitude short-term data, each graph spanning 3 seconds. a) Pull-in zone; since the attraction is weak, the amplitude is maintained without any visible variations. b) Frequency shift starts increasing, and the amplitude oscillates from a second order response as it is being regulated by the PLL and AGC, c) d) Amplitude settles back to its initial value, frequency shift stabilises and the measurement is obtained.*

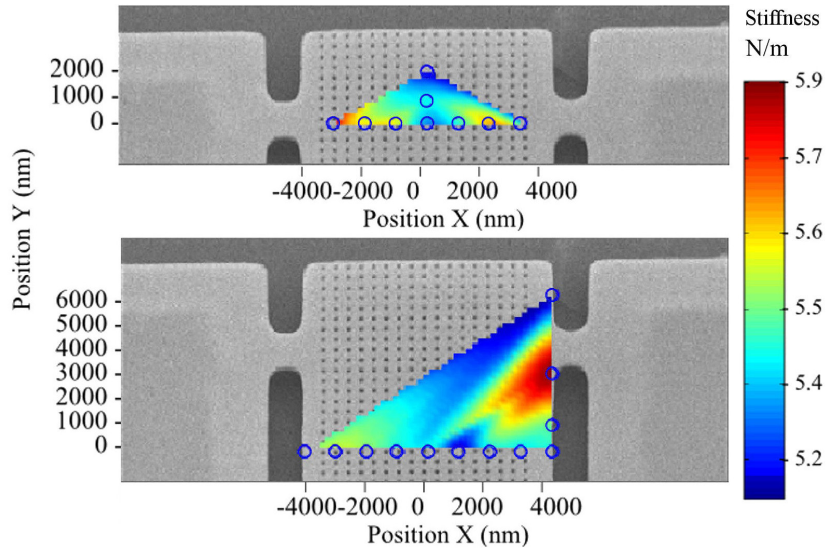

Figure 4.20 - *Local stiffness variations on two stretched flat membranes of the same type. Blue circles mark the points where measurements were taken. The spread colouration is a linear extrapolation for display purposes only.*

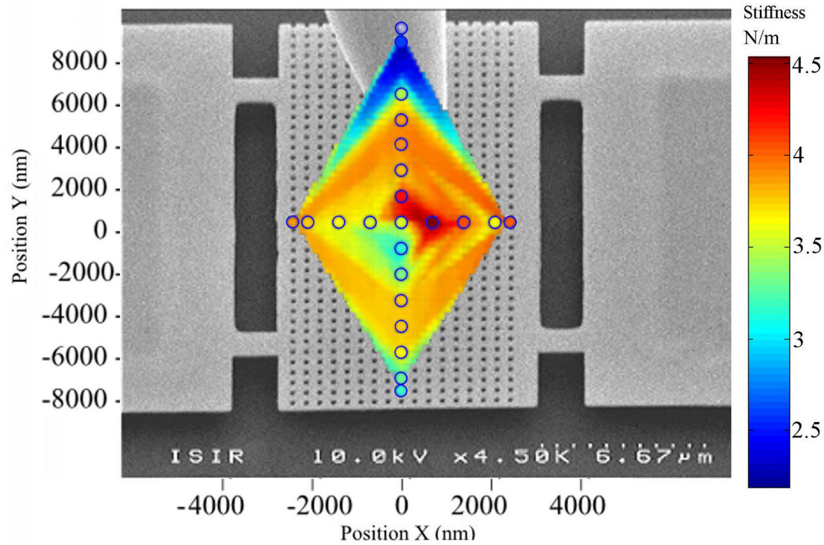

Figure 4.21 - *Local stiffness variations on a convex membrane. Display conventions are similar to Fig. 4.20.*

- Flat membranes
  Experiments conducted on membranes stretched by 20 nm provide values with a variation ranging between 5 and 6 N/m across the samples. Fig. 4.20 lays out the distribution of measurements taken on two similar stretched membrane models. The highest values are obtained near the hinges, which is in agreement with the assumption that the hinges and anchored regions of the sample must be stiffer than the body of the membrane itself. Stiffness gradually decreases when approaching the center or edges of the membrane. Measurements taken on more flat membranes confirm this structural tendency.

- Convex membranes
  In this case, measurements on membranes compressed by 20 nm provide a slightly wider range of values, as seen on Fig. 4.21. Unlike the other models, stiffness increases towards the center of the membrane.

- Concave membranes
  Measurements between two hinges show stiffness varying greatly across the surface of the membrane. The highest values are obtained on the hinges, and two- to five times lower values are obtained near the center of the membrane depending on the geometrical models. Fig. 4.22 shows local stiffness measurements between two hinges of a concave membrane ranging from 0.6 to 3 N/m.

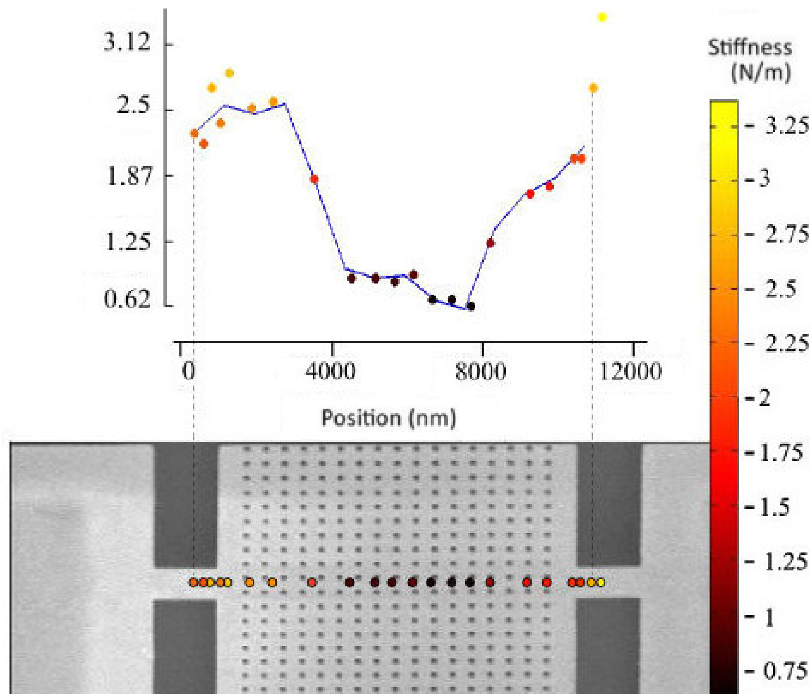

Figure 4.22 - *Stiffness measurements ranging between two suspensions of a concave membrane, taken from left to right. The sample is left undamaged.*

The values obtained for these different models indicate consistent stiffness trends. Stretched membranes are stiffer, as intuitively expected, and exhibit considerably less standard deviation than compressed models. A convex membrane is, interestingly, more stiff at its center - though

overall notably less stiff. Concave membranes have the lowest stiffness values and tend to be less stiff still near their center. All models are stiffer near the hinge nodes as expected.

3 Conclusion

The requirement for SEM vision in flexible micro-scale experimentation contextualises the potential of quartz probes in micro-robotics. A SEM chamber, in which they can be implemented where AFM cantilever detection cannot, imposes the advantages and constraints of a vacuum environment on the micro-robotic system and on the Q factor of the quartz probe. Vacuum environments are not uncommon in AFM, and the specificity of the SEM environment rather lies in the risks of electrostatic charging. The use of the electron beam to get real-time vision feedback on the probe and sample surfaces in practice applies unpredictable effects on tip-sample interaction. Despite the ensuing challenges, a non-destructive local stiffness measurement method has successfully been implemented with quartz tuning fork probes in a SEM. A 9-DoF platform has been used for nano-manipulation, assisted by virtual reality and automation tools for practical purposes. Measurements were taken *in situ* on membranes amidst a manufactured batch, with over twenty measurement points taken on a single membrane without altering it; these measurements will contribute to the design and optimisation of micro-membrane resonators, and to the understanding of their mechanical behaviour. The chosen quartz local-probe approach to measuring the stiffness of MEMS/NEMS mechanical resonator membranes has thus been validated.

Future works may include dynamically monitoring the mechanical behaviour of membranes resonating under external excitation, as well as applying this sensing technique on newer designs of the membranes. These upcoming samples could present more fragile structures, suspended by longer hinges to dramatically elevate their quality factor. Other types of samples with fragile surfaces, such as graphene films, can constitute yet more delicate applications for quartz probes.

Conclusion and Perspectives

Embeddable sensing tools are essential in micro-robotics. Probes must be adapted to the global actuation and control setups required for the scales and performances of a wide range of applications, and although cantilevers have long fulfilled the role of catch-all end tool, we have seen that quartz probes are a definite improvement, fitting the criteria of reliability and flexibility on which scientific development jointly hinges in this field. Reliability implies the means to obtain repeatable quantitative results after calibration as well as delicate and non-destructive operation, which entails the integration of accordingly delicate tools to the appropriate control systems; whereas the goals of fundamental research may be satisfied by statistically sound successes even in discrete occurrences, micro-robotic systems aim for outcomes dependable enough either to be extended to automated processes, or otherwise to apply even to non-systematic or heavily disturbed experimental conditions. Flexibility here further comes into play through compact laserless setups, in which quartz probes can be reoriented and embedded into scanning electron microscopes (SEM) – for the *in situ* observation of samples in real time with greater resolution and field of view – which enables easier tool-sample approach cycles and local targeting.

This work has studied quartz probes for ambient imaging and SEM-controlled experimentation across the following points:

- The fabrication and improvement of customisable tools has been shown to be possible by using standard off-the-shelf electronic components and adding to them a microtip. Understanding the way quartz probes function and how their mechanical parameters govern their performance makes it possible to design and fabricate faster probes, by selecting appropriate higher-frequency resonators, without going through the design and

optimisation of entirely new electromechanical components and without requiring highly specific micromachining equipment.

- Several options for higher-frequency quartz probes have thus been selected and tested, while keeping in mind the criteria of reliability and versatility. Overtone mode excitation and quartz tuning forks with less standard eigenfrequencies have not been deemed interesting, but contoured thickness shear resonators in the MHz range have been analysed and yielded ambient imaging results up to ten times faster than quartz tuning fork probes on a comparable setup.
- The trade-off between scanning speed and force sensitivity has been emphasised in ambient experiments, and the impact on these properties which must be expected from vacuum environments has been laid out, together with the specificities and challenges inherent to the electrostatically charged environment of a SEM.
- A local stiffness characterisation method has been successfully implemented with quartz tuning fork probes in a SEM, with a 9-DoF nano-actuating platform assisted by virtual reality and automation tools. Non-destructive measurements were taken *in situ* on a batch of micro-membranes and locally on individual samples, showcasing the full potential of quartz probes in the context of microrobotics through SEM embedding and conjoined control.

From there, perspectives are open along several lines. While overtone excitation has been discarded on the basis of its performance with most current commercial components, there may yet be ways of exploiting models for which signal-to-noise ratio is the limiting factor, through work on the electronics or with external excitation instead – this would open up possibilities for multi-modal control and additional surface composition detail in imaging. Yet higher-frequency thickness shear resonators exist which only require the corresponding oscillation control equipment, and it remains to be seen whether much higher frequencies could yield improvements even at low speeds through the averaging of increased amounts of data.

The impact of a vacuum environment on QTF AFM sensitivity could not be fully ascertained with the recent SEM setup used here, and technical improvements on shielding and electronic noise mitigation may present more favourable conditions for the study of how the Q-factor impacts sensed forces – and, through this, of the nature of interaction forces with regard to their fall-off with distance. The development of automated control strategies to keep to minimal uses of the electron beam will help palliate the issues encountered in a SEM when it is structurally impossible for samples or their required substrates to be highly conductive. The use of stiffer or higher-frequency probes can also synergise well with efforts for fast and robust operation through unpredictable electrostatic fields or other hazardous conditions.

Lastly, future works will include the characterisation of the SEM-embedded micro-robotic system in variable pressure as regards both the piezo-actuators and the probe, as well as the vision-controlled automation of the membrane stiffness measurement process demonstrated in this work. While sample stages can offer tilting capabilities, they may be limited to small angles and in any case cannot be automatically tracked by SEM vision: the non-laser reliant feedback of quartz probes can onwards be exploited to an even greater extent, by increasing the dexterity and flexibility of probing systems through angular control of the probe end-effector.

Bibliography

[Abrahamians 14] **J.-O. Abrahamians**, **B. Sauvet**, **J. Polesel-Maris**, **R. Braive et S. Regnier**. *A Nanorobotic System for In Situ Stiffness Measurements on Membranes.* IEEE Transactions on Robotics, vol. 30, n° 1, pages 119–124, février 2014.

[Acosta 11] **Juan Camilo Acosta**, **Gilgueng Hwang**, **Jérôme Polesel-Maris et Stéphane Regnier**. *A tuning fork based wide range mechanical characterization tool with nanorobotic manipulators inside a scanning electron microscope.* Review of Scientific Instruments, vol. 82, n° 3, pages 035116–035116–8, mars 2011.

[Akiyama 03] **T. Akiyama**, **U. Staufer**, **N. F. de Rooij**, **P. Frederix et A. Engel**. *Symmetrically arranged quartz tuning fork with soft cantilever for intermittent contact mode atomic force microscopy.* Review of Scientific Instruments, vol. 74, n° 1, pages 112–117, janvier 2003.

[Albrecht 91] **T. R. Albrecht**, **P. Grütter**, **D. Horne et D. Rugar**. *Frequency modulation detection using high-Q cantilevers for enhanced force microscope sensitivity.* Journal of Applied Physics, vol. 69, n° 2, pages 668–673, janvier 1991.

[An 08] **Toshu An**, **Takahiro Nishio**, **Toyoaki Eguchi**, **Masanori Ono**, **Atsushi Nomura**, **Kotone Akiyama et Yukio Hasegawa**. *Atomically resolved imaging by low-temperature frequency-modulation atomic force microscopy using a quartz length-extension resonator.* Review of Scientific Instruments, vol. 79, n° 3, page 033703, mars 2008.

[An 13] **Sangmin An**, **Kunyoung Lee**, **Bongsu Kim**, **Jongwoo Kim**, **Soyoung Kwon**, **Qhwan Kim**, **Manhee Lee et Wonho Jhe**. *Compensation of stray capacitance of the quartz tuning fork for a quantitative force spectroscopy.* Current Applied Physics, vol. 13, n° 9, pages 1899–1905, novembre 2013.

[Ando 01] **Toshio Ando**, **Noriyuki Kodera**, **Eisuke Takai**, **Daisuke Maruyama**, **Kiwamu Saito et Akitoshi Toda**. *A high-speed atomic force microscope for studying biological macromolecules.* Proceedings of the National Academy of Sciences of the United States of America, vol. 98, n° 22, pages 12468–12472, octobre 2001.

[Ando 08] **Toshio Ando**, **Takayuki Uchihashi et Takeshi Fukuma**. *High-speed atomic force microscopy for nano-visualization of dynamic biomolecular processes.* Progress in Surface Science, vol. 83, n° 7–9, pages 337–437, novembre 2008.

[Ando 12] **Toshio Ando**. *High-speed atomic force microscopy coming of age.* Nanotechnology, vol. 23, n° 6, page 062001, février 2012.

[Ando 13] **Toshio Ando**. *Molecular machines directly observed by high-speed atomic force microscopy.* FEBS Letters, vol. 587, n° 8, pages 997–1007, avril 2013.

[Antognozzi 03] **M. Antognozzi**, **M. D. Szczelkun**, **A. D. L. Humphris et M. J. Miles**. *Increasing shear force microscopy scanning rate using active quality-factor control.* Applied Physics Letters, vol. 82, n° 17, pages 2761–2763, avril 2003.

[Arai 03] **F. Arai**, **M. Nakajima**, **Lixin Dong et T. Fukuda**. *Pico-Newton order force measurement using a calibrated carbon nanotube probe by electromechanical resonance.* In IEEE International Conference on Robotics and Automation, 2003. Proceedings. ICRA '03, volume 1, pages 300–305 vol.1, 2003.

[Babic 15] **Bakir Babic**, **Magnus T. L. Hsu**, **Malcolm B. Gray**, **Mingzhen Lu et Jan Herrmann**. *Mechanical and electrical characterization of quartz tuning fork force sensors.* Sensors and Actuators A: Physical, vol. 223, pages 167–173, mars 2015.

[Bak 15] **Wan Bak**, **Baekman Sung**, **Jongwoo Kim**, **Soyoung Kwon**, **Bongsu Kim et Wonho Jhe**. *Time-resolved observation of thermally activated rupture of a capillary-condensed water nanobridge.* Applied Physics Letters, vol. 106, n° 1, page 013102, janvier 2015.

[Barbic 07] **Mladen Barbic**, **Lowell Eliason et James Ranshaw**. *Femto-Newton force sensitivity quartz tuning fork sensor.* Sensors and Actuators A: Physical, vol. 136, n° 2, pages 564–566, mai 2007.

[Baselt 93] **David R. Baselt**. *The tip-sample interaction in atomic force microscopy and its implications for biological applications.* phd, California Institute of Technology, 1993.

[Binnig 82] **G. Binnig**, **H. Rohrer**, **Ch. Gerber et E. Weibel**. *Surface Studies by Scanning Tunneling Microscopy.* Physical Review Letters, vol. 49, n° 1, pages 57–61, juillet 1982.

[Binnig 86] **Binnig**, **Quate et Gerber**. *Atomic force microscope.* Phys. Rev. Lett., vol. 56, n° 9, pages 930–933, mars 1986.

[Boles 12] **Steven T. Boles**, **Andreas Sedlmayr**, **Oliver Kraft et Reiner Mönig**. *In situ cycling and mechanical testing of silicon nanowire anodes for lithium-ion battery applications.* Applied Physics Letters, vol. 100, n° 24, pages 243901–243901–4, juin 2012.

[Braunsmann 10] **Christoph Braunsmann et Tilman E. Schäffer**. *High-speed atomic force microscopy for large scan sizes using small cantilevers.* Nanotechnology, vol. 21, n° 22, page 225705, juin 2010.

[Breguet 98] **Jean-Marc Breguet et Reymond Clavel**. *Actionneurs "stick and slip" pour micro-manipulateurs.* Thèse de doctorat, Ecole polytechnique fédérale de Lausanne EPFL, 1998.

[Brown 13] **Benjamin P. Brown**, **Loren Picco**, **Mervyn J. Miles et Charl F. J. Faul**. *Opportunities in High-Speed Atomic Force Microscopy.* Small, vol. 9, n° 19, pages 3201–3211, 2013.

[Buchaillot 14] **L. Buchaillot**, **E. Mairiaux**, **B. Walter**, **Zhuang Xiong**, **M. Faucher**, **B. Legrand**, **D. Theron et E. Algre**. *Near-field microscopy: Is there an alternative to micro and nano resonating cantilevers?* In Frequency Control Symposium (FCS), 2014 IEEE International, pages 1–2, mai 2014.

[Butt 91] **Hans-Juurgen Butt**. *Electrostatic interaction in atomic force microscopy.* Biophys J, vol. 60, n° 4, pages 777–785, octobre 1991.

[Castellanos-Gomez 10] **Andres Castellanos-Gomez**, **Nicolas Agrait et Gabino Rubio-Bollinger**. *Dynamics of quartz tuning fork force sensors used in scanning probe microscopy.* Nanotechnol., vol. 20, page 215502, mars 2010.

[Chaillet 10] **Nicolas Chaillet et Stéphane Regnier**. Microrobotics for Micromanipulation. Wiley-ISTE, 2010.

[Dedkov 09] **G. V. Dedkov et A. A. Kyasov**. *Conservative–dissipative forces and heating mediated by fluctuation electromagnetic field: Two plates in relative nonrelativistic motion.* Surface Science, vol. 604, n° 5-6, pages 562–567, 2009.

[Dohn 05] **Søren Dohn**, **Rasmus Kousholt Sandberg**, **Winnie Edith Svendsen et Anja Boisen**. *Enhanced functionality of cantilever based mass sensors using higher modes.* Applied Physics Letters, vol. 86, n° 23, page 233501, 2005.

[Dürig 86] **U. Dürig**, **J.K. Gimzewski**, **D.W. Pohl et R. Schlittler**. *Force Sensing in Scanning Tunneling Microscopy.* Rapport technique RZ1513, IBM Research Report, 1986.

[Edwards 97] **Hal Edwards**, **Larry Taylor**, **Walter Duncan et Allan J. Melmed**. *Fast, high-resolution atomic force microscopy using a quartz tuning fork as actuator and sensor.* Journal of Applied Physics, vol. 82, n° 3, pages 980–984, août 1997.

[Eichhorn 12] **V. Eichhorn**, **M. Bartenwerfer et S. Fatikow**. *Nanorobotic Assembly and Focused Ion Beam Processing of Nanotube-Enhanced AFM Probes.* IEEE Transactions on Automation Science and Engineering, vol. 9, n° 4, pages 679 –686, octobre 2012.

[Elawayeb 12] **Mohamed Elawayeb**, **Yong Peng**, **Kevin J. Briston et Beverley J. Inkson**. *Electrical properties of individual NiFe/Pt multilayer nanowires measured in situ in a scanning electron microscope.* Journal of Applied Physics, vol. 111, n° 3, pages 034306–034306–4, février 2012.

[Frisbie 94] **C. D. Frisbie et L. F. Rozsnyai**. *Functional group imaging by chemical force microscopy.* Science, vol. 265, n° 5181, pages 2071–4, 1994.

[Froning 15] **Jens P. Froning**, **Dan Xia**, **Shuai Zhang**, **Erik Lægsgaard**, **Flemming Besenbacher et Mingdong Dong**. *Piezoelectric oscillation sensor based non-contact atomic force microscope for imaging in both ambient and liquid environments.* Journal of Vacuum Science & Technology B, vol. 33, n° 2, page 021801, mars 2015.

[Fukuda 13] **Shingo Fukuda**, **Takayuki Uchihashi**, **Ryota Iino**, **Yasutaka Okazaki**, **Masato Yoshida**, **Kiyohiko Igarashi et Toshio Ando**. *High-speed atomic force microscope combined with single-molecule fluorescence microscope.* Rev Sci Instrum, vol. 84, n° 7, page 073706, juillet 2013.

[Fukuma 06] **Takeshi Fukuma**, **Jason I. Kilpatrick et Suzanne P. Jarvis**. *Phase modulation atomic force microscope with true atomic resolution.* Review of Scientific Instruments, vol. 77, n° 12, page 123703, décembre 2006.

[Giessibl 95] **Franz J. Giessibl**. *Atomic Resolution of the Silicon (111)-(7x7) Surface by Atomic Force Microscopy.* Science, vol. 267, n° 5194, pages 68–71, juin 1995.

[Giessibl 98] **Franz J. Giessibl**. *High-speed force sensor for force microscopy and profilometry utilizing a quartz tuning fork.* Applied Physics Letters, vol. 73, n° 26, pages 3956–3958, décembre 1998.

[Giessibl 00] **Franz J. Giessibl**. *Atomic resolution on Si(111)-(7×7) by noncontact atomic force microscopy with a force sensor based on a quartz tuning fork.* Applied Physics Letters, vol. 76, n° 11, pages 1470–1472, mars 2000.

[Giessibl 05] **Franz J. Giessibl**. *AFM's path to atomic resolution.* Materials Today, vol. 8, n° 5, pages 32–41, mai 2005.

[Giessibl 11] **Franz J. Giessibl**, **Florian Pielmeier**, **Toyoaki Eguchi**, **Toshu An et Yukio Hasegawa**. *Comparison of force sensors for atomic force microscopy based on quartz tuning forks and length-extensional resonators.* Phys. Rev. B, vol. 84, n° 12, page 125409, septembre 2011.

[Gil 11] **M. Gil**, **T. Manzaneque**, **J. Hernando-Garcia**, **A. Ababneh**, **H. Seidel et J.L. Sanchez-Rojas**. *Piezoelectric micro-scale tuning fork resonators for sensing applications.* In Solid-State Sensors, Actuators and Microsystems Conference (TRANSDUCERS), 2011 16th International, pages 1496–1499, juin 2011.

[GmbH 05] **Nanonis GmbH**. *Piezoelectric Quartz Tuning Forks for Scanning Probe Microscopy.* Rapport technique, Nanonis GmbH, Switzerland,, 2005.

[Gonzalez 15] **Laura Gonzalez**, **Roger Oria**, **Luis Botaya**, **Manel Puig-Vidal et Jorge Otero**. *Determination of the static spring constant of electrically-driven quartz tuning forks with two freely oscillating prongs.* Nanotechnology, vol. 26, n° 5, page 055501, 2015.

[Higuchi 11] **Seiji Higuchi**, **Hiromi Kuramochi**, **Osamu Kubo**, **Shintaro Masuda**, **Yoshitaka Shingaya**, **Masakazu Aono et Tomonobu Nakayama**. *Angled long tip to tuning fork probes for atomic force microscopy in various environments.* Review of Scientific Instruments, vol. 82, n° 4, pages 043701–043701–6, avril 2011.

[Island 15] **Joshua O. Island**, **Gary A. Steele**, **Herre S. J. can der Zant et Andres Castellanos-Gomez**. *Mechanical manipulation and exfoliation of boron nitride*

flakes by micro-plowing with an AFM tip. arXiv:1501.06437 [cond-mat], janvier 2015. arXiv: 1501.06437.

[Israelachvili 91] **Jacob N. Israelachvili**. Intermolecular and surface forces / Jacob N. Israelachvili. Academic Press, London ; San Diego, 1991.

[Ito 11] **So Ito et Futoshi Iwata**. *Nanometer-Scale Deposition of Metal Plating Using a Nanopipette Probe in Liquid Condition.* Japanese Journal of Applied Physics, vol. 50, n° 8, page 08LB15, août 2011.

[Jaffe 05] **R. L. Jaffe**. *The Casimir Effect and the Quantum Vacuum.* Physical Review D, vol. 72, n° 2, juillet 2005. arXiv: hep-th/0503158.

[Jahng 07] **Junghoon Jahng**, **Manhee Lee**, **Hanheol Noh**, **Yongho Seo et Wonho Jhe**. *Active Q control in tuning-fork-based atomic force microscopy.* Applied Physics Letters, vol. 91, n° 2, page 023103, juillet 2007.

[Jing 07] **Yun Jing**, **Jin Chen**, **Xiao Chen et Xun Gong**. *Frequency Shift of Thickness-Shear Vibrations of AT-Cut Quartz Resonators Due to a Liquid Layer with the Electrode Stiffness Considered.* IEEE Transactions on Ultrasonics, Ferroelectrics and Frequency Control, vol. 54, n° 7, pages 1290–1292, juillet 2007.

[Karrai 95] **Khaled Karrai et Robert D. Grober**. *Piezoelectric tip-sample distance control for near field optical microscopes.* Applied Physics Letters, vol. 66, pages 1842–1844, avril 1995.

[Kawai 09] **Shigeki Kawai**, **Thilo Glatzel**, **Sascha Koch**, **Bartosz Such**, **Alexis Baratoff et Ernst Meyer**. *Systematic Achievement of Improved Atomic-Scale Contrast via Bimodal Dynamic Force Microscopy.* Phys. Rev. Lett., vol. 103, n° 22, page 220801, novembre 2009.

[Kim 14] **Jongwoo Kim**, **Donghyun Won**, **Baekman Sung**, **Sangmin An et Wonho Jhe**. *Effective stiffness of qPlus sensor and quartz tuning fork.* Ultramicroscopy, vol. 141, pages 56–62, juin 2014.

[Kodera 10] **Noriyuki Kodera**, **Daisuke Yamamoto**, **Ryoki Ishikawa et Toshio Ando**. *Video imaging of walking myosin V by high-speed atomic force microscopy.* Nature, vol. 468, n° 7320, pages 72–76, novembre 2010.

[Koopman 03] **M. Koopman**, **B. I. de Bakker**, **M. F. Garcia-Parajo et N. F. van Hulst**. *Shear force imaging of soft samples in liquid using a diving bell concept.* Applied Physics Letters, vol. 83, n° 24, page 5083, 2003.

[LeDue 09] **J M LeDue**, **M Lopez-Ayon**, **S A Burke**, **Y Miyahara et P Grütter**. *High Q optical fiber tips for NC-AFM in liquid.* Nanotechnology, vol. 20, n° 26, page 264018, juillet 2009.

[Lehenkari 00] **P.P Lehenkari**, **G.T Charras**, **A Nykänen et M.A Horton**. *Adapting atomic force microscopy for cell biology.* Ultramicroscopy, vol. 82, n° 1–4, pages 289–295, février 2000.

[Li 92] **Wenjie Li**, **Jorma A. Virtanen et Reginald M. Penner**. *A nanometer-scale galvanic cell.* The Journal of Physical Chemistry, vol. 96, n° 16, pages 6529–6532, août 1992.

[Lu 16] **Tianming Lu**. *Design and Realization of a Desktop Micro-manipulation Cobotic Platform.* PhD Thesis, Université Pierre et Marie Curie, Percipio Robotics, mars 2016.

[Makky 12] **Ali Makky**, **Thomas Berthelot**, **Cécile Feraudet-Tarisse**, **Hervé Volland**, **Pascal Viel et Jérôme Polesel-Maris**. *Substructures high resolution imaging of individual IgG and IgM antibodies with piezoelectric tuning fork atomic force microscopy.* Sensors and Actuators B: Chemical, vol. 162, n° 1, pages 269–277, février 2012.

[Marsden 13] **A. J. Marsden**, **M. Phillips et N. R. Wilson**. *Friction force microscopy: a simple technique for identifying graphene on rough substrates and mapping the orientation of graphene grains on copper.* Nanotechnology, vol. 24, n° 25, page 255704, juin 2013.

[Mate 87] **C. Mathew Mate**, **Gary M. McClelland**, **Ragnar Erlandsson et Shirley Chiang**. *Atomic-scale friction of a tungsten tip on a graphite surface.* Phys. Rev. Lett., vol. 59, n° 17, pages 1942–1945, octobre 1987.

[Melcher 14] **John Melcher**, **Julian Stirling**, **Felipe Guzmán Cervantes**, **Jon R. Pratt et Gordon A. Shaw**. *A self-calibrating optomechanical force sensor with femtonewton resolution.* Applied Physics Letters, vol. 105, n° 23, page 233109, décembre 2014.

[Menciassi 04] **A. Menciassi**, **A. Eisinberg**, **I. Izzo et P. Dario**. *From Macro to Micro Manipulation: Models and Experiments.* IEEE/ASME Transactions on Mechatronics, vol. 9, n° 2, pages 311–320, juin 2004.

[Minne 95] **S. C. Minne**, **S. R. Manalis et C. F. Quate**. *Parallel atomic force microscopy using cantilevers with integrated piezoresistive sensors and integrated piezoelectric actuators.* Applied Physics Letters, vol. 67, n° 26, pages 3918–3920, décembre 1995.

[Minne 98] **S. C. Minne**, **G. Yaralioglu**, **S. R. Manalis**, **J. D. Adams**, **J. Zesch**, **A. Atalar et C. F. Quate**. *Automated parallel high-speed atomic force microscopy.* Applied Physics Letters, vol. 72, n° 18, pages 2340–2342, mai 1998.

[Morán Meza 13] **José Antonio Morán Meza**. *Propriétés structurelles et électroniques du graphène sur SiC(0001) étudiées par microscopie combinée STM/AFM.* Thèse de doctorat, Paris 11, octobre 2013.

[Najar 15] **H. Najar**, **C. Yang**, **A. Heidari**, **L. Lin et D.A. Horsley**. *Quality Factor in Polycrystalline Diamond Micromechanical Flexural Resonators.* Journal of Microelectromechanical Systems, vol. PP, n° 99, pages 1–1, 2015.

[Nečas 11] **David Nečas et Petr Klapetek**. *Gwyddion: an open-source software for SPM data analysis.* centr.eur.j.phys., vol. 10, n° 1, pages 181–188, novembre 2011.

[Nihei 10] **F. Nihei**, **K. Ideura**, **H. Kobayashi**, **J. Taniguchi et M. Suzuki**. *Mechanical Response of 4He Films Adsorbed on Graphite with a Quartz Tuning Fork.* J Low Temp Phys, vol. 162, n° 5-6, pages 559–564, novembre 2010.

[Noi 13] **Kentaro Noi**, **Daisuke Yamamoto**, **Shingo Nishikori**, **Ken-Ichi Arita-Morioka**, **Takayuki Kato**, **Toshio Ando et Teru Ogura**. *High-Speed Atomic Force Microscopic Observation of ATP-Dependent Rotation of the AAA+ Chaperone p97.* Structure, septembre 2013.

[Nonnenmacher 91] **M. Nonnenmacher**, **M. P. O'Boyle et H. K. Wickramasinghe**. *Kelvin probe force microscopy.* Applied Physics Letters, vol. 58, n° 25, pages 2921–2923, juin 1991.

[Oiko 14] **V. T. A. Oiko**, **B. V. C. Martins**, **P. C. Silva**, **V. Rodrigues et D. Ugarte**. *Development of a quartz tuning-fork-based force sensor for measurements in the tens of nanoNewton force range during nanomanipulation experiments.* Review of Scientific Instruments, vol. 85, n° 3, page 035003, mars 2014.

[Otero 12] **Jorge Otero**, **Laura Gonzalez et Manel Puig-Vidal**. *Nanocharacterization of Soft Biological Samples in Shear Mode with Quartz Tuning Fork Probes.* Sensors, vol. 12, n° 4, pages 4803–4819, avril 2012.

[Peng 15] **Ping Peng**, **Lifeng Hao**, **Ning Ding**, **Weicheng Jiao**, **Qi Wang**, **Jian Zhang et Rongguo Wang**. *Note: Wide band amplifier for quartz tuning fork sensors with digitally controlled stray capacitance compensation.* Review of Scientific Instruments, vol. 86, n° 11, page 116105, novembre 2015.

[Pham Van 08] **L. Pham Van**, **V. Kyrylyuk**, **F. Thoyer et J. Cousty**. *A stabler non contact atomic force microscopy imaging using a tuning fork for air and liquid environments: The zero phase mode atomic force microscopy.* Journal of Applied Physics, vol. 104, n° 7, page 074303, octobre 2008.

[Picco 08] **L. M. Picco**, **P. G. Dunton**, **A. Ulcinas**, **D. J. Engledew**, **O. Hoshi**, **T. Ushiki et M. J. Miles**. *High-speed AFM of human chromosomes in liquid.* Nanotechnology, vol. 19, n° 38, page 384018, septembre 2008.

[Polesel-Maris 11a] **Jérôme Polesel-Maris**. *Electronic control and amplification device for a local piezoelectric force measurement probe under a particle beam*, août 2011.

[Polesel-Maris 11b] **Jérôme Polesel-Maris**, **Christophe Lubin**, **François Thoyer et Jacques Cousty**. *Combined dynamic scanning tunneling microscopy and frequency modulation atomic force microscopy investigations on polythiophene chains on graphite with a tuning fork sensor.* Journal of Applied Physics, vol. 109, n° 7, pages 074320–074320–10, avril 2011.

[Polesel-Maris 12] **Jérôme Polesel-Maris**, **Jérémy Legrand**, **Thomas Berthelot**, **Alexandre Garcia**, **Pascal Viel**, **Ali Makky et Serge Palacin**. *Force spectroscopy by dynamic atomic force microscopy on bovine serum albumin proteins changing the tip hydrophobicity, with piezoelectric tuning fork self-sensing scanning probe.* Sensors and Actuators B: Chemical, vol. 161, n° 1, pages 775–783, janvier 2012.

[Qiao 13] **Li Qiao et Xiaojing Zheng**. *Effect of surface stress on the stiffness of micro/nanocantilevers: Nanowire elastic modulus measured by nano-scale tensile and vibrational techniques.* Journal of Applied Physics, vol. 113, n° 1, pages 013508–013508–9, janvier 2013.

[Qin 12] **Shengyong Qin**, **Tae-Hwan Kim**, **Zhouhang Wang et An-Ping Li**. *Nanomanipulation and nanofabrication with multi-probe scanning tunneling microscope: From individual atoms to nanowires.* Review of Scientific Instruments, vol. 83, n° 6, pages 063704–063704–4, juin 2012.

[Rhoads 10] **Jeffrey F. Rhoads**, **Steven W. Shaw et Kimberly L. Turner**. *Nonlinear Dynamics and Its Applications in Micro- and Nanoresonators.* Journal of Dynamic Systems, Measurement, and Control, vol. 132, n° 3, page 034001, 2010.

[Rodriguez 03] **Tomas R. Rodriguez et Ricardo Garcia**. *Theory of Q control in atomic force microscopy.* Applied Physics Letters, vol. 82, n° 26, pages 4821–4823, juin 2003.

[Ru 11] **Changhai Ru**, **Yong Zhang**, **Yu Sun**, **Yu Zhong**, **Xueliang Sun**, **D. Hoyle et I. Cotton**. *Automated Four-Point Probe Measurement of Nanowires Inside a Scanning Electron Microscope.* IEEE Transactions on Nanotechnology, vol. 10, n° 4, pages 674 –681, juillet 2011.

[Ruppert 13] **Michael G. Ruppert et S. O. Reza Moheimani**. *A novel self-sensing technique for tapping-mode atomic force microscopy.* Review of Scientific Instruments, vol. 84, n° 12, page 125006, décembre 2013.

[Sader 05] **John E. Sader**, **Takayuki Uchihashi**, **Michael J. Higgins**, **Alan Farrell**, **Yoshikazu Nakayama et Suzanne P. Jarvis**. *Quantitative force measurements using frequency modulation atomic force microscopy—theoretical foundations.* Nanotechnology, vol. 16, n° 3, page S94, 2005.

[Sauvet 13] **Bruno Sauvet**. *Design of a microrobotic platform for the manipulation and characterization of thin films.* Thèse de doctorat, Université Pierre et Marie Curie, Paris, mars 2013.

[Sell 11] **J. K. Sell**, **A. O. Niedermayer et B. Jakoby**. *Simultaneous measurement of density and viscosity in gases with a quartz tuning fork resonator by tracking of the series resonance frequency.* Procedia Engineering, vol. 25, pages 1297–1300, 2011.

[Seo 05] **Yongho Seo**, **Paul Cadden-Zimansky et Venkat Chandrasekhar**. *Low-temperature high-resolution magnetic force microscopy using a quartz tuning fork.* Applied Physics Letters, vol. 87, n° 10, page 103103, septembre 2005.

[Shaw 14] **Gordon A. Shaw**. *Improvement in Uncertainty of Tuning Fork-Based Force Sensor Stiffness Calibration via the Indentation Method Using Direct Determination of Contact and Machine Compliance.* In **Gordon Shaw III**, **Barton C. Prorok**, **LaVern Starman et Cosme Furlong**, éditeurs, MEMS and Nanotechnology, Volume 5, Conference Proceedings of the Society for Experimental Mechanics Series, pages 125–128. Springer International Publishing, janvier 2014.

[Strassner 04] **M. Strassner**, **J.-L. Leclercq et I. Sagnes**. *Fabrication of ultra-thin InP membranes and their application for high reflective mirrors in tunable vertical-cavity devices.* In 2004 International Conference on Indium Phosphide and Related Materials, 2004. 16th IPRM, pages 221 – 223, juin 2004.

[Su 02] **Xiaodi Su**, **Changchun Dai**, **Jian Zhang et Sean J O'Shea**. *Quartz tuning fork biosensor.* Biosensors and Bioelectronics, vol. 17, n° 1–2, pages 111–117, janvier 2002.

[Takahashi 11] **M. Takahashi**, **H. Ko**, **T. Ushiki et F. Iwata**. *Interactive nano manipulator based on an atomic force microscope for scanning electron microscopy.* In 2011 International Symposium on Micro-NanoMechatronics and Human Science (MHS), pages 495 –500, novembre 2011.

[Terris 89] **B. D. Terris**, **J. E. Stern**, **D. Rugar et H. J. Mamin**. *Contact electrification using force microscopy.* Phys. Rev. Lett., vol. 63, n° 24, pages 2669–2672, décembre 1989.

[Toledo 14] **J. Toledo**, **T. Manzaneque**, **J. Hernando-García**, **J. Vázquez**, **A. Ababneh**, **H. Seidel**, **M. Lapuerta et J. L. Sánchez-Rojas**. *Application of quartz tuning forks and extensional microresonators for viscosity and density measurements in oil/fuel mixtures.* Microsyst Technol, vol. 20, n° 4-5, pages 945–953, février 2014.

[Torbrügge 10] **Stefan Torbrügge**, **Oliver Schaff et Jörg Rychen**. *Application of the KolibriSensor® to combined atomic-resolution scanning tunneling microscopy and noncontact atomic-force microscopy imaging.* Journal of Vacuum Science & Technology B, vol. 28, n° 3, pages C4E12–C4E20, mai 2010.

[Tung 10] **Ryan C. Tung**, **Thorsten Wutscher**, **David Martinez-Martin**, **Ronald G. Reifenberger**, **Franz Giessibl et Arvind Raman**. *Higher-order eigenmodes of qPlus sensors for high resolution dynamic atomic force microscopy.* Journal of Applied Physics, vol. 107, n° 10, page 104508, mai 2010.

[Uchihashi 06] **Takayuki Uchihashi**, **Toshio Ando et Hayato Yamashita**. *Fast phase imaging in liquids using a rapid scan atomic force microscope.* Applied Physics Letters, vol. 89, n° 21, page 213112, novembre 2006.

[van Vörden 12] **Dennis van Vörden**, **Manfred Lange**, **Merlin Schmuck**, **Nico Schmidt et Rolf Möller**. *Spring constant of a tuning-fork sensor for dynamic force microscopy.* Beilstein J. Nanotechnol., vol. 3, pages 809–816, 2012.

[Wang 13] **Wenjun Wang**, **Rongxing Wu**, **Ji Wang**, **Jianke Du et Jiashi Yang**. *Thickness-shear modes of an elliptical, contoured at-cut quartz resonator.* IEEE Transactions on Ultrasonics, Ferroelectrics and Frequency Control, vol. 60, n° 6, pages 1192–1198, juin 2013.

[Wastl 13] **Daniel S. Wastl**, **Alfred J. Weymouth et Franz J. Giessibl**. *Optimizing atomic resolution of force microscopy in ambient conditions.* Phys. Rev. B, vol. 87, n° 24, page 245415, juin 2013.

[Watanabe 13] **Hiroki Watanabe**, **Takayuki Uchihashi**, **Toshihide Kobashi**, **Mikihiro Shibata**, **Jun Nishiyama**, **Ryohei Yasuda et Toshio Ando**. *Wide-area scanner for high-speed atomic force microscopy.* Review of Scientific Instruments, vol. 84, n° 5, page 053702, mai 2013.

[Wei 14] **Hao Ting Wei**, **Chun Yu Hsu et Shu Jung Chen**. *Research on miniature quartz tuning fork with quality factor.* In Microsystems, Packaging, Assembly and Circuits Technology Conference (IMPACT), 2014 9th International, pages 494–497, octobre 2014.

[Weisenhorn 89] **A. L. Weisenhorn**, **P.K. Hansma**, **T.R. Albrecht et C.F. Quate**. *Forces in atomic force microscopy in air and water.* Applied Physics Letters, vol. 54, n° 26, pages 2651–2653, 1989.

[Xie 12a] **Hui Xie**, **Cagdas Onal**, **Stéphane Régnier et Metin Sitti**. Atomic Force Microscopy Based Nanorobotics, volume 71 of *Springer Tracts in Advanced Robotics.* Springer Berlin Heidelberg, Berlin, Heidelberg, 2012.

[Xie 12b] **Hui Xie et S. Régnier**. *High-Efficiency Automated Nanomanipulation With Parallel Imaging/Manipulation Force Microscopy.* IEEE Transactions on Nanotechnology, vol. 11, n° 1, pages 21–33, janvier 2012.

[Yang 12] **Zhan Yang**, **M. Nakajima**, **Yajing Shen et T. Fukuda**. *Assembly and evaluation of MWCNTs probe thermal sensor by nanorobotic manipulation.* In 2012 12th IEEE Conference on Nanotechnology (IEEE-NANO), pages 1 –4, août 2012.

[Yong 12] **Y. K. Yong**, **S. O. R. Moheimani**, **B. J. Kenton et K. K. Leang**. *High-speed flexure-guided nanopositioning: Mechanical design and control issues.* Review of Scientific Instruments, vol. 83, n° 12, page 121101, décembre 2012.

[Zhang 13] **Yan Liang Zhang**, **Yong Zhang**, **Changhai Ru**, **B.K. Chen et Yu Sun**. *A Load-Lock-Compatible Nanomanipulation System for Scanning Electron Microscope.* IEEE/ASME Transactions on Mechatronics, vol. 18, n° 1, pages 230 –237, février 2013.

[Zhong 93] **Q. Zhong**, **D. Inniss**, **K. Kjoller et V. B. Elings**. *Fractured polymer/silica fiber surface studied by tapping mode atomic force microscopy.* Surface Science Letters, vol. 290, n° 1, pages L688–L692, juin 1993.

[Zurich Instruments 12] **Zurich Instruments**. *HF2PLL Phase-locked Loop Technical Note.* Technical Note, février 2012.

List of publications

Published :

1. Abrahamians, J.O. and Sauvet, B. and Polesel-Maris, J. and Braive, R. and Régnier, S.
   Nanorobotic system for in situ stiffness measurements on membranes.
   IEEE Transactions on Robotics (T-RO), Volume 30, Issue 1, pp. 119-124, 2014.
2. Abrahamians, J.O. and Sauvet, B. and Polesel-Maris, J. and Braive, R. and Régnier, S.
   Robotic in Situ Stiffness Cartography of InP Membranes by Dynamic Force Sensing.
   IEEE/RSJ International Conference on Intelligent Robots and Systems (IROS), 2013.

Pending :

3. Abrahamians, J.O. and Pham Van, L. and Régnier, S.
   Quartz Force Sensing Probes for Micro-applications, AIP/Review of Scientific Instruments (RSI).